

Grant agreement no.: FCH-JU-325386



Support to Safety Analysis of Hydrogen and Fuel Cell Technologies

Report on Model Benchmarking Exercise “II”



The SUSANA project is co-funded by the European Commission within the 7th Framework Program

List of Authors
(randomly ordered by list of partner Institutions)

Olaf Jedicke (project coordinator)

Authors

Alexei Kotchourko
Ke Ren
Volodymyr Shentsov
Dmitriy Makarov
James Keenan
Vladimir Molkov
Daniele Baraldi
Daniele Melideo
Stella Giannissi
Ilias Tolias
Alexandros Venetsanos
Simon Coldrick
Franck Verbecke
Audrey Duclos
Shane Slater

Copyright

This Document has been created within the FP7 project SUSANA. The utilization and release of this document is subject to the conditions of the contract within the 7th EU Framework Program. Project reference is Grant agreement no.: FCH-JU-325386

Content

Content.....	3
1. Introduction.....	8
2. Release and Dispersion.....	8
2.1 GARAGE experiment.....	8
2.1.1 Experimental description.....	8
2.1.2 Modeling approach.....	12
2.1.3 Sensitivity studies.....	26
2.1.4 Results and discussion.....	44
2.1.5 Comparison of the results by all partners.....	58
2.1.6 Statistical analysis.....	60
2.1.7 Concluded remarks.....	62
2.1.8 References.....	64
2.2 GAMELAN experiment.....	65
2.2.1 Experimental description.....	65
2.2.2 Modelling approach.....	66
2.2.3 Mesh Generation.....	68
2.2.4 Initial and Boundary condition.....	71
2.2.5 Discretization of the system of equations.....	71
2.2.6 Results.....	72
2.2.7 Conclusions.....	76
2.2.8 References.....	77
3. Deflagration.....	77
3.1 Experiment overview.....	77
3.2 Mathematical methodology.....	77
3.2.1 Governing equations.....	77
3.2.2 Simulation approach.....	79
3.2.3 Numerical details.....	80
3.3 Conclusions.....	82
3.4 References.....	88
4. Deflagration to detonation transition.....	88
4.1 Experiment overview.....	88
4.2 Mathematical Methodology.....	90
4.2.1 Governing equations.....	90
4.2.2 Simulation approach.....	93
4.2.3 Numerical details.....	94
4.3 Results and discussion.....	95
4.4 References.....	99

Table List

Table 2-1. Test parameters.....9
 Table 2-2. Sensors coordinates.10
 Table 2-3. JRC-List of the simulations performed17
 Table 2-4. UU-Parameters of numerical simulations.23
 Table 2-5. EE- List of the simulations performed.25
 Table 2-6. AREVA-The main characteristics of the grids that were tested.....26
 Table 2-7. NCSR- The main characteristics of the grids that were tested.35
 Table 2-8. Model performance measures for the peak concentration.....60
 Table 2-9. Model performance measures for time=7000 s.61
 Table 2-10. Model performance measures for time=20000 s.61
 Table 2-11. Summary of the experimental conditions.....65
 Table 2-12. Meshes used to simulate GAMELAN.....70
 Table 2-13. Model performance measures.....76
 Table 3-1. Constants set for the Standard k-ε method.78
 Table 4-1. Transducers.....89
 Table 4-2. Initial condition90

Figure List

Figure 2-1. Description of GARAGE set-up at CEA Saclay. GARAGE structure showing front and service door (left) and GARAGE structure equipped with Styrodur® sheets (right).....8
 Figure 2-2. Openings (upper vent closed, lower vent open).....10
 Figure 2-3. Sensor location.12
 Figure 2-4. AREVA-Mesh used to simulate the rejection in the garage.15
 Figure 2-5. JRC-Detail of the mesh at symmetry plane for mesh #118
 Figure 2-6. JRC-Detail of the mesh at symmetry plane for mesh #219
 Figure 2-7. JRC-Detail of the mesh at symmetry plane for mesh #2.b19
 Figure 2-8. JRC-Detail of the mesh at symmetry plane for mesh #320
 Figure 2-9. JRC-Detail of the mesh at symmetry plane for mesh #420
 Figure 2-10. JRC-Detail of the mesh at symmetry plane for mesh #521
 Figure 2-11. JRC-Details of the inlet boundary meshes22
 Figure 2-12. EE- Mesh inside garage showing three levels of mesh refinement: Plan view above, side elevation below. Refinement regions outlined in yellow. Mesh outside garage not show.26
 Figure 2-13. AREVA- Numerical results of the third sensor (going from the bottom) of the mast 1 obtained with different meshes.27
 Figure 2-14. JRC-The results from the grid sensitivity study using the SST model. ..28
 Figure 2-15. JRC-The results from the grid sensitivity study using the SST model. ..29
 Figure 2-16. JRC-The results from the grid sensitivity study using the laminar model.30
 Figure 2-17. JRC-The results from the grid sensitivity study using the DES model...31
 Figure 2-18. JRC-The results from the time step sensitivity study.....32
 Figure 2-19. JRC-Domain expansion sensitivity study.33

Figure 2-20. NCSR-D-The results from the domain sensitivity study with k-ε turbulence model.....34

Figure 2-21. NCSR-D-The results without domain expansion with k-ε turbulence model.....35

Figure 2-22. NCSR-D-The results from the grid independency study with k-ε turbulence model.....36

Figure 2-23. NCSR-D-The results from the time step sensitivity study with k-ε turbulence model.....37

Figure 2-24. NCSR-D-The results obtained with different grid sizes and the laminar model.....38

Figure 2-25. NCSR-D-The results obtained with different grid sizes and the RNG-LES model.....39

Figure 2-26. NCSR-D- The results from the time step sensitivity study for the RNG-LES model39

Figure 2-27. UU-Garage centreline cross sections from top to bottom Grid 1 (254,089 CV's), Grid 2 (523,540 CV's), Grid 3 (996,639 CV's): x=0 (left), y=0 (middle), z=0 (right).40

Figure 2-28. UU-Extended domain cross sections from left to right: x=0, y=0, z=0, vent and inlet cross sections.....41

Figure 2-29. UU-The results from the grid independency study.....42

Figure 2-30. UU-The results from the time step sensitivity study.....42

Figure 2-31. EE- Results from the grid sensitivity study using LES turbulence model.43

Figure 2-32. AREVA-The mass balance and the mass error during the low Reynolds k-ω simulation.....45

Figure 2-33. AREVA-Computational results of helium concentration at several sensors.....45

Figure 2-34. AREVA- Comparison of the results using the low Reynolds k-ω turbulence model with the experimental results.46

Figure 2-35. AREVA-Helium concentration contours on y-injection plane with the low Re k-ω model at 3740 s (top), 10000 s (center) and 20000 s (bottom).....47

Figure 2-36. AREVA-Predicted flammable mass inside the GARAGE facility48

Figure 2-37. JRC-The mass balance and the mass error during the SST simulation...48

Figure 2-38. JRC-Comparison of the results using the SST turbulence model and the experimental results.49

Figure 2-39. JRC-Helium concentration contours on y-injection plane with the SST model at 3740 s (left, top), 10000 s (right, top) and 20000 s (bottom).50

Figure 2-40. JRC-Predicted flammable mass inside the GARAGE facility.....50

Figure 2-41. NCSR-D-The mass balance and the mass error during the simulations. .50

Figure 2-42. NCSR-D-Comparison of the results using the laminar model, the k-ε model and the RNG-LES turbulence model with the experiment.51

Figure 2-43. NCSR-D-Helium concentration contours on y-injection plane with the laminar model at 3740 s (left, top), 10000 s (right, top) and 20000 s (bottom).....52

Figure 2-44. NCSR-D-Helium concentration contours on y-injection plane with the k-ε at 3740 s (left, top), 10000 s (right, top) and 20000 s (bottom).....52

Figure 2-45. NCSR-D-Helium concentration contours on y-injection plane with the RNG-LES at 3740 s (left, top), 10000 s (right, top) and 20000 s (bottom).53

Figure 2-46. NCSR-D-Predicted flammable mass inside the GARAGE facility.53

Figure 2-47. UU-The mass balance and the mass error during the simulations.54

Figure 2-48. UU-Comparison of the results using LES Dynamic S-L and RNG-LES turbulence model with the experiment.54

Figure 2-49. UU-Helium concentration contours on y-injection plane with LES Dynamic S-L at 3740 s (top), 10000 s (right, center) and 20000 s (bottom). The hole is on the right side.55

Figure 2-50. UU-Helium concentration contours on y-injection plane with RNG-LES at 3740 s. The hole is on the right side.56

Figure 2-51. UU-Predicted flammable mass inside the GARAGE facility.56

Figure 2-52. EE-Comparison of the results using LES model with the experiment....57

Figure 2-53. EE-Contours of He concentration at 3740 s (top) and 10,000 s (bottom).58

Figure 2-54. EE-Predicted flammable mass inside the GARAGE facility.58

Figure 2-55. Comparison of the results by JRC and NCSR-D partner with the laminar model.59

Figure 2-56. Comparison of the results by NCSR-D and UU partner with the RNG-LES.59

Figure 2-57. Geometric mean bias (MG) versus geometric mean variance (VG) for peak helium concentration.62

Figure 2-58. : Experimental environment of GAMELAN (Open box with a vent in the upper part).65

Figure 2-59. Experimental setup scheme, top view on the left and side view on the right.66

Figure 2-60. Homogeneous regime (left) and homogeneous layer regime (right).69

Figure 2-61. Mesh used to simulate GAMELAN.70

Figure 2-62. Numerical results of the lowest sensor of the mast 4 obtained with different meshes.71

Figure 2-63. AREVA-Concentration of helium at different time.73

Figure 2-64. AREVA-Concentration of helium registered by the sensors of the mast4.74

Figure 2-65. AREVA-Concentration of helium registered by the sensors of the mast2.74

Figure 2-66. AREVA-Concentration of helium registered by the sensors of the mast1.74

Figure 2-67. AREVA- Comparison between experimental and numerical concentration registered by the sensor of mast 1.75

Figure 2-68. AREVA- Comparison between experimental and numerical concentration registered by the sensor of mast 2.75

Figure 2-69. AREVA- Comparison between experimental and numerical concentration registered by the sensor of mast 4.76

Figure 3-1. Experiment setup open deflagration.77

Figure 3-2. Computational domain for 1 quarter experiment80

Figure 3-3. Experimentally obtained flame profiles82

Figure 3-5. Comparison between simulation and experiment at sensor 2m83

Figure 3-6. Comparison between simulation and experiment at sensor 5m84

Figure 3-7. Comparison between simulation and experiment at sensor 8m84

Figure 3-8. Comparison between simulation and experiment at sensor 18m85
 Figure 3-9. Comparison between simulation and experiment at sensor 35m86
 Figure 3-10. Comparison between simulation and experiment at sensor 80m87
 Figure 3-11. R-t diagram of the open deflagration87
 Figure 4-1. MINI RUT facility89
 Figure 4-2. Induction times92
 Figure 4-3. 3D overview of the computational domain93
 Figure 4-4. Details of geometry in computational domain93
 Figure 4-5. Comparison of pressure records at sensor P196
 Figure 4-6. Comparison of pressure records at sensor P297
 Figure 4-7. Comparison of pressure records at sensor P397
 Figure 4-8. R-t diagram of pressure98
 Figure 4-9. R-v diagram of experiment and simulation99

all rights reserved

Introduction

The main objective of this work is to perform benchmarking of the various CFD software packages available to the SUSANA partners, based on several experiments involving hydrogen release and dispersion, hydrogen deflagration and hydrogen detonation. The detailed description of the experiments and computational results are presented in the following section.

This work is part of the SUSANA project.

Release and Dispersion

1.1 GARAGE experiment

1.1.1 Experimental description

The experiments were performed by the CEA within HYSAFE project and are related to helium (instead of hydrogen for safety reasons) dispersion in a facility representative of a realistic single private garage. Test 4 as described in (Gupta et al. 2009) is chosen for this benchmarking exercise.

The GARAGE facility is situated indoors to avoid the uncertainty of the meteorological conditions. It is of rectangular shape with interior dimensions of 5.76 m (length) x 2.96 m (width) x 2.42 m (height). The internal volume of GARAGE is 40.92 m³. The maximum uncertainty in GARAGE volume calculation is of the order of $\pm 0.5\%$. The garage is equipped with a door for technical access in the back, and a tilting door on the front side (Figure 2-1).

Concerning the garage design, the choice is made of a stainless steel (Grade 304) skeleton (tubes of square section of 40mm side width), in order to obtain a great modularity of the walls (Figure 2-1 left). The material chosen for the panels is Styrodur® (2500 C), a green coloured extruded rigid polystyrene foam of 30mm thickness (40mm thickness at the floor level) as shown in Figure 2-1 (right).



Figure 2-1. Description of GARAGE set-up at CEA Saclay. GARAGE structure showing front and service door (left) and GARAGE structure equipped with Styrodur® sheets (right).

The leakage source is positioned in the middle of the GARAGE and at a height of 220 mm from the floor. The flow at the pipe exit is fully developed.

The reference point of the GARAGE is situated near the front door (at the cross section of the side wall and the floor level) as shown in figure 1 (left).

Table 2-1 summarizes the experimental parameters.

Table 2-1. Test parameters

Garage x-dimension (mm)	5760
Garage y-dimension (mm)	2960
Garage z-dimension (mm)	2420
x release (mm)	2880
y release (mm)	1480
z release (mm)	220
Exit diameter (mm)	29,7
Volumetric flow rate - STP (NL/min)	18
He mass flow rate (g/s)	0,0536
Garage Temperature T (°C)	24,1
Exit velocity (m/s)	0,47
Release Direction	Upwards
Release Type	Continuous
Release duration (s)	3740
Released volume - STP (NL)	1122
He released mass (g)	200,28
Target concentration (%)	2,94%
Total measurement time (s)	90440
Re at exit (24.1°C)	115

The test was performed in a free volume configuration, i.e. no obstacle in the garage and without ventilation. The upper vent was kept closed (Figure 2-2). The lower vent was kept open in order to maintain the test facility at constant atmospheric pressure for the duration of the tests.

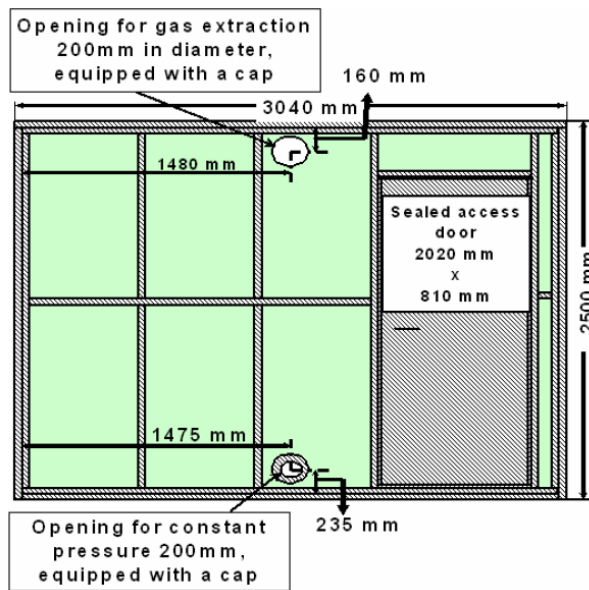


Figure 2-2. Openings (upper vent closed, lower vent open).

According to Table 2-1 the flow inside the pipe is laminar, since the Reynolds number is 115 which is below the critical value for pipe flows (~2300). However, as the jet develops the velocity will be increased due to buoyancy acceleration and thus the Reynolds number, too. Furthermore, the Reynolds critical value (transition from laminar to turbulent flow) for jets is lower than the respective for pipe flows. (Versteeg & Malalasekera 2007) suggest that Reynolds numbers above 10 would lead to turbulent jets, while (Ungate et al. 1975) refer that for non-buoyant jets Reynolds number above 500 could eventually become turbulent at some distance from the nozzle. Furthermore, (Landa & McClintock 2004) states that “It is known that, as distinct from flows in channels, jet flows are rarely, if ever, laminar”. Therefore, though the exit Reynolds number indicates laminar flow it is likely that at some distance from the nozzle the jet to become unstable and to break down into turbulent eddies.

For an extensive concentration measurement, 64 monitoring points were used inside the GARAGE test facility. Figure 2-3 displays the location of the sensors inside the GARAGE. In Table 2-2 the sensors’ coordinates are shown.

Table 2-2. Sensors coordinates.

Sensor name	x (mm)	y (mm)	z (mm)
M1N1	-1000	1001	315
M1N2	-1000	1001	630
M1N3	-1000	1002	945
M1N4	-1000	1000	1260
M1N5	-1000	995	1575
M2N1	-1000	1957	315
M2N2	-1000	1959	630
M2N3	-1000	1960	945
M2N4	-1000	1958	1260

M2N5	-1000	1955	1575
M3N1	-2920	1002	315
M3N2	-2920	1003	630
M3N3	-2920	1004	945
M3N4	-2920	1000	1260
M3N5	-2920	1001	1575
M4N1	-2915	1960	315
M4N2	-2915	1961	630
M4N3	-2915	1958	945
M4N4	-2915	1959	1260
M4N5	-2915	1960	1575
M5N1	-4840	1010	315
M5N2	-4840	1009	630
M5N3	-4840	1005	945
M5N4	-4840	1003	1260
M5N5	-4840	1002	1575
M6N1	-4835	1960	315
M6N2	-4835	1959	630
M6N3	-4835	1959	945
M6N4	-4835	1958	1260
M6N5	-4835	1957	1575
P1N1	-190	155	1900
P1N2	-190	151	2135
P1N3	-190	150	2370
P2N1	-151	1480	1900
P2N2	-151	1480	2135
P2N3	-150	1480	2350
P3N1	-190	2817	1900
P3N2	-190	2815	2135
P3N3	-192	2813	2370
P4N1	-2965	152	1900
P4N2	-2968	152	2135
P4N3	-2970	158	2370
P5N1	-2971	1485	1900
P5N2	-2972	1480	2135
P5N3	-2974	1480	2350
P6N1	-2981	2810	1900
P6N2	-2979	2810	2135
P6N3	-2976	2810	2370
P7N1	-5602	150	1900
P7N2	-5603	150	2135
P7N3	-5608	150	2370
P8N1	-5593	1483	1900
P8N2	-5596	1481	2135
P8N3	-5604	1483	2370
P9N1	-5606	2810	1900

P9N2	-5609	2811	2135
P9N3	-5606	2810	2370
Vo11	-5740	1480	235
Vo12	-5745	1030	2315
Vo13	-5745	1030	2295
Vo14	-5745	1030	2275
Vo15	-5745	1030	2255
Vo16	-5745	1030	2235
Vo17	-5745	1030	2215

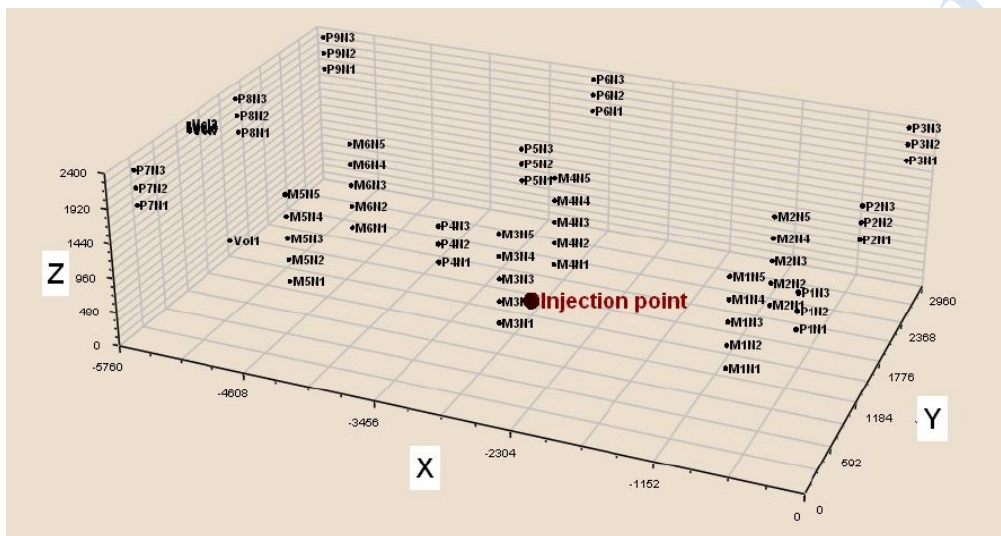


Figure 2-3. Sensor location.

1.1.2 Modeling approach

Five partners participated in the present benchmark: AREVA, JRC, NCSR UU and EE. The following Sections present the modeling approach for each partner.

1.1.2.1 AREVA

The main parameters of the CFD simulations are:

- CFD code: MERLIN (home code of INERIS establish on MATLAB)
- Isothermal simulation.
- Source modelled as a 2D
- Symmetry is assumed. Simulation made on a half domain
- The computational domain outside the box is extended in all the three directions to avoid boundary conditions at the opening.
- Model used: low Reynolds $k-\omega$

1.1.2.1.1 Governing equations

To simulate the experiments, a three dimensional calculation was performed using “Non-reacting flows” solver of the numerical toolbox MERLIN.

The equations were slightly modified to introduce the buoyancy terms both in the averages equations and in the turbulence equations:

❖ Mass equation

$$\frac{\partial \bar{\rho}}{\partial t} + \frac{\partial \bar{\rho} \tilde{u}}{\partial x} + \frac{\partial \bar{\rho} \tilde{v}}{\partial y} + \frac{\partial \bar{\rho} \tilde{w}}{\partial z} = 0 \quad [1]$$

❖ Momentum equation following the x direction

$$\frac{\partial \bar{\rho} \tilde{u}}{\partial t} + \frac{\partial \bar{\rho} \tilde{u}^2}{\partial x} + \frac{\partial \bar{\rho} \tilde{u} \tilde{v}}{\partial y} + \frac{\partial \bar{\rho} \tilde{u} \tilde{w}}{\partial z} = -\frac{\partial \bar{P}}{\partial x} + (\mu_l + \mu_t) \left[\frac{\partial^2 \tilde{u}}{\partial x^2} + \frac{\partial^2 \tilde{u}}{\partial y^2} + \frac{\partial^2 \tilde{u}}{\partial z^2} \right] \quad [2]$$

❖ Momentum equation following the y direction

$$\frac{\partial \bar{\rho} \tilde{v}}{\partial t} + \frac{\partial \bar{\rho} \tilde{u} \tilde{v}}{\partial x} + \frac{\partial \bar{\rho} \tilde{v}^2}{\partial y} + \frac{\partial \bar{\rho} \tilde{v} \tilde{w}}{\partial z} = -\frac{\partial \bar{P}}{\partial y} + (\mu_l + \mu_t) \left[\frac{\partial^2 \tilde{v}}{\partial x^2} + \frac{\partial^2 \tilde{v}}{\partial y^2} + \frac{\partial^2 \tilde{v}}{\partial z^2} \right] \quad [3]$$

❖ Momentum equation following the z direction

$$\begin{aligned} & \frac{\partial \bar{\rho} \tilde{w}}{\partial t} + \frac{\partial \bar{\rho} \tilde{u} \tilde{w}}{\partial x} + \frac{\partial \bar{\rho} \tilde{v} \tilde{w}}{\partial y} + \frac{\partial \bar{\rho} \tilde{w}^2}{\partial z} \\ & = -\frac{\partial \bar{P}}{\partial z} + (\mu_l + \mu_t) \left[\frac{\partial^2 \tilde{w}}{\partial x^2} + \frac{\partial^2 \tilde{w}}{\partial y^2} + \frac{\partial^2 \tilde{w}}{\partial z^2} \right] + g(\rho - \rho_a) \end{aligned} \quad [4]$$

As previously, we decide to not resolve the energy equation because the rejected helium has the same temperature as the ambient air.

Given that Helium is injected in the air, the system of equation has to contain the species equation to take into account the apportionment of Helium in the chamber.

❖ Species equation

$$\begin{aligned} & \frac{\partial \bar{\rho} \tilde{C}}{\partial t} + \frac{\partial \bar{\rho} \tilde{u} \tilde{C}}{\partial x} + \frac{\partial \bar{\rho} \tilde{v} \tilde{C}}{\partial y} + \frac{\partial \bar{\rho} \tilde{w} \tilde{C}}{\partial z} \\ & = \frac{\partial}{\partial x} \left[\left(\bar{\rho} D_1 + \frac{\mu_t}{Sc_t} \right) \frac{\partial \tilde{C}}{\partial x} \right] + \frac{\partial}{\partial y} \left[\left(\bar{\rho} D_1 + \frac{\mu_t}{Sc_t} \right) \frac{\partial \tilde{C}}{\partial y} \right] \\ & \quad + \frac{\partial}{\partial z} \left[\left(\bar{\rho} D_1 + \frac{\mu_t}{Sc_t} \right) \frac{\partial \tilde{C}}{\partial z} \right] \end{aligned} \quad [5]$$

In reality, the k-ε model is valid, strictly speaking, far from wall boundaries. For the boundaries layers flows, the model does not provide damping for the turbulent parameters in the near boundary region and in fact, the application of the model as it is, for the boundary layer flows lead to the wrong profiles of velocity (more precisely, the velocity profile does not follow the well know “boundary law”) which may impact the helium concentration prediction, especially at sensor M4N1, given that it is located at 110 mm below of the output of the injection tube (in the boundary layer) where the effect of viscosity may be preponderant in view of the weak Reynolds number in that region (the injection is not directed in that region, it is rather the gravity effect which favors the drop of helium until the position of the sensor M4N1). The same

ascertainment is done for the sensor M1N5 and M2N5 not because of the Reynolds number but rather their proximity to the upper wall.

An alternative consists in using the low Reynolds number k-epsilon model which resolves the flow everywhere. It contains two damping terms, f_2 and f_μ : the function f_2 that appears in the term of “dissipation of the dissipation” (see chapter 3 of the Ph.D thesis memory, (Kone, Ph.D in progress)) considers the effects of the low local Reynolds number near to the boundary, which contributes to the growth of ϵ in this zone; the function f_μ which intervenes in the calculation of μ_t (turbulent viscosity) is a damping function permitting to quickly decrease the turbulent viscosity in the zone of near boundary. It is a logical extension of the standard k-epsilon model and shares many of its advantages, but uses more memory.

In view of the reasons given above, the low Reynolds number k-epsilon model is retained for this simulation and the two transport equations that compose this model are written as follow:

$$\frac{\partial(\bar{\rho}k)}{\partial t} + \frac{\partial(\bar{\rho}\tilde{u}_j k)}{\partial x_j} = \bar{\rho}\tau R_{ij} \frac{\partial \tilde{u}_i}{\partial x_j} - \bar{\rho}\epsilon^* + P_b + \frac{\partial}{\partial x_j} \left[\left(\mu + \frac{\mu_t}{\sigma_k} \right) \frac{\partial k}{\partial x_j} \right] - D \quad [6]$$

$$\begin{aligned} \frac{\partial(\bar{\rho}\epsilon^*)}{\partial t} + \frac{\partial(\bar{\rho}\tilde{u}_j \epsilon^*)}{\partial x_j} &= C_{\epsilon 1} \frac{\bar{\rho}\epsilon^*}{k} \left(\tau R_{ij} \frac{\partial \tilde{u}_i}{\partial x_j} + C_{3\epsilon} P_b \right) - C_{\epsilon 2} f_2 \bar{\rho} \frac{\epsilon^{*2}}{k} + \frac{\partial}{\partial x_j} \left[\left(\mu + \frac{\mu_t}{\sigma_\epsilon} \right) \frac{\partial \epsilon^*}{\partial x_j} \right] \\ &+ E \end{aligned} \quad [7]$$

In these equations,

ϵ^* is a transformed variable introduced by Jones and Launder and it is written:	$\epsilon^* = \epsilon - 2\nu \left(\frac{\partial k^{\frac{1}{2}}}{\partial y} \right)^2$	[8]
D is an additional dissipation term and it is written:	$D = \bar{\rho}\epsilon - \bar{\rho}\epsilon^*$	[9]
μ_t is the turbulent viscosity and it is written:	$\mu_t = C_\mu f_\mu \bar{\rho} \frac{k^2}{\epsilon}$	[10]
E is an additional turbulence production term and it is written:	$E = 2 \frac{\mu\mu_t}{\bar{\rho}} \left(\frac{\partial^2 u_i}{\partial x_j \partial x_k} \right) \left(\frac{\partial^2 u_i}{\partial x_j \partial x_k} \right)$	[11]
f_2 is the damping factor and it is written:	$f_2 = 1 - 0.3 \exp(-R_t^2)$	[12]
f_μ is also a dumping factor and it is written:	$f_\mu = \exp \left(\frac{-2.5}{1 + \frac{R_t}{50}} \right)$	[13]

<p>R_t is the turbulent Reynolds number and it is written:</p>	$R_t = \frac{k^2}{\nu \varepsilon}$	<p>[14]</p>
<p>P_b is the term linked to buoyancy and it is written:</p>	$P_b = - \frac{\mu_t}{\rho S c_t} g \nabla \rho$ <p>$S c_t$ is the turbulent Schmidt number and its value is 0.7 in this study.</p>	<p>[15]</p>

It is important to underline that in the case where one used the modified dissipation ε^* instead of the true dissipation ε , the conservation equation for k must be modified by including an additional term of dissipation D . Moreover, it is necessary to add to the equation of ε^* an additional term of production denoted E whose role is to increase the rate of dissipation in the buffer regions of the boundary layer in order to ensure a correct value of the maximum of k in the profile.

1.1.2.1.2 Mesh generation

In the simulations the vent is not modeled. The facility is assumed fully closed. Given that the domain presents two planes of symmetry for the simulation and it is possible to use the quarter of the domain.

Knowing that the actual version of MERLIN doesn't consider more than one plane of symmetry, for the simulation of garage, we are going to use the same kind of mesh used for GAMELAN (see Section 2.2.3).

The zones to be meshed finely are the plume zone and the upper part of the chamber. The plume zone is meshed with an expansion of 12 degree, going from the origin of the jet to the ceiling which can represent the angle of jet expansion. The other parts of the chamber are meshed less finely. In Figure 2-4, the mesh used for this simulation is represented.

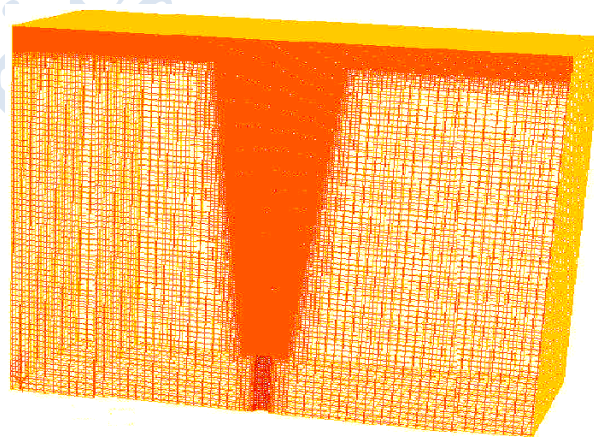


Figure 2-4. AREVA-Mesh used to simulate the rejection in the garage.

The mesh presented in the Figure 2-4 has been retained for this study after a study of sensitivity which proved that the convergence in mesh has been reached. Concretely,

the helium rejection in the garage has been simulated using in total 25,677,145 cells which can be decomposed as follow:

- 10,555,145 cells for the plume and the upper part of the chamber with 88 nodes at the injection diameter.
- 15,122,000 cells in the other parts of the domains.

1.1.2.1.3 Initial and boundary conditions

At the entrance of the helium jet:

- The ambient pressure (atmospheric pressure) is defined;
- The turbulence intensity is supposed to be 1%;
- The mass flow is imposed at the entrance (In each case, it is the global value of the mass flow which is imposed).
- The volume fraction of helium is supposed to be 1.
- An ambient temperature (273.15 K) is imposed at the entrance.

On the walls, the zero pressure gradient condition has been applied.

It is interesting to note that at the beginning of the injection, the chamber contains air in Standard Temperature and Pressure (STP) conditions.

1.1.2.1.4 Discretization of the system of equations

Without further indications, to solve the RANS equations, the time derivatives are first order solved explicitly. For the convective terms, FCT (Flux Corrected Transport) numerical scheme was used (Lax-Wendroff scheme for the high order flux estimator and Lax-Frederichs scheme for the low order flux estimator). A central derivation scheme is issued for the diffusive terms.

1.1.2.2 JRC

Main parameters of the CFD simulations:

- CFD code: ANSYS CFX 15.5
- Isothermal simulation. (garage $T = 24.1^{\circ} \text{C}$)
- Source modelled as a 3D pipe.
- Inlet mass flow rate = 0.05355 g/s
- Multicomponent flow model: the code assumes that the various components of a fluid are mixed at the molecular level and that they share the same mean velocity, pressure and temperature fields, and that mass transfer takes place by convection and diffusion.
- The computational domain outside the box is extended in all the three directions to avoid boundary conditions at the opening.
- Turbulent models:
 - SST Transitional model as fluid model: The $k-\omega$ based Shear-Stress-Transport (SST) model was originally designed to give highly accurate predictions of the onset and the amount of flow separation under adverse pressure gradients by the inclusion of transport effects into the formulation of the eddy-viscosity.

This results in a major improvement in terms of flow separation predictions but not only. The full transition model is based on two transport equations, one for the intermittency and one for the transition onset criteria in terms of momentum thickness Reynolds number. It is called 'Gamma Theta Model' and it is the recommended transition model for general-purpose applications. It uses a new empirical correlation (Langtry and Menter) which has been developed to cover standard bypass transition as well as flows in low free-stream turbulence environments. This built-in correlation has been extensively validated together with the SST turbulence model for a wide range of transitional flows.

- DES model: the idea behind the Detached Eddy Simulation model of Strelets is to switch from the SST-RANS model to an LES model in regions where the turbulent length predicted by the RANS model is larger than the local grid spacing. In this case, the length scale used in the computation of the dissipation rate in the equation for the turbulent kinetic energy is replaced by the local grid spacing.
- Advection scheme: High resolution.
- Transient scheme: Second order backward Euler.

Mesh strategy

The detail of the adopted mesh (i.e. mesh #1, mesh #2, mesh #2.b, mesh #3, mesh #4, mesh #5) at the symmetry plane are reported in the following figures. Information about the number of nodes is reported in Table 2-3. The H and T letters in the fifth column of Table 2-3 indicate the type of mesh, i.e. H is hexahedral and T is tetrahedral.

Table 2-3. JRC-List of the simulations performed

Sensitivity simulation (7500 s)

	#	# Mesh	n. of nodes			Comp. time	Sim. time	n. of CPUs	TS	T.Model	
			Garage	Out	TOT						
a	1	1	0.10 M	H+T	5700	0.11 M	0d 19h 15m	7500 s	15	1 s	SST trans
b	2	2	0.46 M	H+T	5700	0.47 M	10d 23h 31m	7500 s	45	0.1 s	SST trans
c	3	3	2.85 M	H+T	5700	2.86 M	6d 46h 52m	7500s	45	1 s	SST trans
d*	4	2	0.46 M	H+T	5700	0.47 M	-	7500 s	45	1 s	SST trans
e	5	2	0.46 M	H+T	5700	0.47 M	1d 07h 51m	7500 s	15	5 s	SST trans
f	6	2.b	0.46 M	H+T	8700	0.47 M	1d 17h 10m	7500 s	30	1 s	SST trans
g	7	4	0.54 M	H*	5700	0.55 M	2d 06h 50m	7500 s	30	1 s	SST trans
h	8	5	0.69 M	H	5700	0.70 M	2d 21h 43m	7500 s	30	1 s	SST trans

* This case is actually the same as case i9.

I	12	6	0.14 M	T	5700	0.55 M	0d 14h 47m	7500 s	45	1 s	SST trans
m	13	5	0.69 M	H	5700	0.70 M	1d 03h 16m	7500 s	45	1 s	LAM
o	14	1	0.10 M	H+T	5700	0.11 M	0d 09h 13m	7500 s	45	1 s	LAM
p	15	2	0.46 M	H+T	5700	0.47 M	0d 22h 59m	7500 s	45	1 s	LAM
q	16	3	2.85 M	H+T	5700	2.86 M	6d 21h 36m	7500s	45	1 s	LAM
r	17	1	0.10 M	H+T	5700	0.11 M		7500 s	45	1 s	DES
s	18	3	2.85 M	H+T	5700	2.86 M		7500s	45	1 s	DES

Full simulations (20000 s)

		n. of nodes									
	#	# Mesh	Garage		Out	TOT	Comp. time	Sim. time	n. of CPUs	TS	T.Model
i	9	2	0.46 M	H+T	5700	0.47 M	2d 07h 44m	20000 s	45	1 s	SST trans
j	10	2	0.46 M	H+T	5700	0.47 M	1d 21h 24m	20000 s	45	1 s	LAM
k	12	2	0.46 M	H+T	5700	0.47 M	2d 06h 34m	20000 s	45	1 s	DES

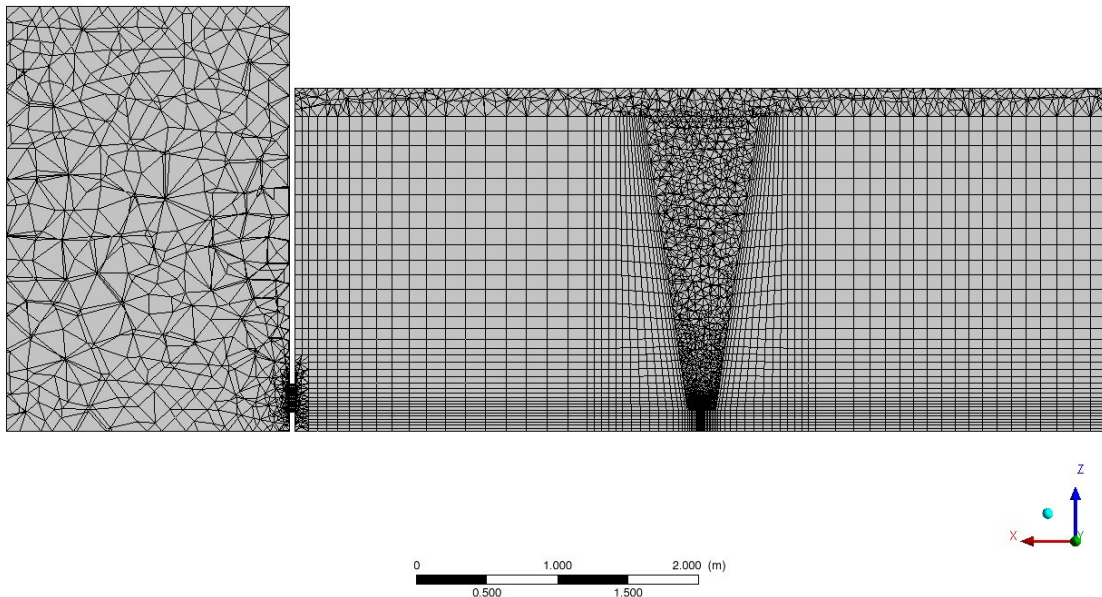


Figure 2-5. JRC-Detail of the mesh at symmetry plane for mesh #1

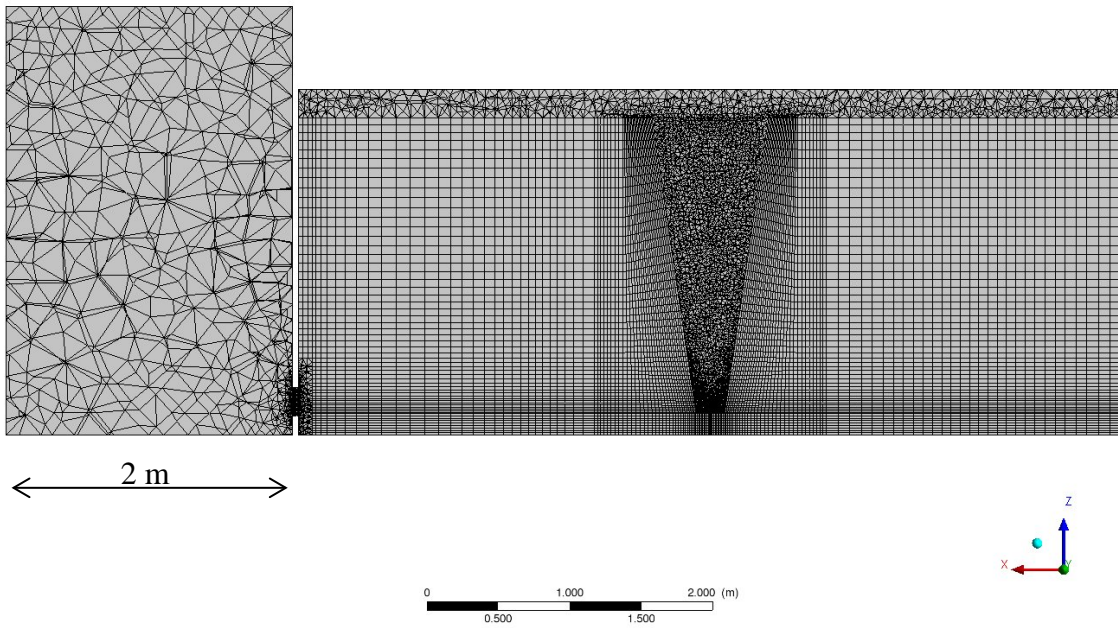


Figure 2-6. JRC-Detail of the mesh at symmetry plane for mesh #2

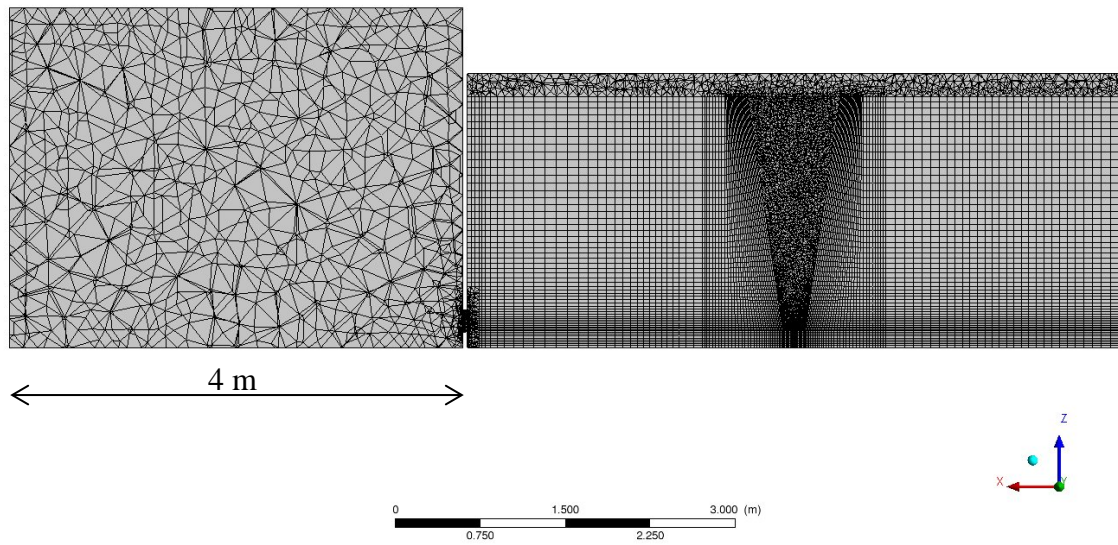


Figure 2-7. JRC-Detail of the mesh at symmetry plane for mesh #2.b

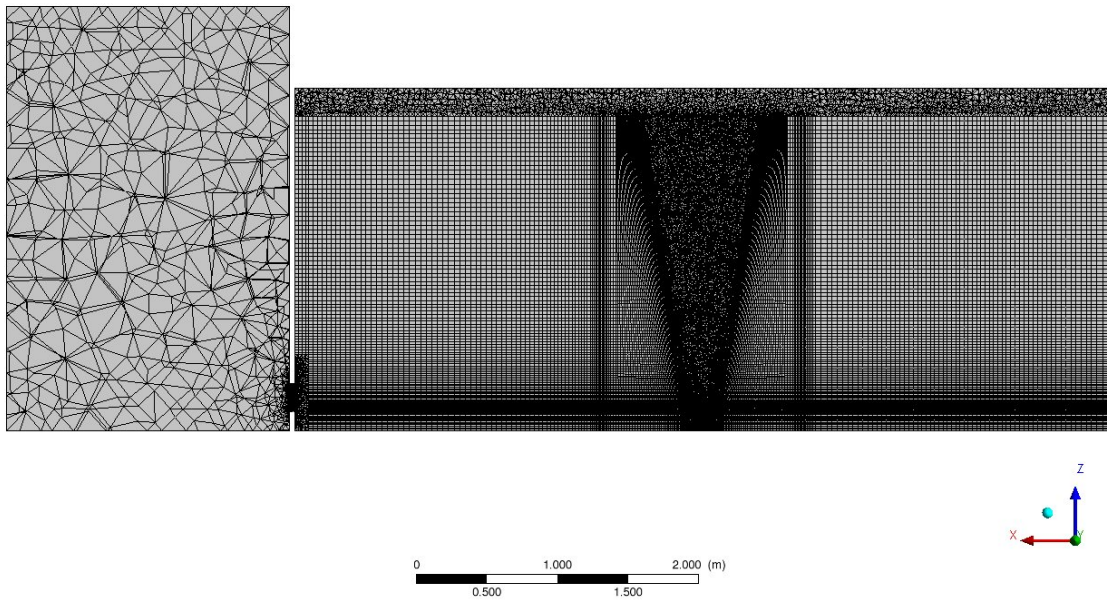


Figure 2-8. JRC-Detail of the mesh at symmetry plane for mesh #3

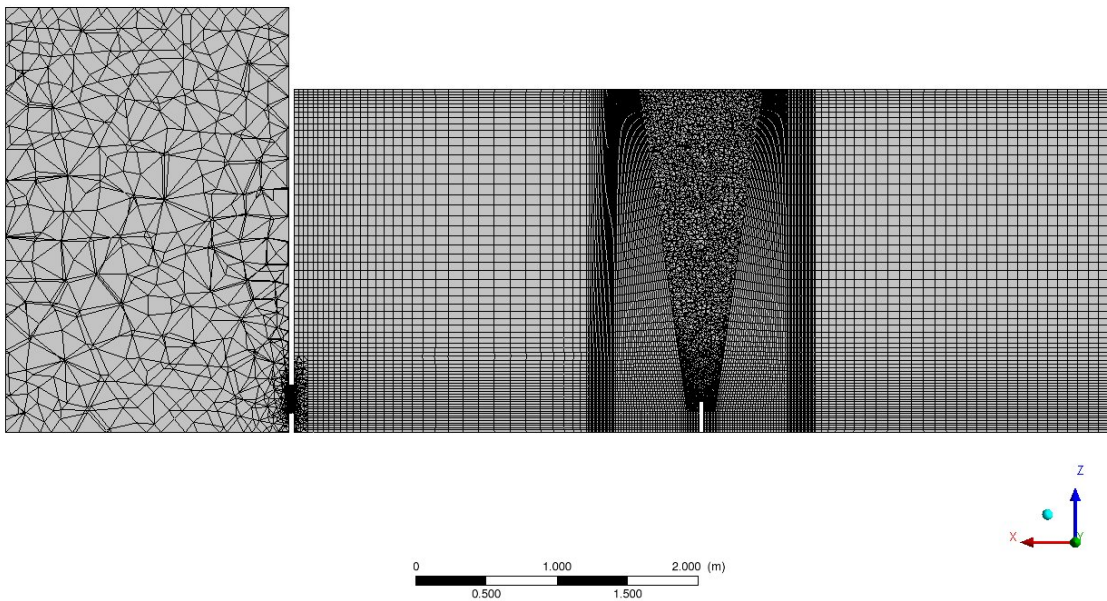


Figure 2-9. JRC-Detail of the mesh at symmetry plane for mesh #4

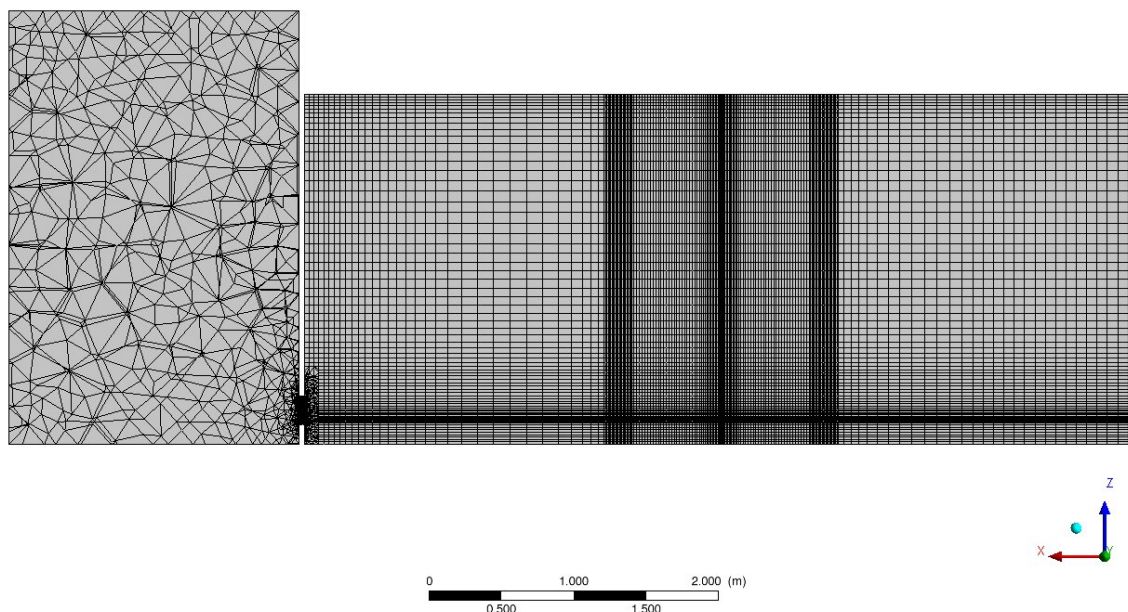


Figure 2-10. JRC-Detail of the mesh at symmetry plane for mesh #5

The details of the inlet boundary meshes are reported in Figure 2-11

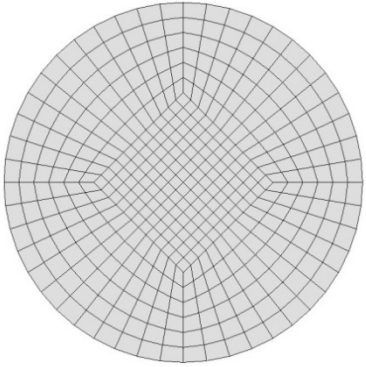
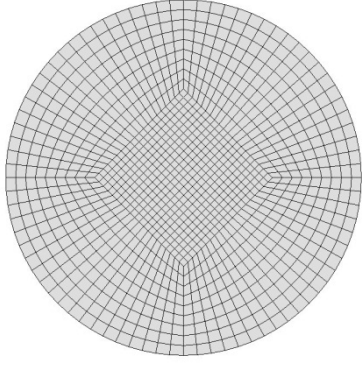
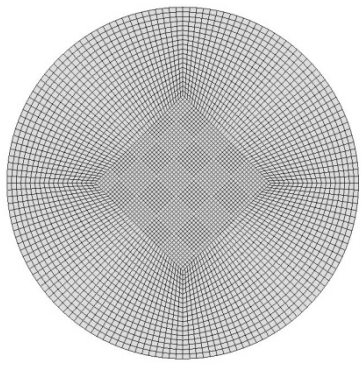
		
Mesh #1 n. of nodes on the circumference 56	Mesh #2, Mesh #2.b, Mesh #4, Mesh #5 n. of nodes on the circumference 80	Mesh #3 n. of nodes on the circumference 160

Figure 2-11. JRC-Details of the inlet boundary meshes

1.1.2.3 NCSR D

Description of the numerical methods used in the calculations:

- ADREA-HF CFD code
- Turbulence models that were tested:
 - Laminar model
 - k- ϵ model with extra buoyancy terms
 - RNG-LES
- 1st order fully implicit scheme for time integration in the case of laminar and k- ϵ model, 2nd order fully implicit scheme in the case of RNG-LES model
- Convective terms: MUSCL TVD scheme in the case of laminar and k- ϵ model, Central Differences in the case of RNG-LES model
Diffusive terms: Central Differences
- Isothermal conditions (297.25 K)
- CFL \leq 10 restriction for laminar and k- ϵ model and CFL \leq 0.9 for RNG-LES model. These values were proved to be the independent ones from the time step sensitivity study (see Section 2.1.3.3).

The information about the computational domain and grid are given in Section Sensitivity studies. Cartesian structured grid is used. As far as the boundary conditions is concerned, wall boundaries are applied on the walls, bottom and ceiling. In the simulations with laminar model and k- ϵ model at the side open boundaries (y-planes) zero gradient boundary conditions were imposed for all variables. On the top boundary the constant pressure boundary condition was applied. In the simulations with RNG-LES model non reflective boundary conditions were applied at all open boundaries.

1.1.2.4 UU

In this study CFD model with two sub-models of non-reacting incompressible flow were applied to simulate helium sub-sonic release and dispersion in the enclosure with one vent following CEA test (Gupta et al. 2009) and using ANSYS FLUENT software.

The governing equations for simulation of gas release and dispersion of non-reacting flow for CFD model applied here i.e. Large Eddy Simulation (LES) model for simulation of turbulence with two sub-grid-scale (SGS) models Dynamic Smagorinsky-Lilly and renormalized group theory (RNG). Specific features and governing equations of these models described in details in (Molkov & Shentsov 2014) and (Bragin et al. 2013) respectively. Both models have shown good results in former studies.

Description of the numerical methods used in the calculations:

- Software: ANSYS Fluent 14.5
- Type of solver: Incompressible Pressure-Based
- Pressure-Velocity coupling : SIMPLE
- Spatial Discretization :
 - Gradient: Least Squares Cell Based
 - Pressure : Standard
 - Momentum : Bounded Central Differencing
 - Turbulent dissipation rate: Second Order Upwind
 - Helium : Second order upwind
 - Energy : Second Order Upwind
- Transient scheme: Bounded Second Order Implicit

The calculation CPU rate seconds of real release time per hour of calculation together with *CFL* number and time steps are outlined in Table 1. Time step is limited to 0.02 s in simulations 2-5 to keep $CFL=U\Delta t/\Delta x=0.47\cdot 0.02/0.01=0.94$, below 1 and to avoid divergence problems. Where *U* is release velocity (m/s), Δt is the time step (s), Δx is the cell size at the release point (m). In fact this *CFL* number valid only for the flow in the pipe where the initial velocity is 0.47 m/s. When the gas exits the pipe it starts to accelerate due to buoyancy resulting in higher *CFL* above the pipe even if the grid becomes coarser. Table 2-4 shows maximum *CFL* numbers for each calculation. It can be seen from the table that the maximum *CFL* numbers for the same time step size and different grid sizes are very close. This is due to that fact that the flow accelerates at about the same distance from the pipe where the grid size is very close and didn't increased yet. In all simulations the time step after termination of release at 3740 s was increased to 0.2 s in order to save time.

Table 2-4. UU-Parameters of numerical simulations.

No.	Grid	Δt , s	<i>CFL</i>	Model applied	Number of cores	CPU rate, s/h
1	1	0.2	35	LES Dynamic S-L	64	67.4
2	1	0.02	4.4	LES Dynamic S-L	64	4.4

3	1	0.02	4.0	LES RNG	64	5.8
4	2	0.02	5.7	LES Dynamic S-L	64	9.0
5	3	0.02	5.1	LES Dynamic S-L	64	6.5

Initial and boundary conditions, model constants

Initial temperature of released helium and air temperature in the domain were set to values specified in experimental description. Non-slip boundary conditions were applied to all solid surfaces. Release was initiated through the velocity inlet boundary condition with 100% of helium and constant velocity throughout the inlet cross-section. Initial inlet turbulence intensity and length scale were calculated from equations $I=0.16Re^{-1/8}$ and $L=0.07d$ respectively. Initial velocities were set to zero in the whole calculation domain. The “pressure outflow” condition was set at the domain boundaries with the same temperature as in the domain and gauge pressure equal to zero. The main constants in applied models are as follows: LES ($Sc_t=0.7$, C_S is calculated dynamically).

1.1.2.5 EE

Main parameters of the CFD simulations:

- CFD code: FDS Version 6
- Isothermal simulation. (garage $T = 24.1^\circ \text{C}$)
- Source modelled as a surface boundary condition
- Inlet mass flow rate = 0.05355 g/s
- Walls: Adiabatic boundary condition applied.
- Opening: Initial studies indicated flow velocities at the opening are very low (order 0.1m/s and the buoyant He plume outside of the box rises very quickly. This indicated that a computational domain outside the box is required, but this can be of limited extent (0.2m in x and y direction).
- Turbulent models: FDS uses a time-accurate approach with a LES turbulence model.
- 2nd order accurate evaluation of spatial differences (using Superbee TVD flux limiter)
- Transient scheme: explicit 2nd order accurate

Mesh Strategy

FDS uses a Cartesian mesh which allows mesh refinement in areas where high gradients need to be captured. Initial flow studies revealed a number of key flow features which determined the meshing strategy including:

- Lateral extent of the rising He plume – indicating the region where higher gradients occurred
- Acceleration of the flow after injection: buoyancy causes the He-air mixture to accelerate above the release point.
- Velocity at opening was found to be very low, and the He plume outside of the box is largely buoyancy driven rather than momentum driven (i.e. in contrast to a higher velocity jet emitting from the vent). This indicates that a 3-D domain outside the box is required to capture flow features but that this can be limited in extent.

Table 2-5. EE- List of the simulations performed.

Mesh	Cells	Sim. time (s)	Computer time (h)	CPUs	Mix Dx	Max CFL
A-coarse	75,264	15,000	6	12	.04	1
B-medium	103,936	15,000	24	12	.02	1
C-fine	116,224	15,000	72	12	.01	1

Due to the strategic approach to grid refinement (informed by initial runs), the overall number of cells does not increase significantly; however the level of refinement in key grid areas doubles as the grid is refined. This does mean that timesteps are reduced by 50% at each grid refinement level and run times increase by more than a factor of two because of: timestep reduction; increase in grid cell number, and also better resolution of the velocity flow field leading to higher (buoyancy induced) velocity in the region above the inlet. In fact, from an initial inflow velocity of 0.47m/s, a maximum velocity of 1.5m/s was observed.

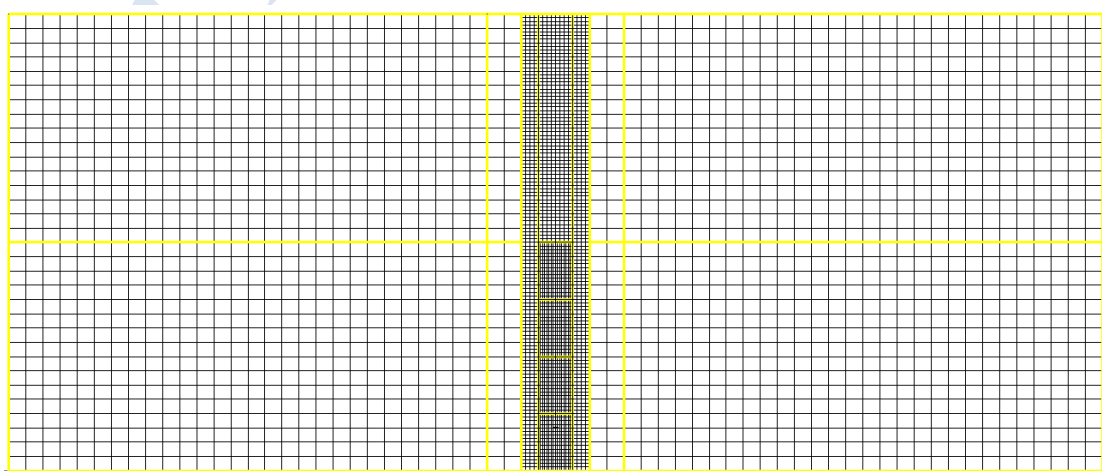
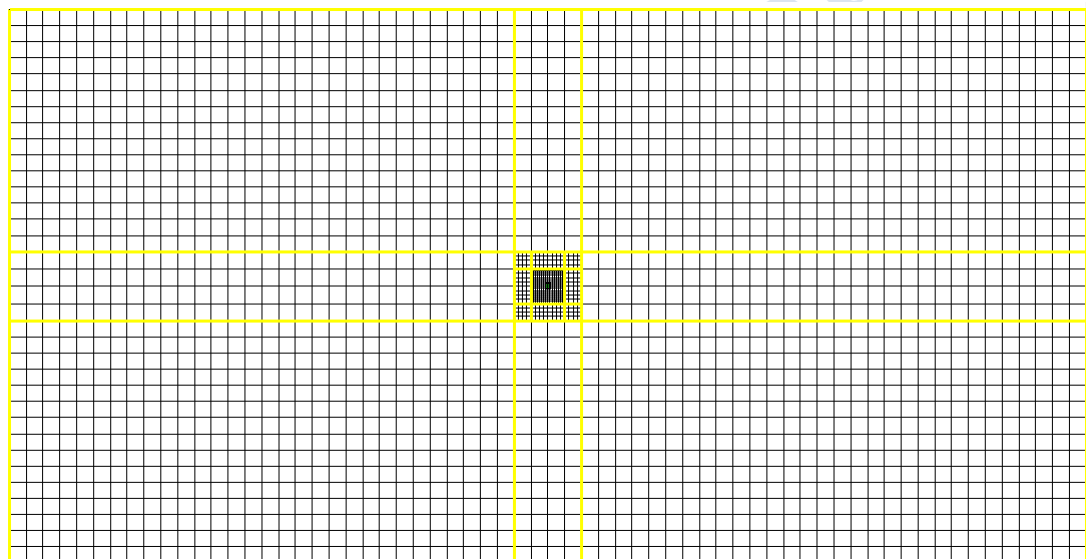


Figure 2-12. EE- Mesh inside garage showing three levels of mesh refinement: Plan view above, side elevation below. Refinement regions outlined in yellow. Mesh outside garage not show.

1.1.3 Sensitivity studies

According to “Best Practice in Guidelines in numerical simulations” (SUSANA D3.1, 2014) several sensitivity studies should be performed, in order assure that the computational results are unaffected by numerical errors. The most important sensitivity study is the grid independency study. Other sensitivity studies, such as domain and time step sensitivity studies are also useful.

In this Section the sensitivity studies that each partner performed are presented. From the sensitivity studies the grid, domain etc. that provides independent results is obtained and these results are then compared to the experiment and with each other in Section “Results and discussion”.

1.1.3.1 AREVA

Four grid size samples have been chosen to investigate the grid size effect on the results and are shown in Table 2-6.

Table 2-6. AREVA-The main characteristics of the grids that were tested.

Meshes	Number of cells in the plume and the upper part of the chamber	Number of cells in the other part of the chamber	Number of nodes at the injection diameter	Total number of cells
Mesh1	2,154,820	3,578,214	20	5,733,034
Mesh2	5,584,620	8,244,520	47	13,829,140
Mesh3	10,555,145	15,122,000	88	25,677,145
Mesh4	11,253,882	16,252,320	93	27,506,202

The numerical result obtained for the third sensor (going from the bottom) of the mast 1 for the different meshes represented in Table 2-6 are displayed in Figure 2-13.

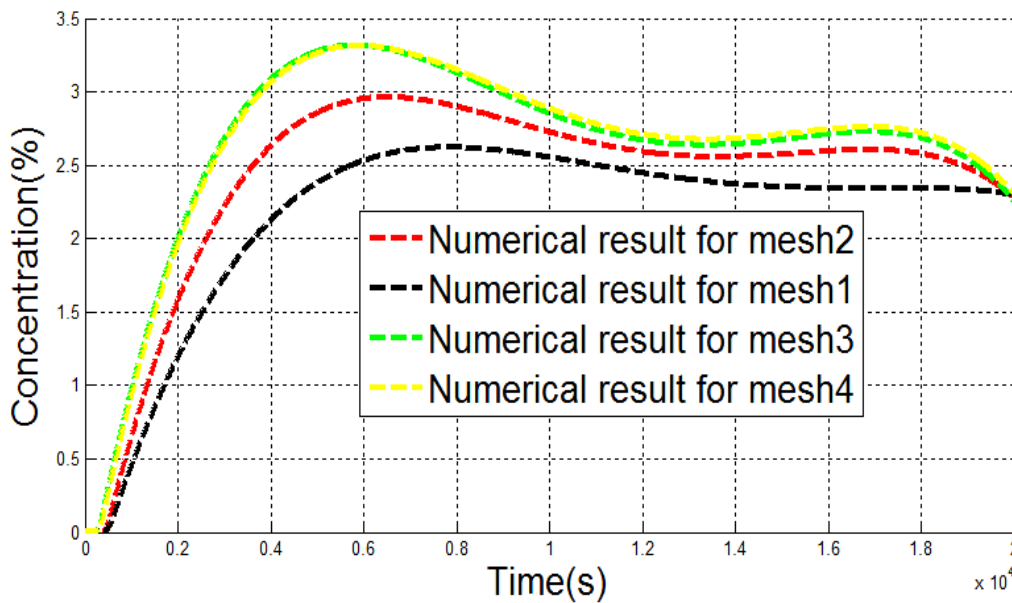


Figure 2-13. AREVA- Numerical results of the third sensor (going from the bottom) of the mast 1 obtained with different meshes.

According to Figure 2-13 it is clear that the convergence in mesh is obtained for mesh3 given that the finer mesh (mesh4) gives identical results. Therefore, mesh3 is the independent mesh.

1.1.3.2 JRC

JRC performed grid independency study using the SST transitional model, the laminar model and the DES model.

Table 2-3 summarizes the simulations that were performed for all grid sensitivity studies. Figure 2-5-Figure 2-10 show the meshes that were used. In all simulations for the grid sensitivity studies the time step was equal to 1 s. Figure 2-14 shows the results of the grid independency study with the SST model. It should be highlighted here that the meshes in cases a, i, c consist of both hexahedral and tetrahedral cells. The mesh in case g has tetrahedral cells only in a conical region similar to the jet cone and it does not consist of tetrahedral cells on the top, whereas the mesh in case h consists only of hexahedral cells.

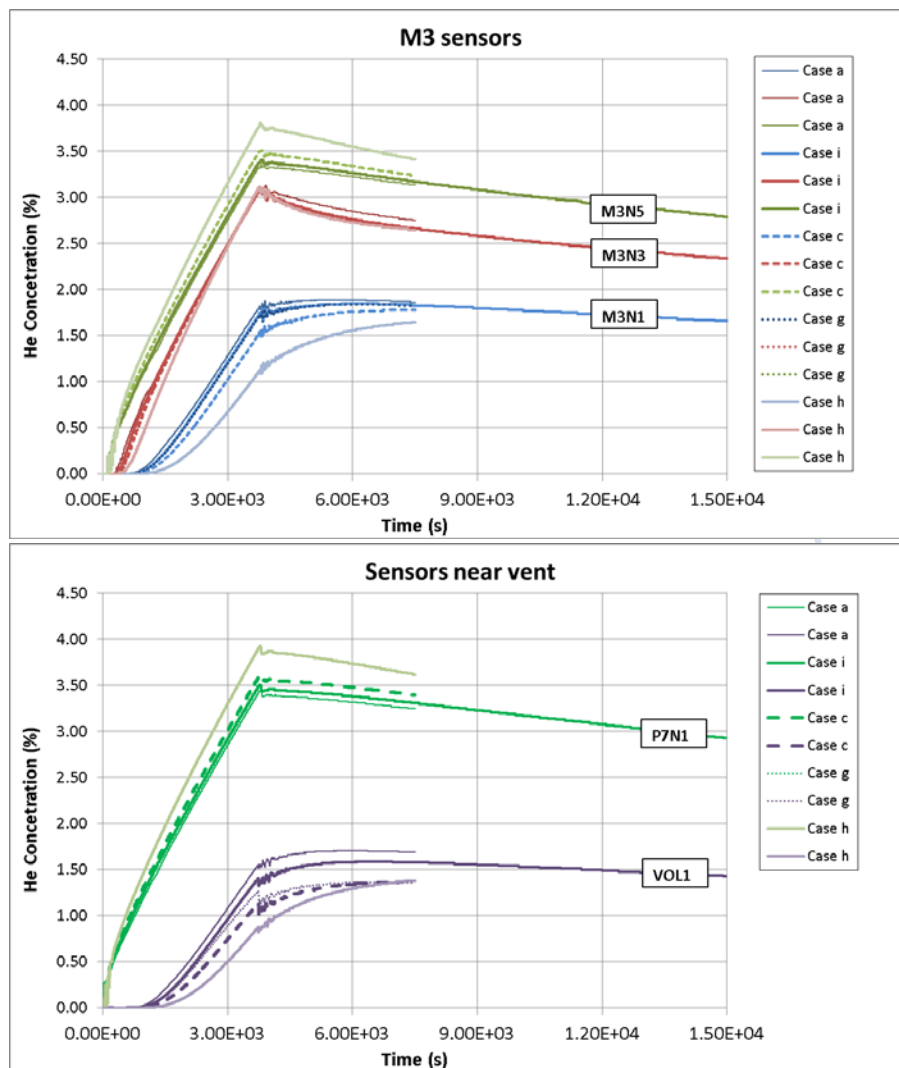


Figure 2-14. JRC-The results from the grid sensitivity study using the SST model.

Comparing the cases a, i and c, which consist of both hexahedral and tetrahedral cells, but consist of larger number of nodes respectively, there are small differences at most of the sensors. The largest differences are detected at the sensors near the vent. Case g, which has different design of hexa and tetra cells, but similar total number of nodes with case i gives almost identical results with case i, except for the sensor in the hole (Vol1), where small discrepancies are observed.

Figure 2-15 shows the results for cases i, I and h. In these cases the mesh type is different with case i to use both hexa and tetra cells, case I only tetra cells and case h only hexa cells. The results with tetra mesh seem to deviate from the experiment the most producing lower concentrations at the bottom sensors.

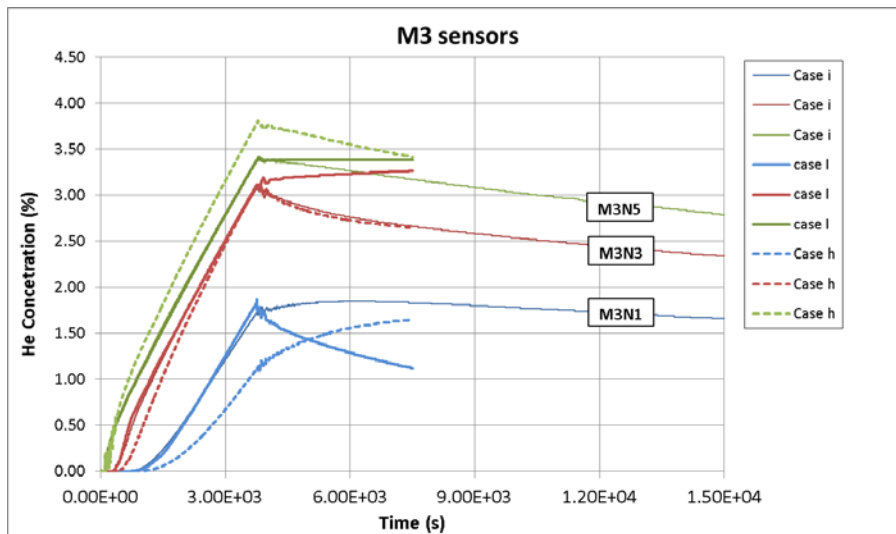
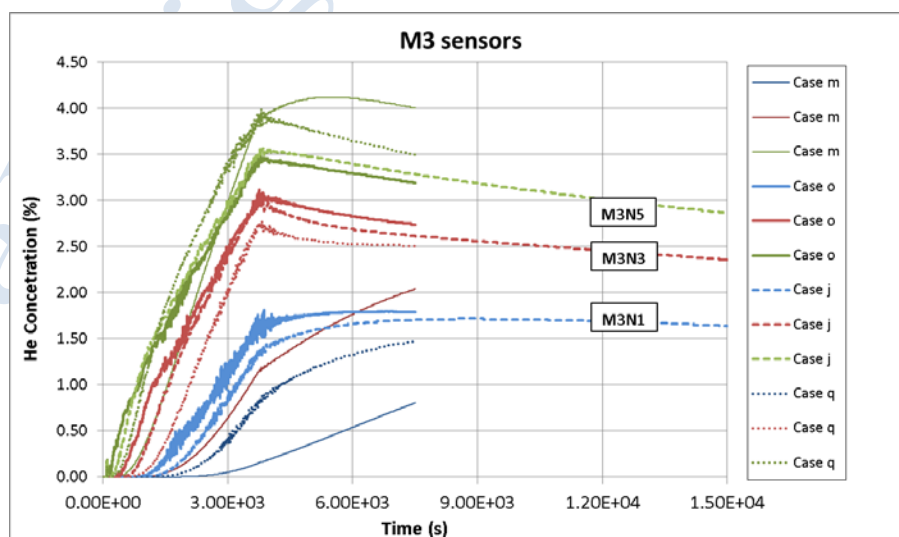


Figure 2-15. JRC-The results from the grid sensitivity study using the SST model.

In general, it is shown that all cases except case h and l, which consist only of hexahedral cells and tetrahedral cells, respectively, are similar at the majority of the sensors. The largest differences between case h and the rest of the cases are observed at the lower and the upper sensors, while at the middle sensors (e.g. M3N3) the results are almost the same for all cases. Case h predicts less diffusive results.

Therefore, the mesh of case i (mesh#2) can be considered as the grid independent one for the SST model.

Similar procedure was followed for the laminar model, too. Four different meshes were tested and the results are shown in Figure 2-16. Grid independency was not achieved for the laminar model.



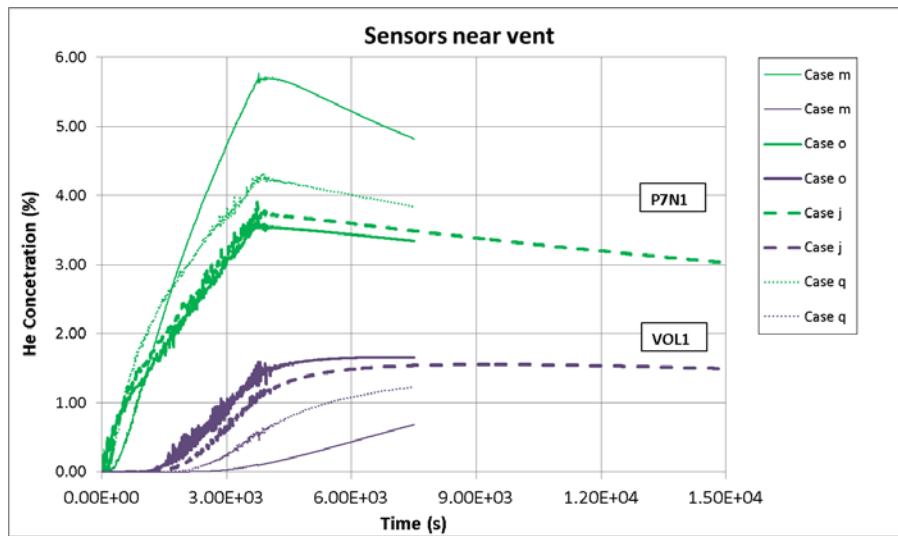
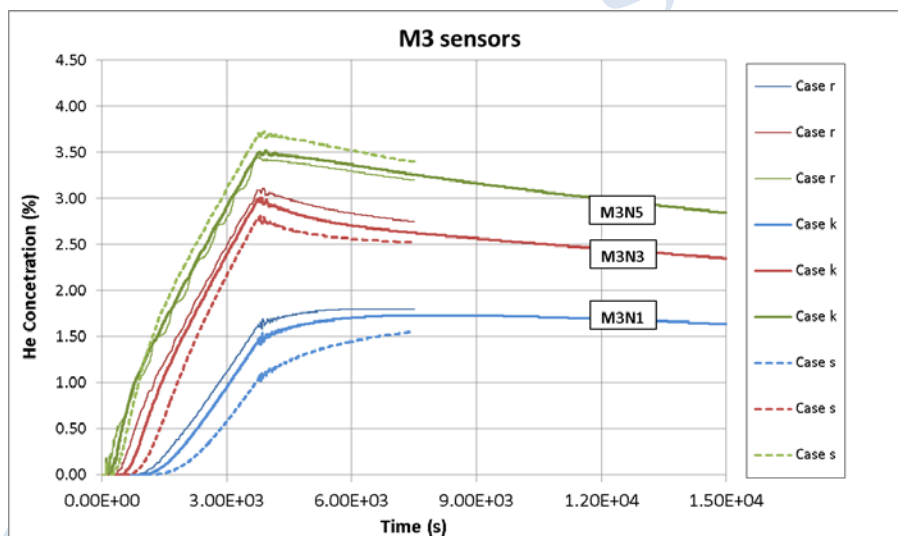


Figure 2-16. JRC-The results from the grid sensitivity study using the laminar model.

Figure 2-17 shows the results from the grid independency study using the DES model. Grid independency was not achieved for the DES model.



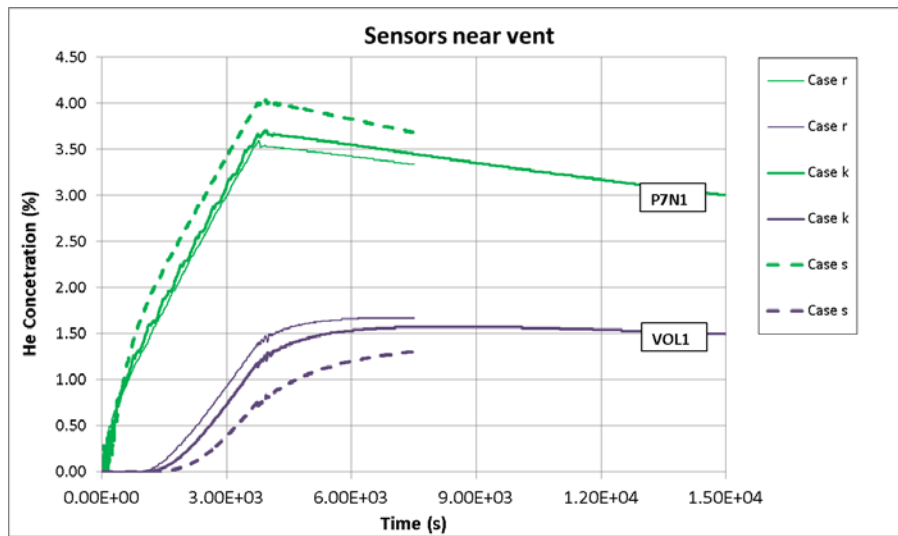
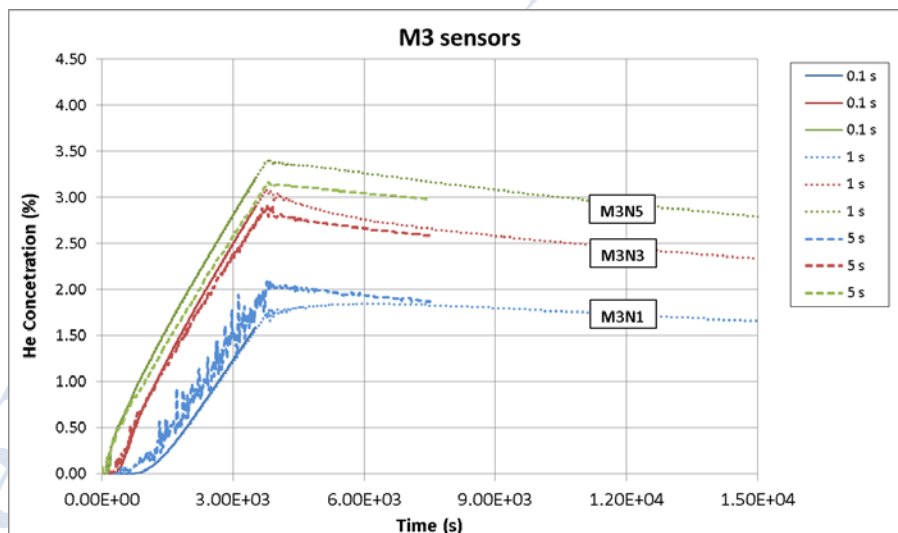


Figure 2-17. JRC-The results from the grid sensitivity study using the DES model.

The case with the independent grid and the SST model (case i) was employed for the time step sensitivity study. Three different time steps were tested: 0.1 s, 1 s and 5 s (case b, i and e, respectively in Table 2-3). The results are presented in Figure 2-18. The results with time step 0.1 and 1 s are identical at all sensors, while the largest time step equal to 5 s differs at all sensors. Therefore, a time step equal to 1 s is considered sufficient and independent.



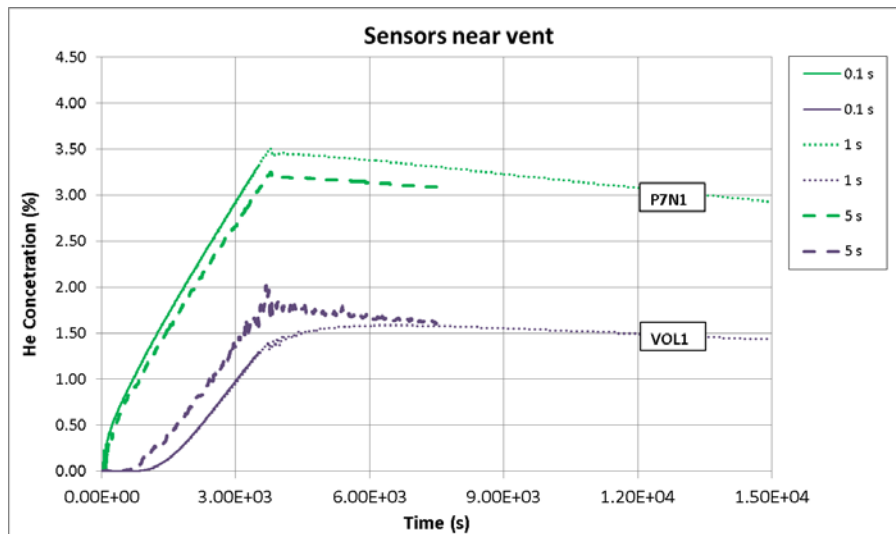
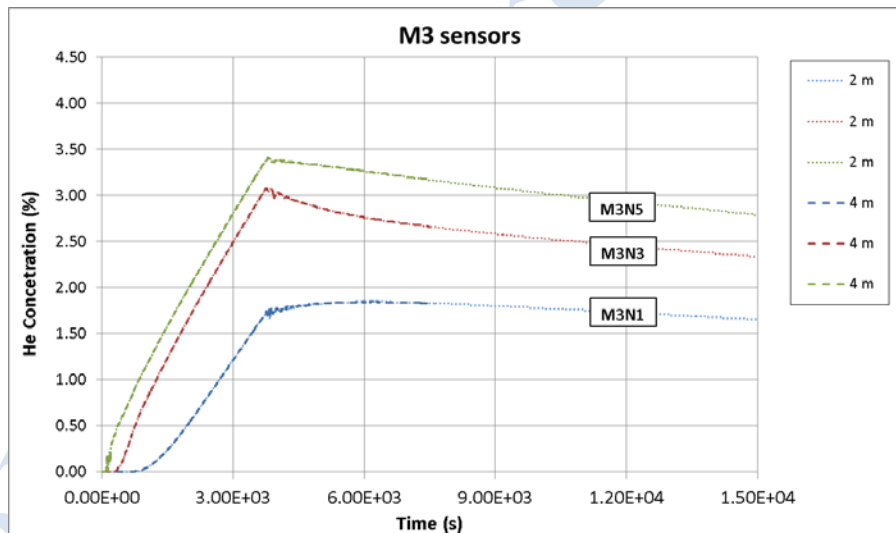


Figure 2-18. JRC-The results from the time step sensitivity study.

Finally, for the case i a more extended domain upwind the vent equal to 4 m expansion instead of 2 m expansion was used (case f in Table 2-3), to asses the domain effect on the results. Figure 2-19 shows the comparison between case i and case f. the results are identical at all sensors; therefore, a domain expansion equal to 2 m is sufficient.



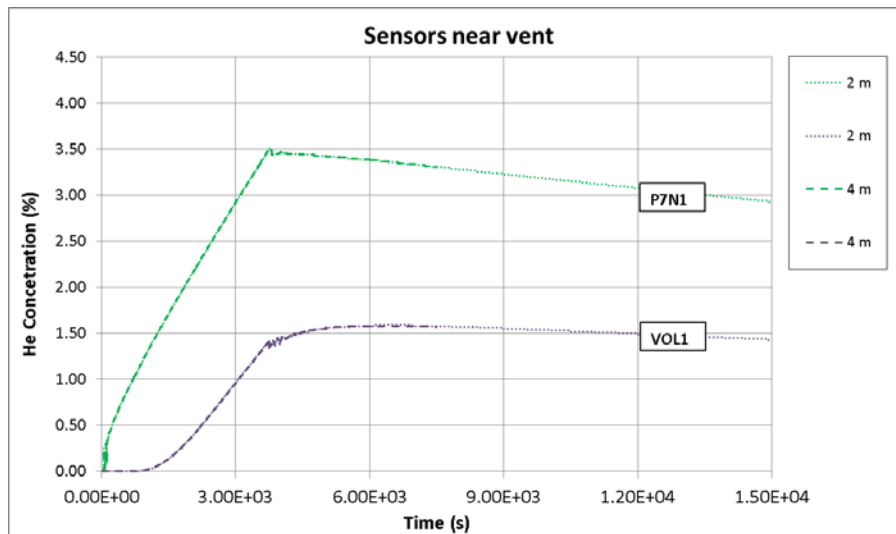


Figure 2-19. JRC-Domain expansion sensitivity study.

1.1.3.3 NCSR D

NCSR D performed several sensitivity studies: domain, grid and time step sensitivity study. Moreover, a simulation with 2nd order fully implicit scheme was examined for the k-ε turbulence model without any impact on the results; therefore the 1st order implicit scheme was used for k-ε and laminar turbulence model.

Initially, a domain sensitivity study was carried out for the k-ε turbulence model, using a coarse mesh (Grid 1 in Table 2-7). Four different domain expansions were applied: 0.25 m, 0.5 m, 1 m and 2m. The domain was extended only upwind the wall with the vent (in the negative x-direction, see Figure 2-1). Since the vent is placed approximately in the center of the wall and in the lower part of the wall no expansion is necessary in the y-and z-directions. The case without any domain expansion was also examined.

The results of the domain sensitivity study are presented in Figure 2-20. The predictions are almost identical for all expansion sizes at most of the sensors. Small differences among the case with 0.25 m expansion and the rest of the cases are detected at the sensor which is located in front of the hole. Therefore, a domain expansion equal to 1 m is proved to be sufficient. This domain expansion was used for the rest of the analysis for all turbulence models.

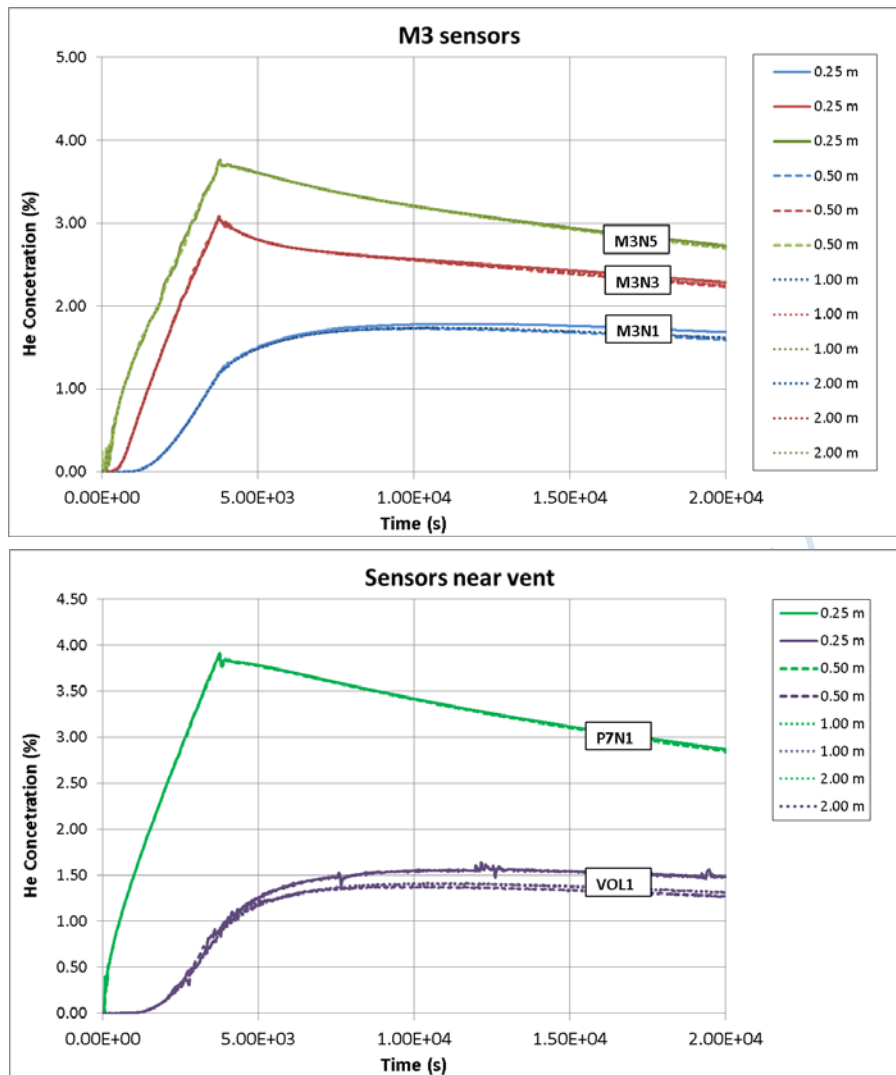


Figure 2-20. NCSR-D-The results from the domain sensitivity study with $k-\epsilon$ turbulence model.

In Figure 2-21 the results without domain expansion and with 1.0 m expansion (the independent one) are illustrated along with the measurements. It is shown that domain expansion upwind the vent, through which helium escapes is essential. Large differences are detected after the cease of the release (diffusion phase), where the predicted concentrations in the case without domain expansion are significantly under-predicted.

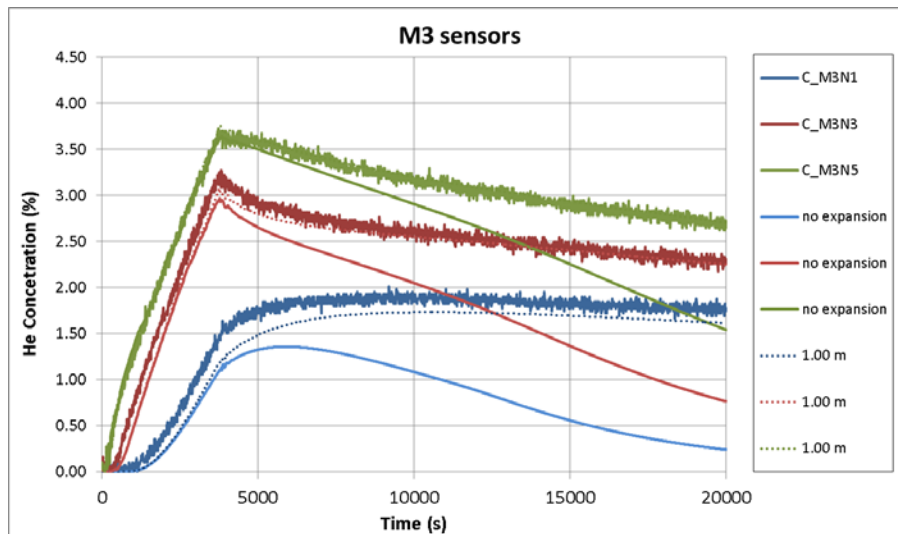


Figure 2-21. NCSR-D-The results without domain expansion with k-ε turbulence model.

Table 2-7 shows the main characteristics of the grids that were used in all the sensitivity studies. In all grids the maximum expansion ratio that was applied is 1.15 inside the GARAGE facility. Outside the GARAGE facility 1.125 expansion ratio is used in the x-direction. Between Grid 1 and Grid 2 the expansion ratios are different. In Grid 3 and Grid 4 more cells were used to discretize the source. In Grid 4 a smaller expansion ratio in the z-direction was applied compared to Grid 2 and Grid 3. In Grid 5 five cells were used along the source diameter (25 cells in total for the source area discretization). Finally, Grid 6 used seven cells along the source diameter, but higher expansion ratios inside the facility without however exceeding the maximum value of 1.15. Another significant difference among Grid 6 and the rest grids is that in Grid 6 the flow inside the injection pipe was also modeled. The source was placed 5 cm before the pipe exit. Five equidistant cells (0.01 m) were used along the pipe.

In the case with k-ε turbulence model four different grid sizes were tested: Grid 1, 2, 3 and 4.

Table 2-7. NCSR-D-The main characteristics of the grids that were tested.

Name	Number of cells in (x,y,z)	Total number of cells	Minimum cell size (dx,dy,dz) - m	Cells along source diameter	Flow modeling inside pipe
Grid 1	(95,51,33)	159,885	(0.0298,0.0298,0.055)	1	No
Grid 2	(115,63,49)	355,005	(0.0298,0.0298,0.0275)	1	No
Grid 3	(145,74,49)	525,770	(0.0149,0.0149,0.0275)	2	No
Grid 4	(166,89,55)	812,570	(0.0099, 0.0099,0.0275)	3	No
Grid 5	(108,75,74)	599,400	(0.00597, 0.00597,0.01)	5	No
Grid 6	(95,65,62)	382,850	(0.0043, 0.0043,0.01)	7	Yes

In Figure 2-22 the results from the grid sensitivity study are presented. It is shown that the results are similar using all four grid sizes. Small discrepancies (less than 10%) are

found at the sensor in front of the vent among the coarse grid (Grid 1) and the three finer grids. Grid 2 can be considered that provides grid independent results.

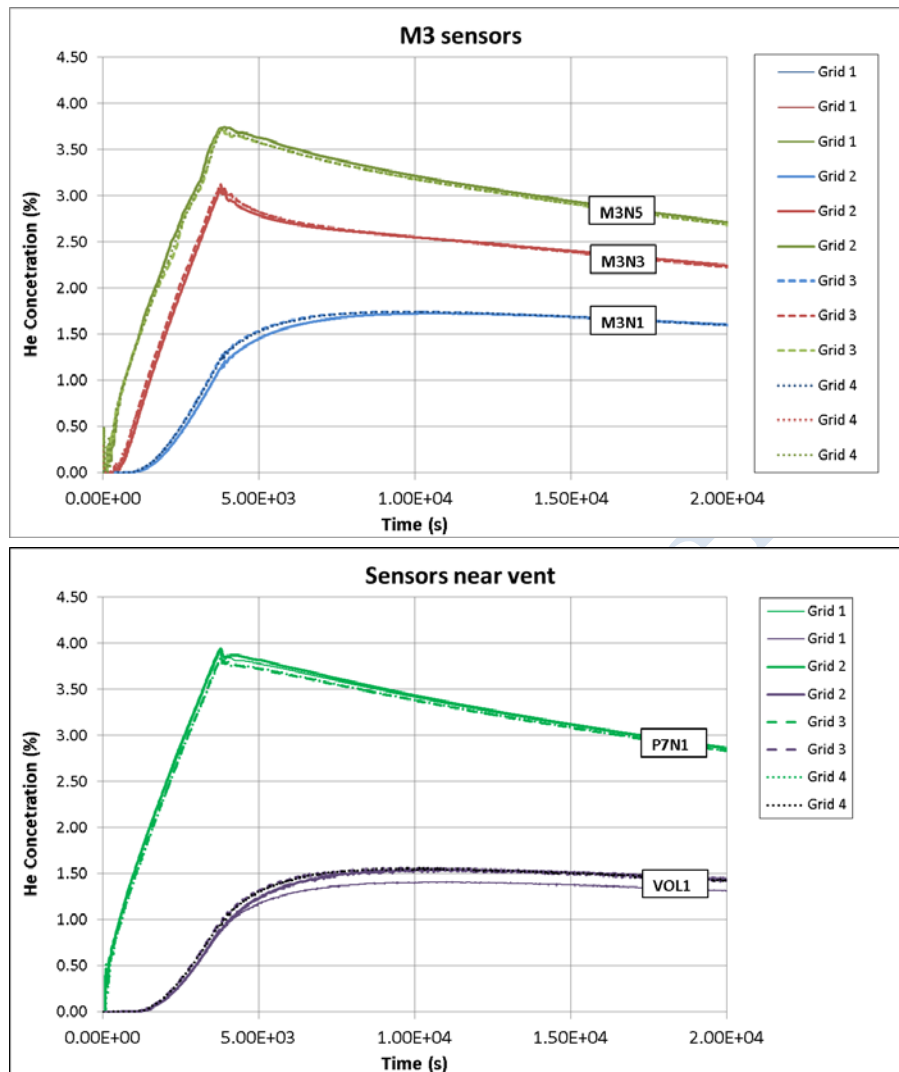


Figure 2-22. NCSR-D-The results from the grid independency study with k-ε turbulence model.

The grid independent grid was used to carry out a time step sensitivity study. To perform the time step sensitivity study three different maximum values of CFL number were imposed, CFL=5, CFL=10 and CFL=20. These values correspond to a time step of 0.3, 0.62, 1.25 s, respectively during the release and to about 1.26, 2.5, 5 s, respectively, after the release has stopped. Figure 2-23 shows the results from the time step sensitivity study at three sensors near the injection point. The same behavior is observed at all sensors. It can be noticed that the results are identical. However, convergence issues were observed during the diffusion phase when CFL=20 was used. Therefore, CFL=10 is considered more appropriate.

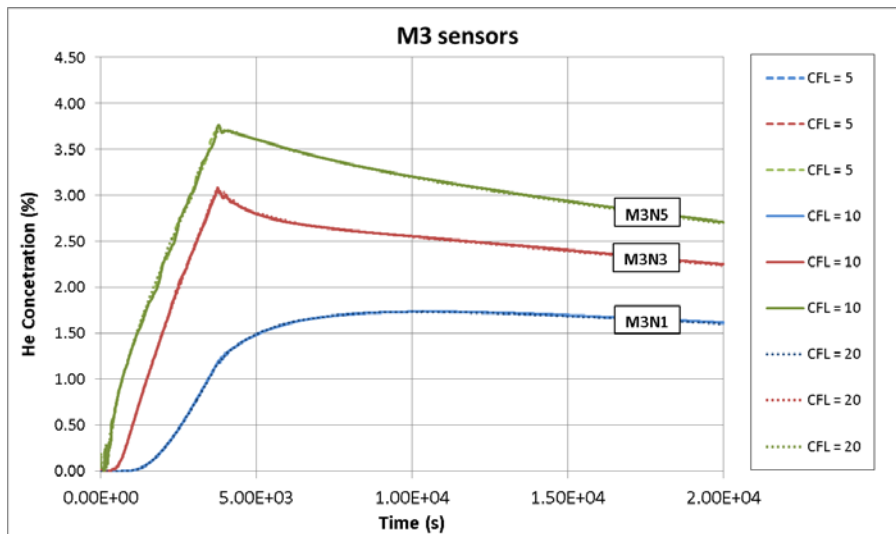
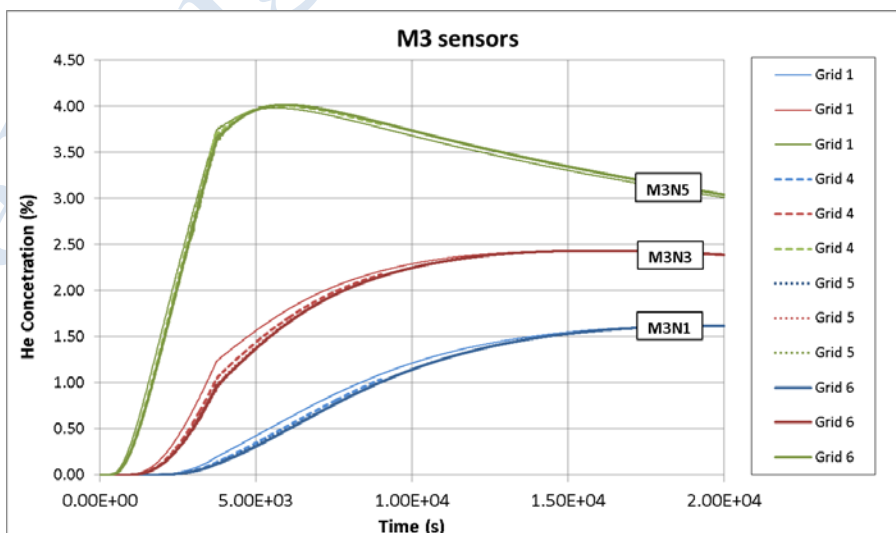


Figure 2-23. NCSR-D-The results from the time step sensitivity study with k-ε turbulence model.

Figure 2-24 shows the results with the different grids that were used for the laminar model. The parameters of the grids tested are indicated in Table 2-7. It can be observed that all grids provide similar results with insignificant differences. However, due to the fact that the results were not in good agreement with the experiment a very fine grid along the vertical direction, where high gradients are expected was also tested. More specifically, 88 equidistant cells were used in z-direction, while all other grid characteristics were the same as Grid 2. The results are not shown here for space economy; however, they showed no differences compared to the results obtained with the other grids. Therefore, the coarser grid, Grid 1, is considered the independent grid for laminar model.

Moreover, according to Figure 2-24 it is shown that the case, which solves the flow inside the pipe (Grid 6), gives the same results as the cases where the source is placed exactly at the pipe exit.



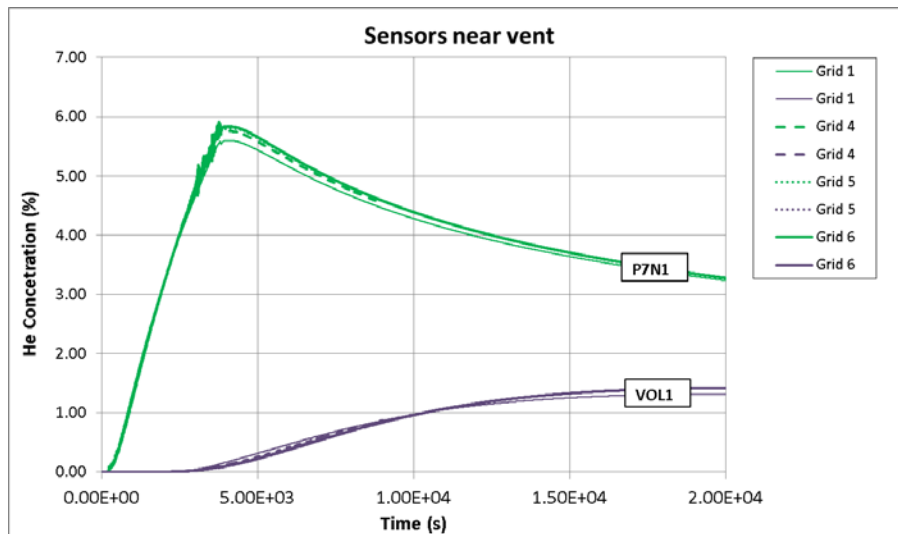
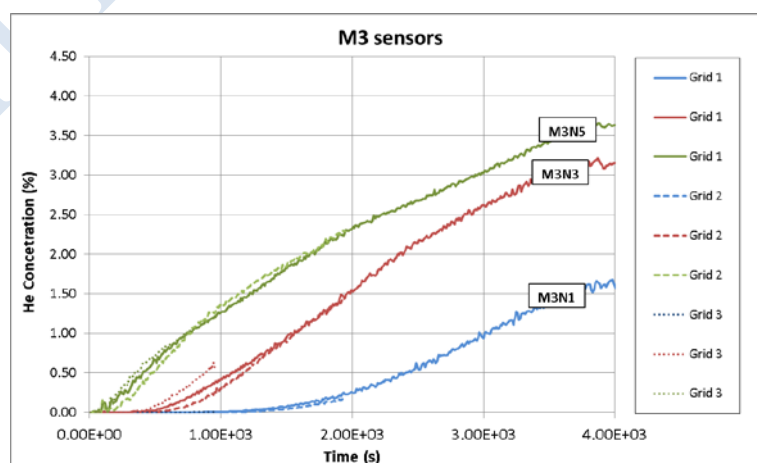


Figure 2-24. NCSR-D-The results obtained with different grid sizes and the laminar model.

According to (Molkov & Shentsov 2014) the laminar model is very sensitive to the value of CFL number, and small time steps are required. Therefore, smaller CFL numbers were tested in the laminar model, too. However, even with CFL=2 the results were not changed. So, a CFL number equal to 10 seems to be sufficient for the laminar model, too.

Figure 2-25 shows the results of the grid independency study for the case with RNG-LES model. Three different grids were examined: Grid 1, Grid 2 and Grid 3 (Table 2-7). In all simulations the CFL=0.9 restriction was imposed. It is shown that there are small differences among the results during the release phase. The simulations with the finer grids have not reached the diffusion phase (due to high computational cost). However, it is considered that there would be no large discrepancies among the results during the diffusion phase too. The coarse grid (Grid 1) gives results between the two finer grids, and thus it can be considered as the independent one and it is used for the rest of the analysis. Of course, to be certain about the grid independency the simulations with the finer grids should be completed.



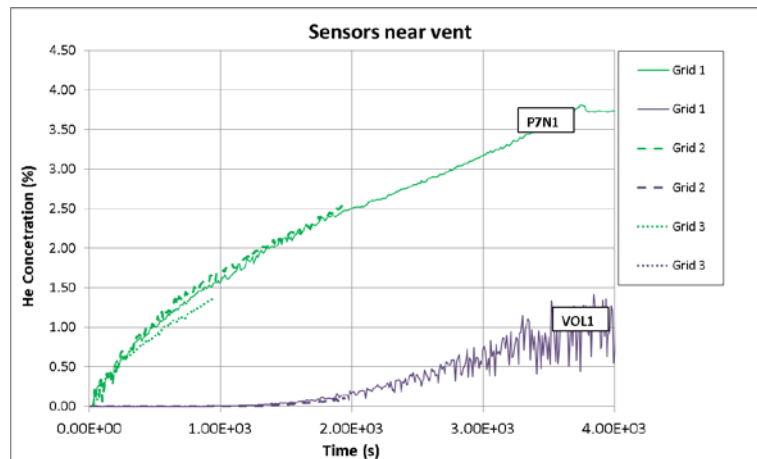


Figure 2-25. NCSR- The results obtained with different grid sizes and the RNG-LES model.

Finally, the time step sensitivity study for the RNG-LES is shown in Figure 2-26. Two smaller CFL restrictions were applied, CFL=0.1 and CFL=0.3 and the results are almost identical with the ones obtained using CFL=0.9.

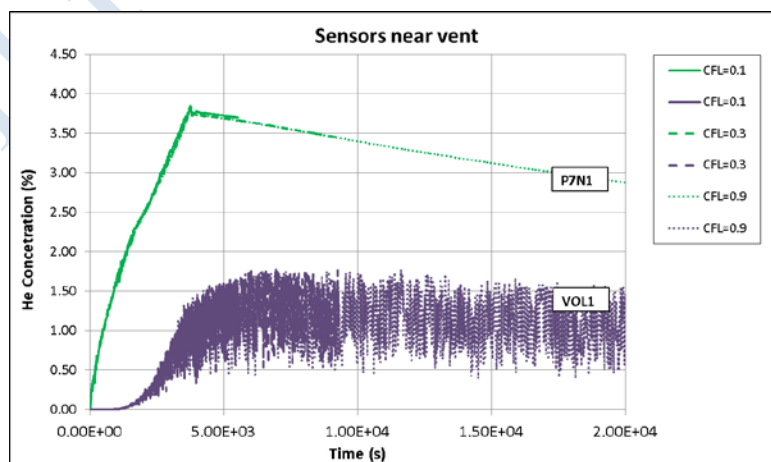
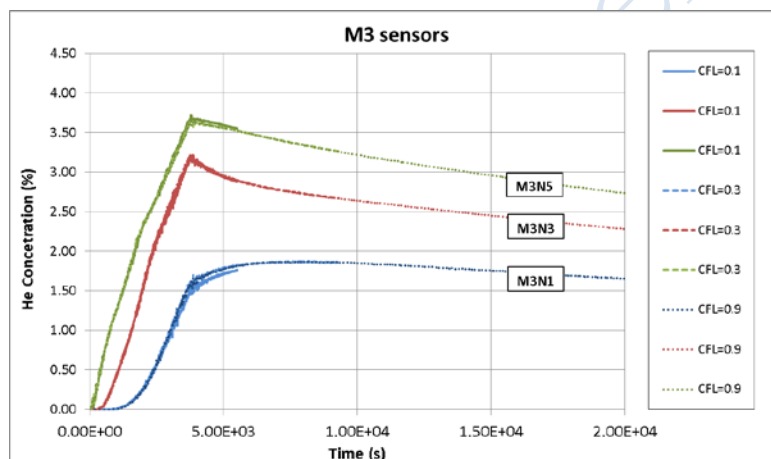


Figure 2-26. NCSR- The results from the time step sensitivity study for the RNG-LES model

1.1.3.4 UU

UU performed a grid sensitivity study and a time step sensitivity study using the LES Dynamic S-L model. The grid independence study was done using three block-structured hexahedral computational grids as shown in Figure 2-27. Calculation domains include both the enclosure part of size as described in experiment and 2.5 m extension at the vent side to avoid boundary conditions being imposed directly at a vent see Figure 2-28. Full 3D grid with no symmetry assumed. All three grids have the same inlet resolution in a form of is a polygon inscribed in a circle of 9 cells across the diameter and with cross-section area of 45 cells and same polygonal vent resolution with 10 cells across the height and 11 across the width with total area of 74 cells as seen in Figure 2-28. The inflow boundary is located inside the release pipe at distance 5 cm from the pipe exit. There are 5 cells along the pipe axis from the inflow boundary to the pipe exit.

For all grids the expansion ratio was 1.1 in all directions from the release pipe vertically and horizontally until the cell size increased and then became uniform. The number of nodes in each direction from the pipe determined the total number of control volumes in a garage. The total number of CVs in the garage of Grid 1 is 254,089, and in the whole domain there are 287,941 CVs. The total number of CVs in the garage of Grid 2 is 523,540, and in the whole domain there are 557,392 CVs. The total number of CVs in the garage of Grid 3 is 996,639, and in the whole domain there are 1,030,491 CVs. Table 2-4 shows some details about the simulations that were performed.

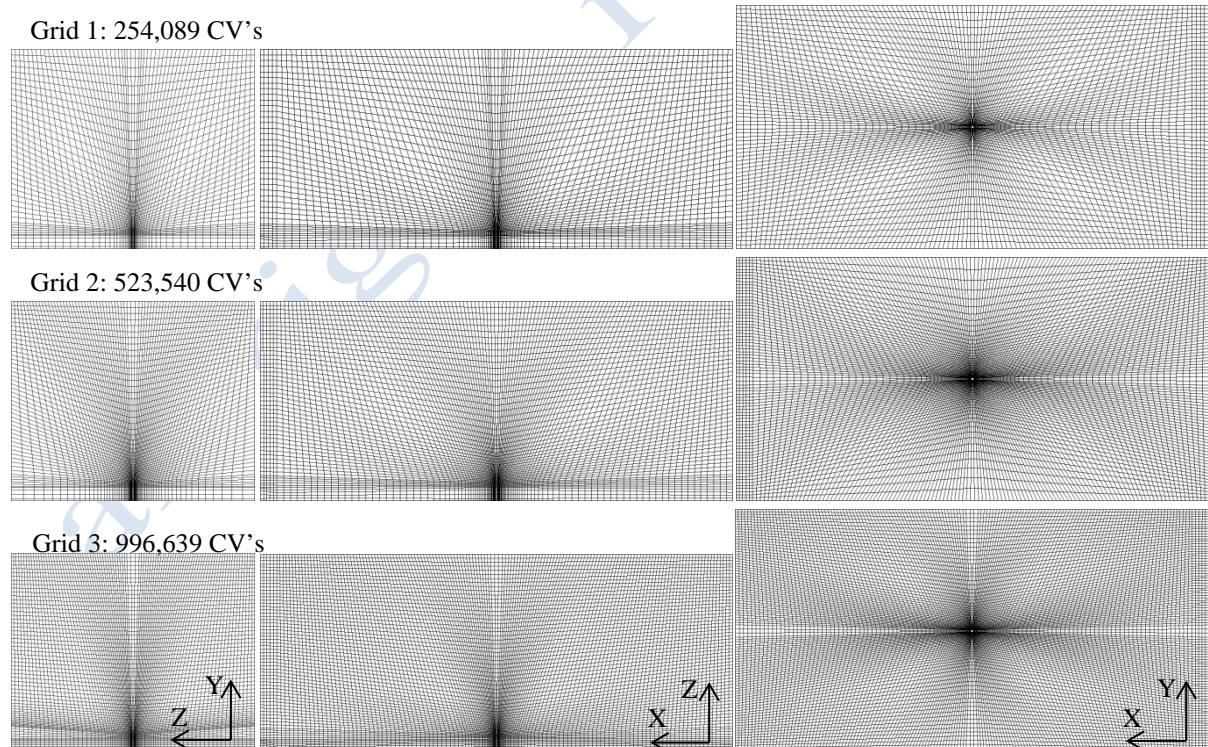


Figure 2-27. UU-Garage centreline cross sections from top to bottom Grid 1 (254,089 CV's), Grid 2 (523,540 CV's), Grid 3 (996,639 CV's): x=0 (left), y=0 (middle), z=0 (right).

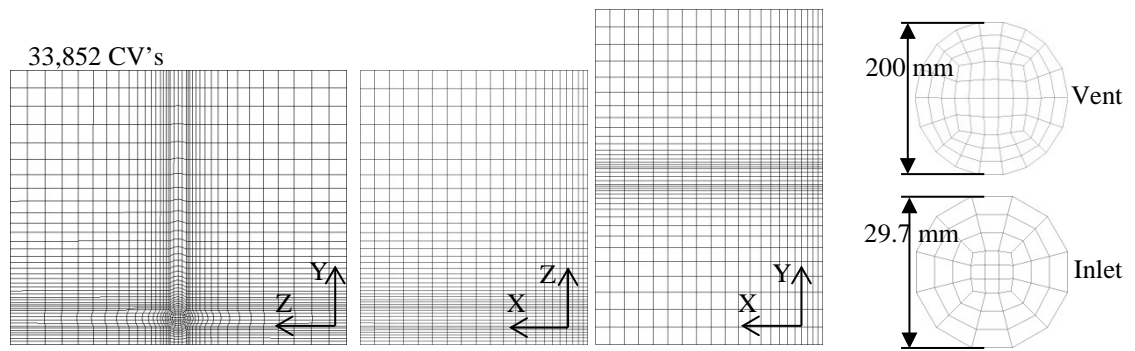


Figure 2-28. UU-Extended domain cross sections from left to right: $x=0, y=0, z=0$, vent and inlet cross sections.

As Figure 2-29 indicates the results with the different grid sizes are similar. Although Grid 2 is the independent one, Grid 1 is used for the rest sensitive studies analysis due to the lower computational time and considering the fact that the results have not significant differences.

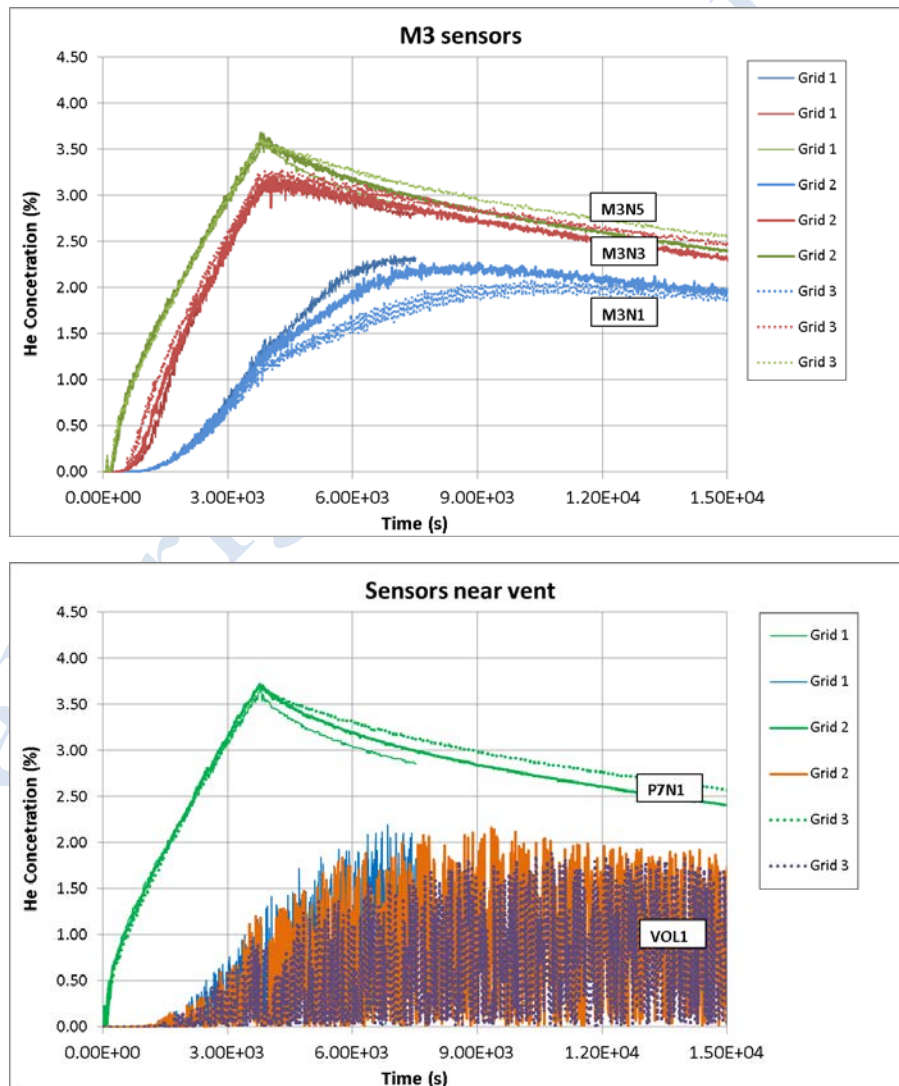


Figure 2-29. UU-The results from the grid independency study.

Two different time steps were examined using Grid 1: 0.2 s and 0.02 s. The results are shown in Figure 2-30. It is observed that there are differences between the results with 0.2 and 0.02 s time step, especially during the release phase. The predictions with the larger time step gives higher concentration levels near the ceiling and lower concentration levels at the bottom sensors compared to the case with the smaller time step (higher stratification). As it will be shown in Section “Results and discussion” the prediction with the smaller time step is closer to the experiment. Therefore, the simulation with the time step equal to 0.02 s will be compared with the experiment and a time step equal to 0.02 s is considered sufficient and it will be used for the RNG-LES simulation, too.

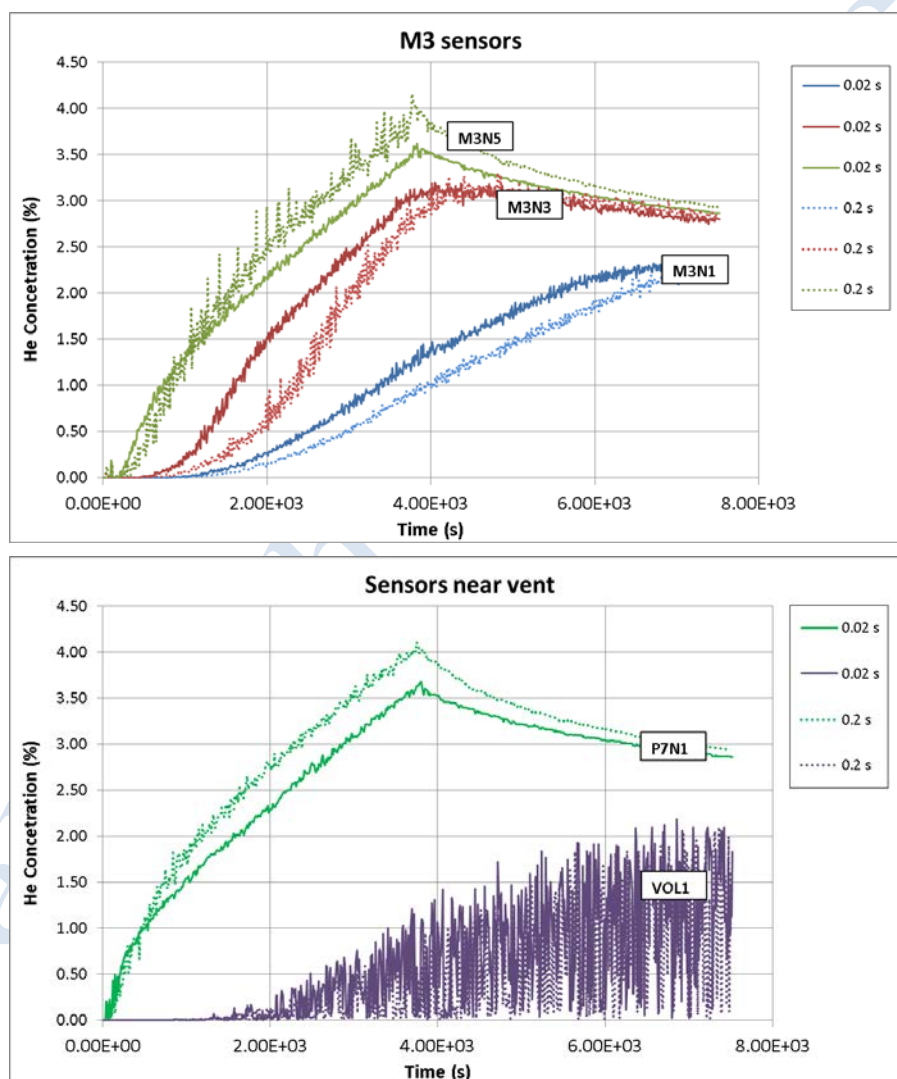


Figure 2-30. UU-The results from the time step sensitivity study.

1.1.3.5 EE

EE performed a sensitivity study focusing on grid size. The grids for this study were shown previously. In all cases, the CFL number remained unchanged. In LES modelling, this means that smaller cells are able to represent smaller turbulent eddies. If the smaller eddies are still larger than the filter size used in the LES approach, then the more detailed grids do not only represent a more refined version of the results, but actually a distinct version, incorporating better representation of the turbulence spectrum. Caution is therefore required with interpretation of grid sensitivity studies using LES models (as opposed to steady-state two equation turbulence models).

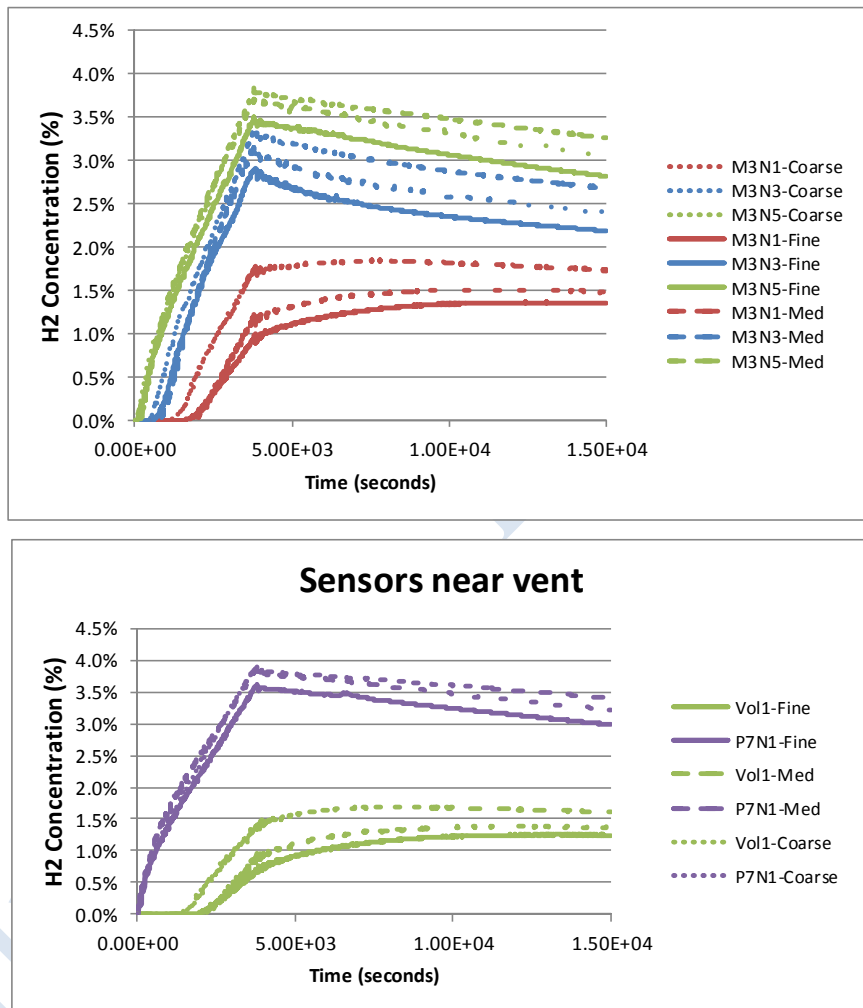


Figure 2-31. EE- Results from the grid sensitivity study using LES turbulence model.

The figure above shows the results from the grid sensitivity study for EE, using three progressively refined grids. There is a good degree of similarity in all results, indicating that the fundamental physics are well captured in all cases. However it is observed that as the grid is progressively refined, there is a reduction in the He concentration levels observed at the M3, Vol1 and P7N1 sensor positions. The reduction in predicted He concentration is most marked for sensors at lower elevations. From flow-field observations it is suggested that this is due to the greater level of diffusion inherent in the coarser grid simulations i.e. while the finer grids

resolve turbulence at a finer level, such small scale eddies are not as efficient at transporting He over concentration gradients as the larger eddies. The result is a more concentrated He jet in the finer simulations, resulting in lower diffusion of He at low levels. Nevertheless, it can be observed that at each progressive doubling of grid resolution, the change in result is reducing i.e. the flow field is asymptoting to a solution. The differences between the two finest meshes are relatively small. For these purposes the finest grid is demonstrated to be relatively insensitive to grid resolution.

1.1.4 Results and discussion

This Section is subdivided in four subsections. In the first three subsections the results from each partner are presented and discussed. The results using different turbulence models are compared with the experimental results. In the last subsection a comparison among the results of all partners is presented. Comparison is performed among results with the same turbulence model but with different modeling approach (presented in Section 2.1.2).

It should be noted that the results that are presented in this Section are the independent (grid, domain, etc.) results according to each partner's sensitivity studies.

1.1.4.1 Results from AREVA

Figure 2-32 shows the mass balance and the mass error during the simulation. The definitions are given by,

$$\text{mass_bal}(t) = m_{\text{HE_accum}} - (m_{\text{HE_released_tot}} - m_{\text{HE_outflow_tot}}) \quad (1.1)$$

$$\text{mass_error}(t) = \frac{m_{\text{HE_accum}} - (m_{\text{HE_released_tot}} - m_{\text{HE_outflow_tot}})}{m_{\text{HE_released_tot}}} \quad (1.2)$$

where $m_{\text{HE_accum}}$ is the helium mass inside the whole domain at time t , $m_{\text{HE_released_tot}}$ is the total helium released mass from $t=0$ to t and $m_{\text{HE_outflow_tot}}$ the total helium mass that flew out the domain from $t=0$ to t .

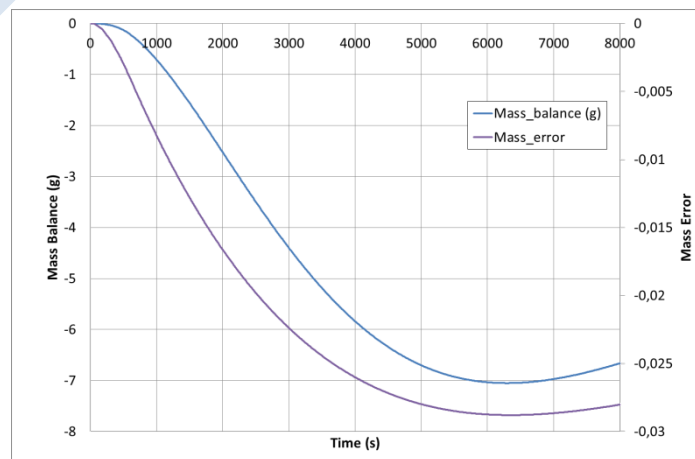


Figure 2-32. AREVA-The mass balance and the mass error during the low Reynolds $k-\omega$ simulation

Some examples of concentration profiles registered in some sensors are represented in Figure 2-33.

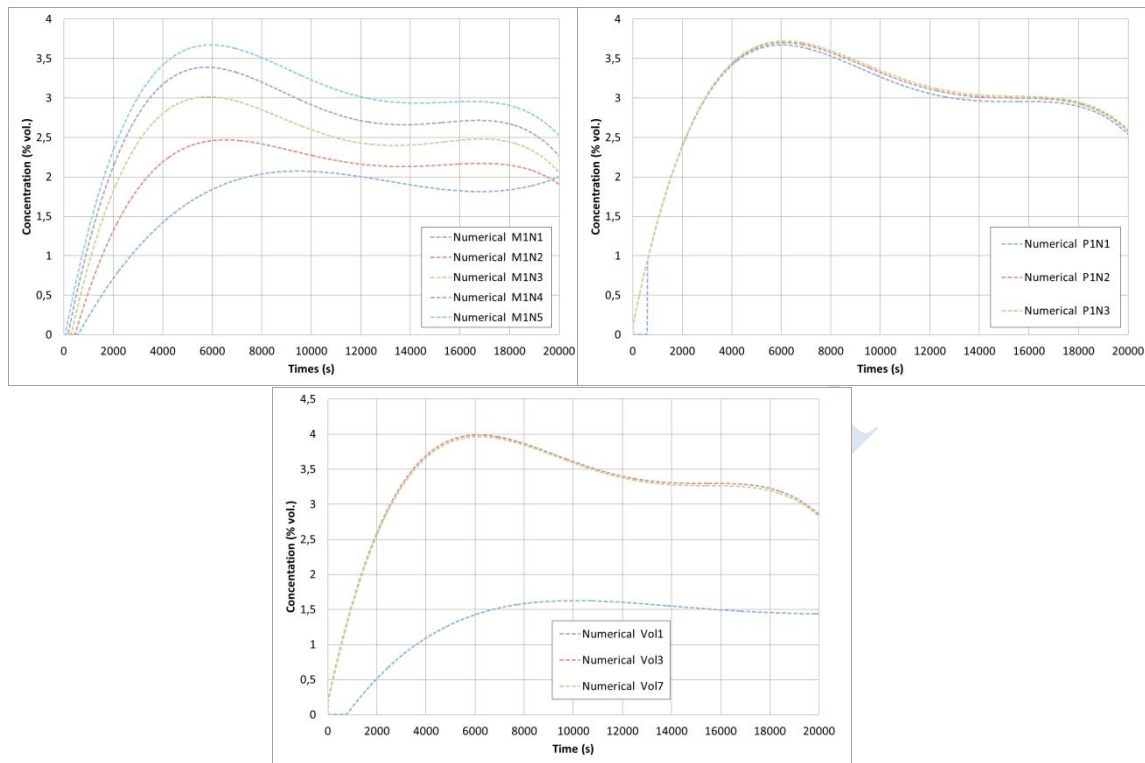
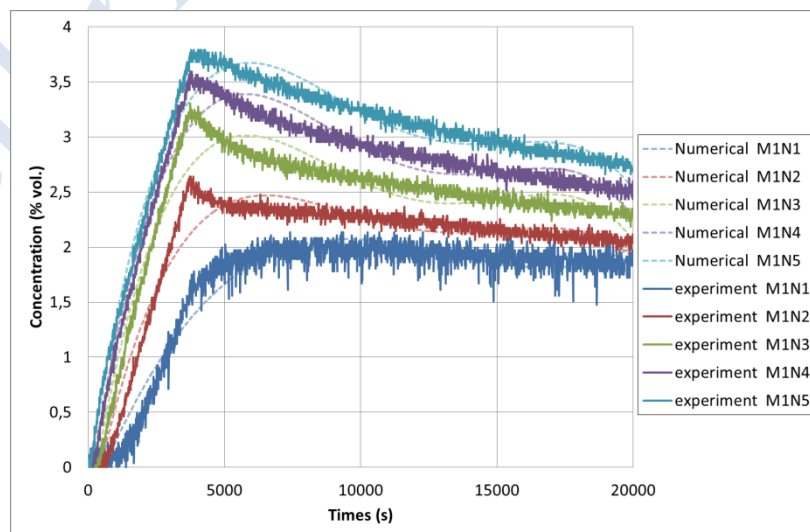


Figure 2-33. AREVA-Computational results of helium concentration at several sensors.

The different examples presented confirm the stratified regime. The comparison between these results and those obtained experimentally is presented in Figure 2-34.



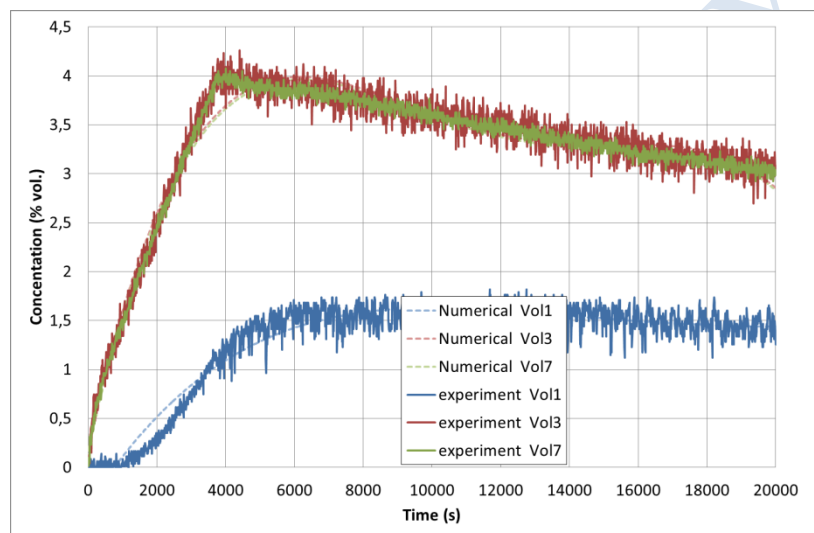
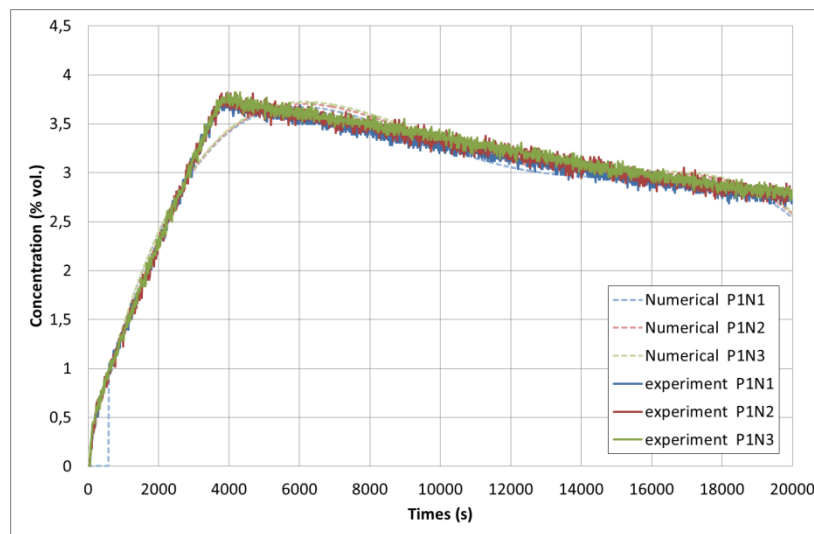


Figure 2-34. AREVA- Comparison of the results using the low Reynolds $k-\omega$ turbulence model with the experimental results.

The comparisons between the experimental and the numerical results for the examples presented, suggest that the numerical simulation realized is a good approximation of the full size experiment. Even if the numerical peak concentration happen with a time delay, without further explanations. However, it could be judicious to do this comparison exercise for all the sensors before testifying of the high quality of the numerical simulation realized.

Figure 2-35 the evolution of the volume fraction within the chamber on plane of symmetry x-z, and at several times of the study. At $t = 3740s$, the helium rejection is stopped and several sub-layers stand out. This regime arises when buoyancy dominates the dispersion. Then, at $t=10000s$, the sub-layers are present but the concentration levels are not stabilized. Finally, at $t=20000s$, which is the final time of the numerical simulation, the concentration levels varied again reducing the sub-layers created during the ejection.

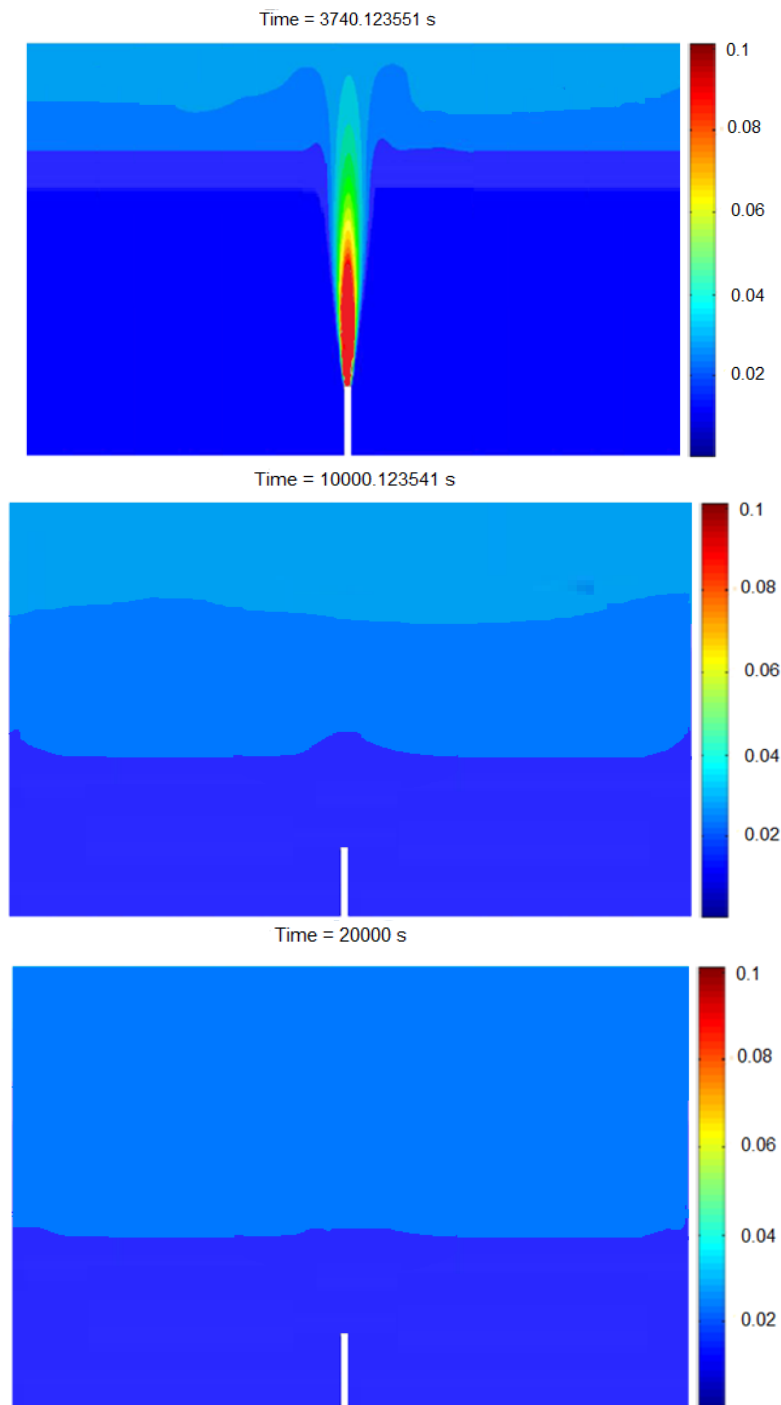


Figure 2-35. AREVA-Helium concentration contours on y-injection plane with the low Re k- ω model at 3740 s (top), 10000 s (center) and 20000 s (bottom).

Figure 2-36 shows the predicted flammable mass (mass corresponding to 4-75% v/v) inside the facility versus time. The prediction provides maximum flammable mass equal to about 55 g). After 6130 s (2390 s after the cease of the release) the flammable mass starts to decrease. Later than 10000 s the flammable mass inside the facility is almost zero.

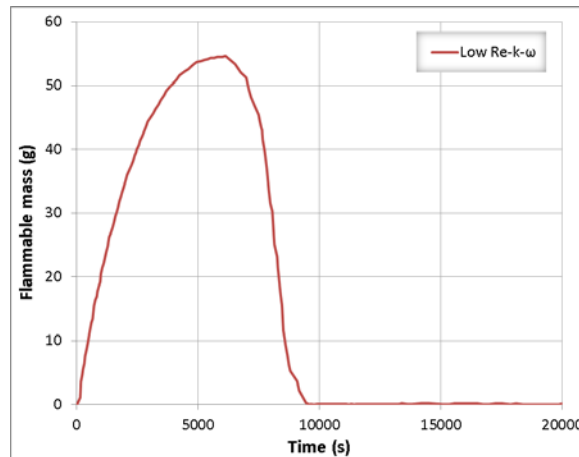


Figure 2-36. AREVA-Predicted flammable mass inside the GARAGE facility

1.1.4.2 Results from JRC

JRC performed simulations with laminar model, the SST transitional model and DES model. However, since there was not achieved grid independency with laminar and DES model, only the SST predictions are shown here. Figure 2-37 shows the mass balance and the mass error during the simulation.

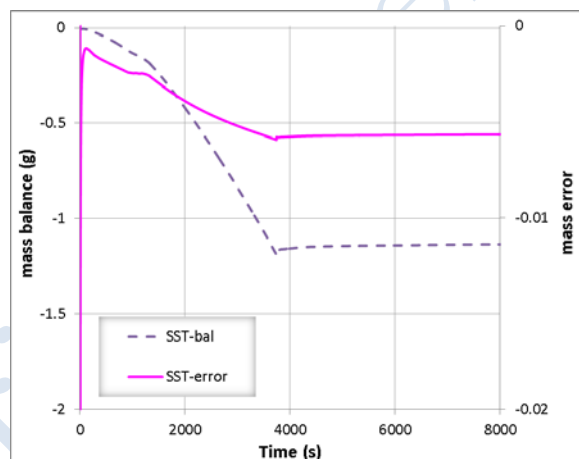


Figure 2-37. JRC-The mass balance and the mass error during the SST simulation.

Figure 2-38 shows the time series of the predicted concentrations using the SST turbulence model and the measured concentrations at several sensors. SST model performs very well. The predicted concentrations are in very good agreement with the measurements. However, they are slightly under-predicted in the diffusion phase (after the cease of the release).

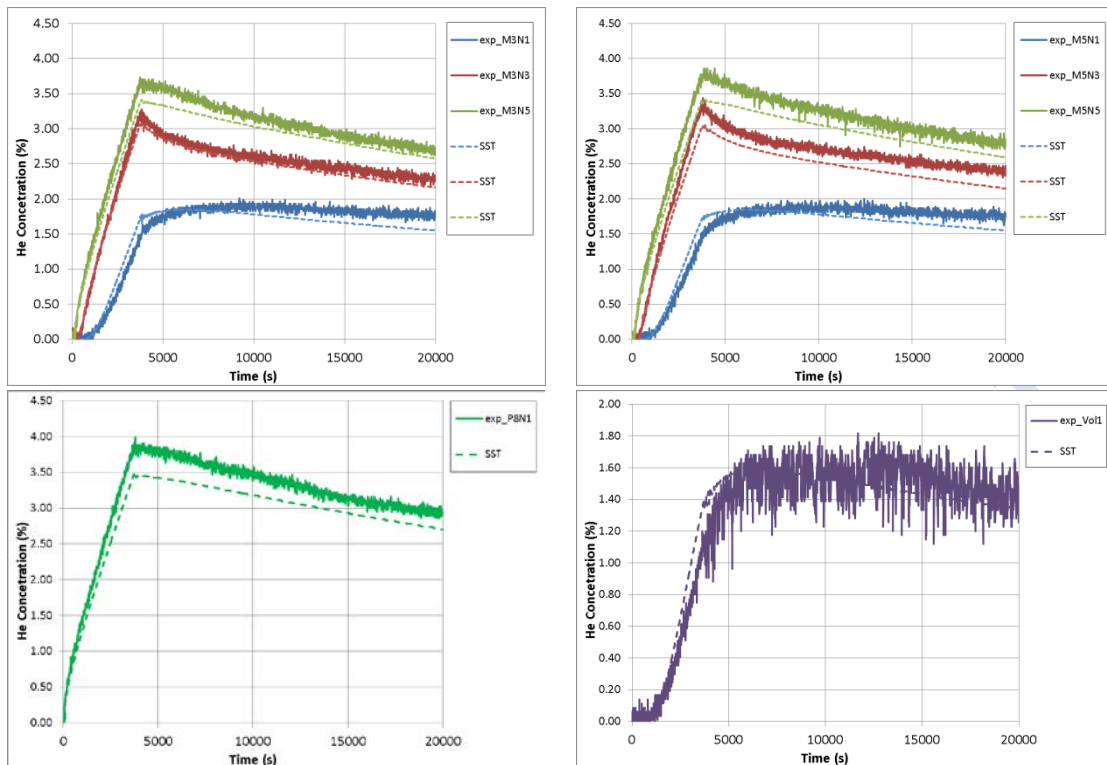


Figure 2-38. JRC-Comparison of the results using the SST turbulence model and the experimental results.

Figure 2-39 show the predicted concentration contours using the SST turbulence model on the y-injection plane at 3740 s (end of the release), 10000 s and 20000 s.

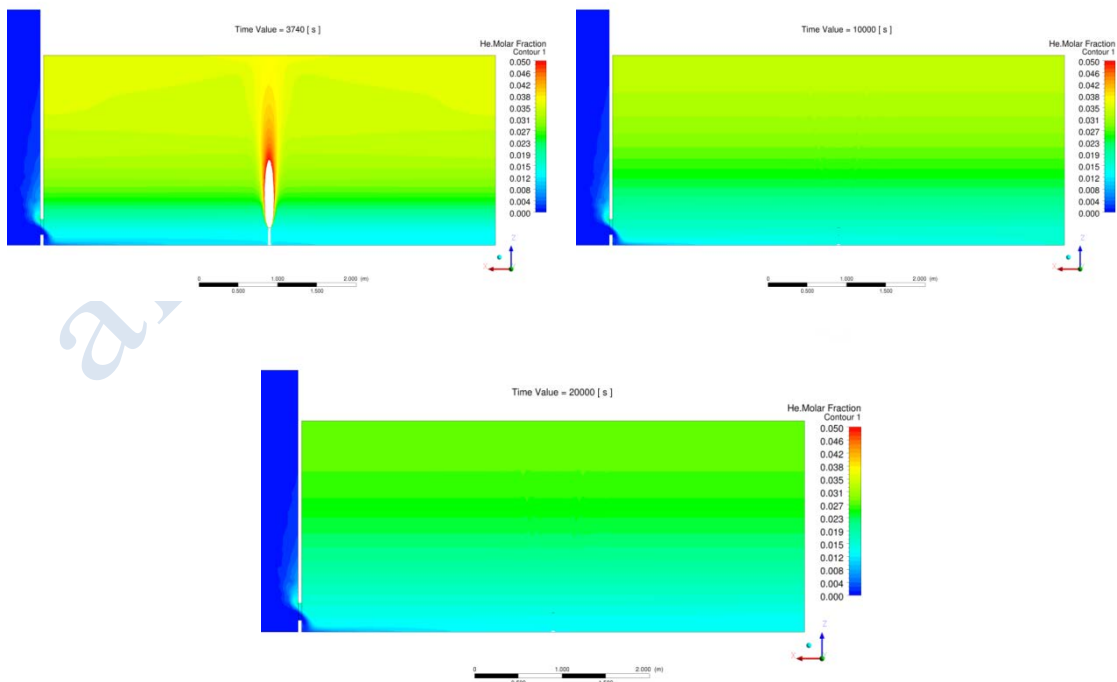


Figure 2-39. JRC-Helium concentration contours on y-injection plane with the SST model at 3740 s (left, top), 10000 s (right, top) and 20000 s (bottom).

Figure 2-40 shows the predicted flammable mass inside the facility versus time. The prediction provides flammable mass equal to about 0.24 g. The SST model predicts an abruptly decrease of the flammable mass as soon as the release is stopped. This is explained by the fact that concentrations values higher than 4% are mainly observed at the core section of the jet. Later than 4000 s the flammable mass inside the facility is zero.

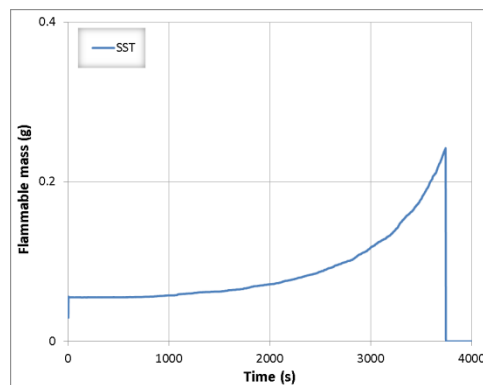


Figure 2-40. JRC-Predicted flammable mass inside the GARAGE facility.

1.1.4.3 Results from NCSR D

NCSR D performed simulations with laminar model and with k-ε and RNG-LES turbulence model. Figure 2-41 shows the mass balance and the mass error during the simulations with each model. The mass error is very small during both the release and the diffusion error.

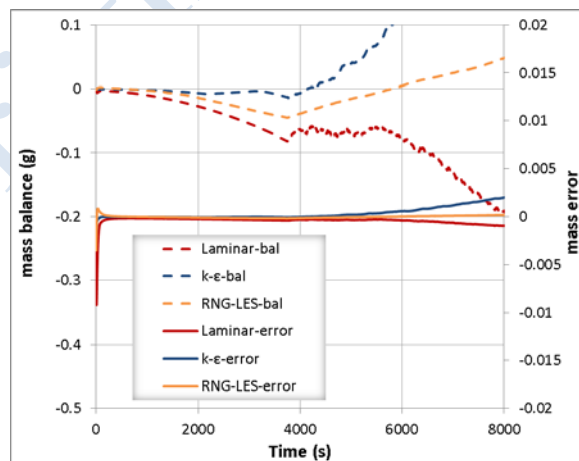


Figure 2-41. NCSR D-The mass balance and the mass error during the simulations.

Figure 2-42 shows the time series of the predicted concentrations and the measured concentrations at several sensors. The laminar model tends to under-predict the concentrations at the lower sensors and overpredict them at the upper sensors. The underprediction at the lower sensors the underprediction is more significant during the

release. At the lower sensors there is also an overestimation of the arrival time. In general, the results show that the laminar model predicts a more stratified mixture especially at the initial stage of the release compared to the experiment. This means that more diffusion is required in the model to match the experiment.

The k-ε model is in very good agreement with the experiment at all sensors, and especially at the upper sensors near the ceiling. However, it tends to slightly under-predict the concentrations at the lower sensors (at 315 mm). The turbulent diffusion that k-ε model predicts assists the mixing and provides stratification similar to the experimental one.

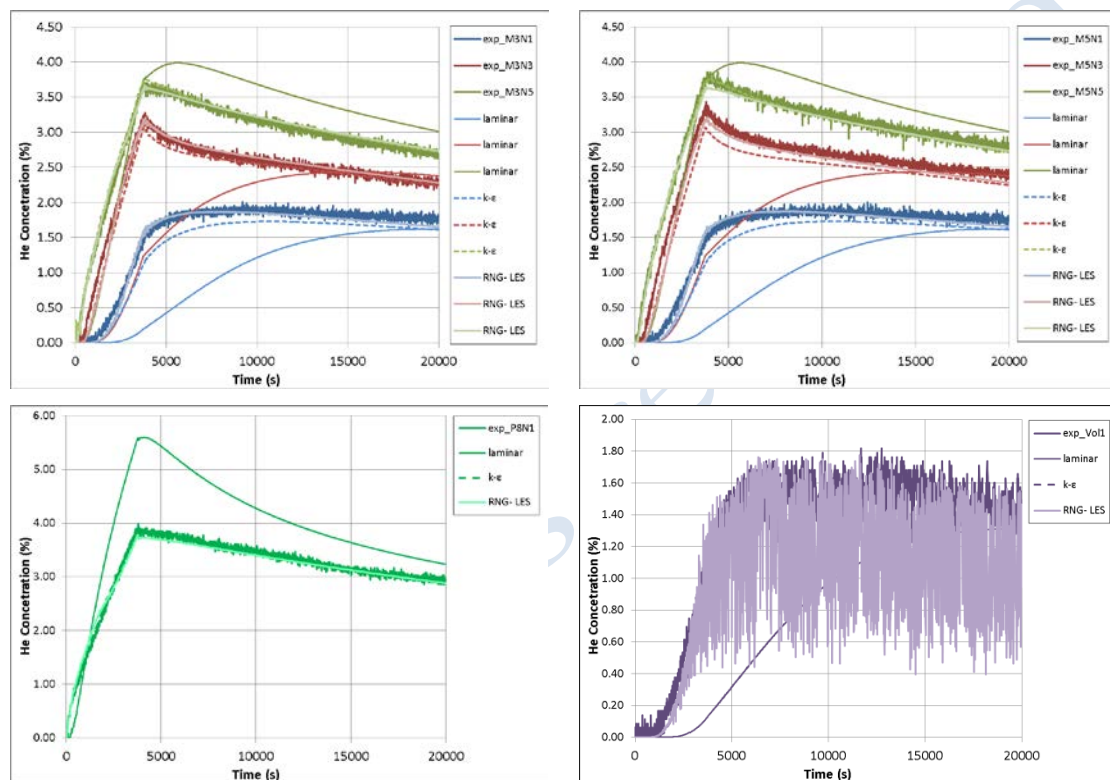


Figure 2-42. NCSR-D-Comparison of the results using the laminar model, the k-ε model and the RNG-LES turbulence model with the experiment.

The RNG-LES model gives results in very good agreement with the experiment during both the release and the diffusion phase. The predictions are almost identical with the measurements at most sensors.

Figure 2-43-Figure 2-45 show the concentration contours at three different times (during the release, at the end of the release and after the end of the release) as were predicted with the three models. According to these figures k-ε and RNG-LES model predict less stratified mixture and more diluted mixture inside the facility at all times compared to the laminar model. As a result higher concentration levels near the ceiling are met at 3740 s using the laminar. During the diffusion phase both k-ε and RNG-LES model give a more homogenous mixture, especially at 20000 s, while laminar model predicts a more stratified mixture even at 20000 s. In general, k-ε and

RNG-LES behavior are very similar at all times; however, in RNG-LES the turbulent eddies are apparent in the jet core in the release phase (at 3740 s).

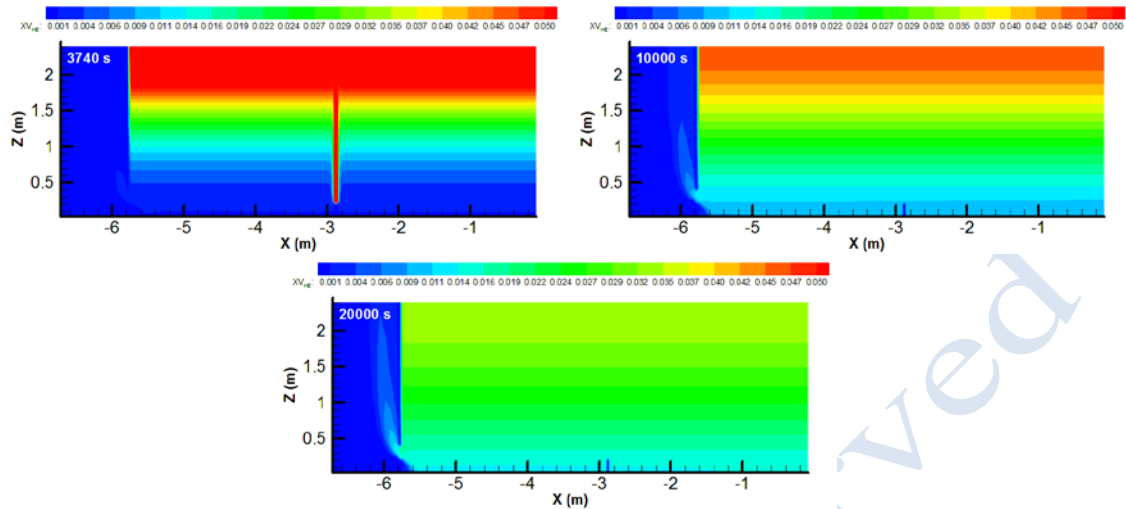


Figure 2-43. NCSR-D-Helium concentration contours on y-injection plane with the laminar model at 3740 s (left, top), 10000 s (right, top) and 20000 s (bottom).

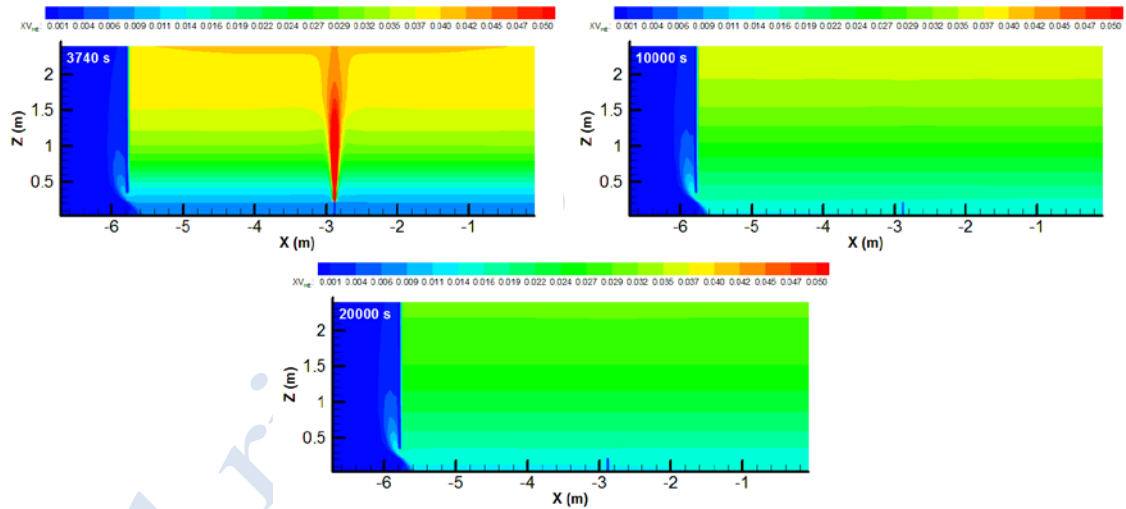
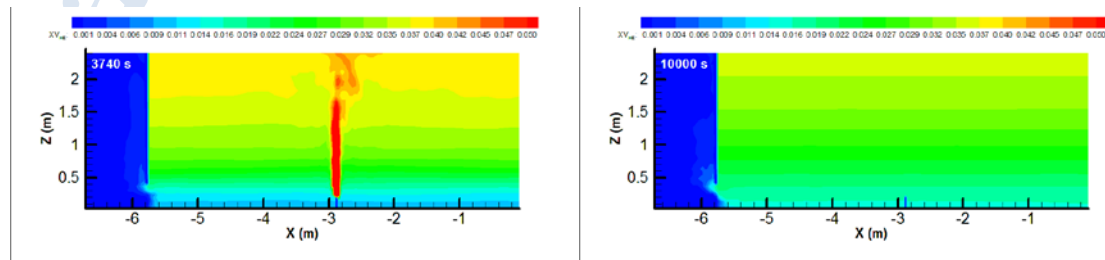


Figure 2-44. NCSR-D-Helium concentration contours on y-injection plane with the k-ε at 3740 s (left, top), 10000 s (right, top) and 20000 s (bottom).



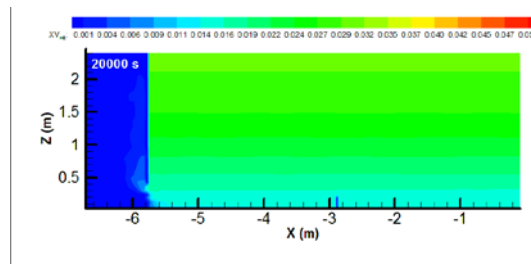


Figure 2-45. NCSR D-Helium concentration contours on y-injection plane with the RNG-LES at 3740 s (left, top), 10000 s (right, top) and 20000 s (bottom).

Comparing all the models it can be concluded that RNG-LES performs better, with $k-\epsilon$ to follow. On the other hand, laminar model performs poorly.

Finally, Figure 2-46 presents the flammable mass (g) inside the GARAGE facility as predicted by each model. It is shown that RNG-LES model predicts the lowest flammable mass inside the facility. The maximum flammable mass predicted by RNG-LES is less than 1 g and it is achieved at the time that the release stopped. Then, it reduced abruptly and it reaches zero before 4000 s. The $k-\epsilon$ model exhibits similar time evolution with maximum flammable mass below 5 g. Laminar model predicts much higher flammable mass with maximum value approximately equal to 142 g. This supports the remark that the diffusion is less in the laminar model resulting in a more stratified mixture, and therefore more flammable mass is accumulated inside the facility. Moreover, the flammable mass decreased at slower rate after the stop of the release and even at 8000 s it has not become zero.

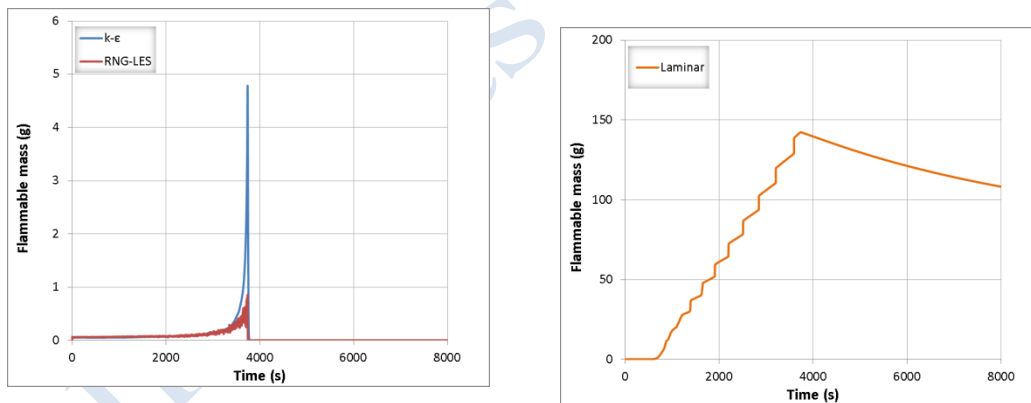


Figure 2-46. NCSR D-Predicted flammable mass inside the GARAGE facility.

1.1.4.4 Results from UU

UU performed simulations with LES Dynamic S-L and RNG-LES turbulence model. Figure 2-47 shows the mass balance and the mass error during the simulations with each model.

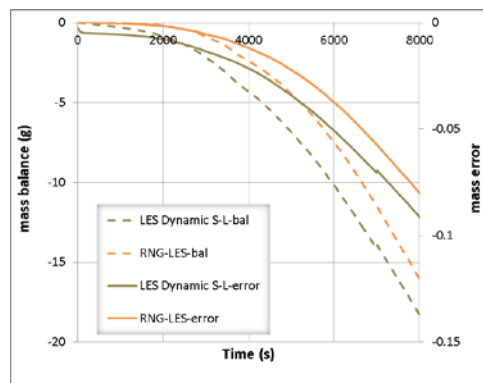


Figure 2-47. UU-The mass balance and the mass error during the simulations.

Figure 2-48 shows the predictions with both models compared with the experiment at several sensors. At this point it should be pointed out that the presented results using the LES Dynamic S-L are with Grid 2, while the results using the RNG-LES model are with Grid 1.

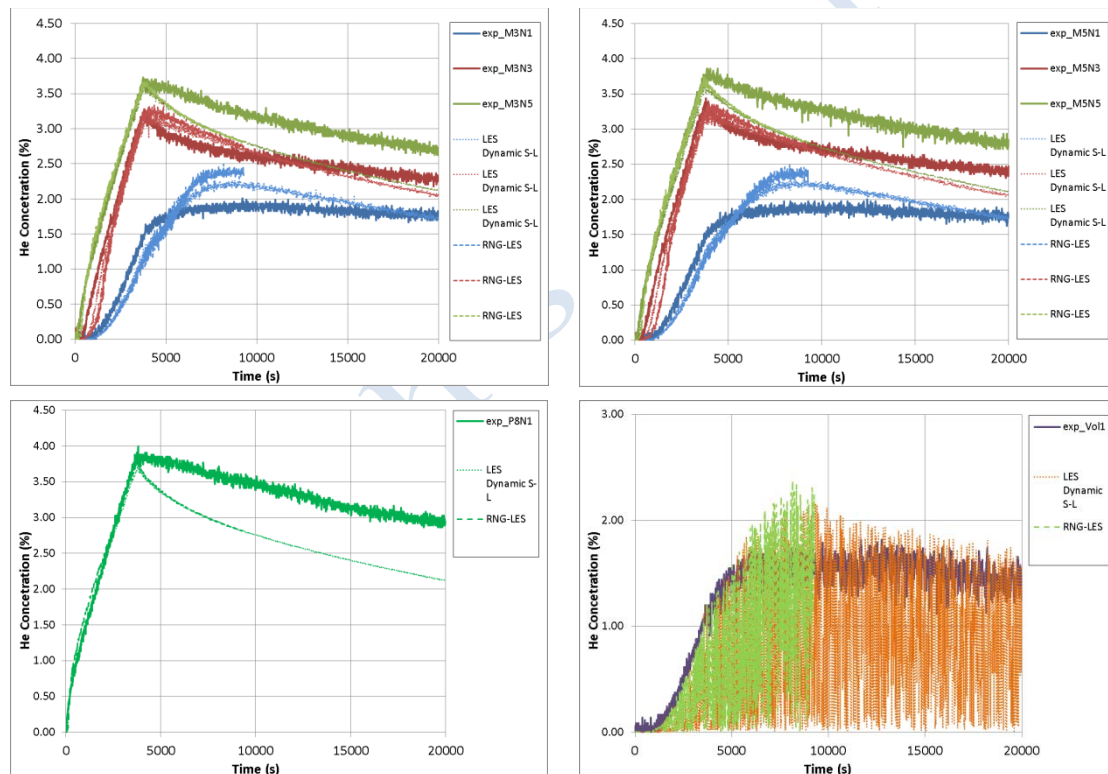


Figure 2-48. UU-Comparison of the results using LES Dynamic S-L and RNG-LES turbulence model with the experiment.

The results are almost the same using both turbulence models at most of the sensors. The largest differences are observed at the lower sensors (e.g. M3N1), still they are smaller than 5% and during the diffusion period (after the release has stopped).

For the sensors placed approximately in the middle of the facility (red curves in Figure 2-48) both predictions are in good agreement with the measurements.

However, both predictions overestimate the concentrations at the lower of the facility and underestimate them at the upper part during the diffusion period compared with the experiment. This behavior means that LES Dynamic S-L and RNG-LES model predict smaller stratification compared to the experiment.

Figure 2-49 and Figure 2-50 illustrate the predicted concentration contours on the y-injection point with LES Dynamic S-L and RNG-LES model, respectively, at different times.

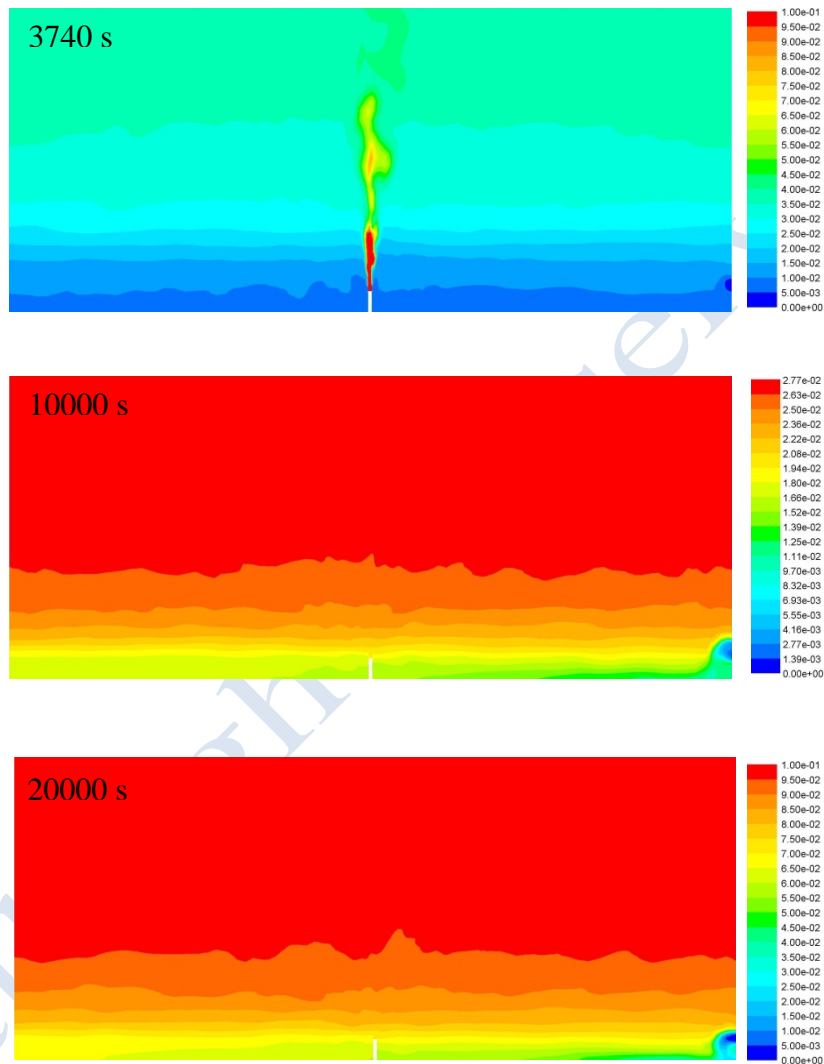


Figure 2-49. UU-Helium concentration contours on y-injection plane with LES Dynamic S-L at 3740 s (top), 10000 s (right, center) and 20000 s (bottom). The hole is on the right side.

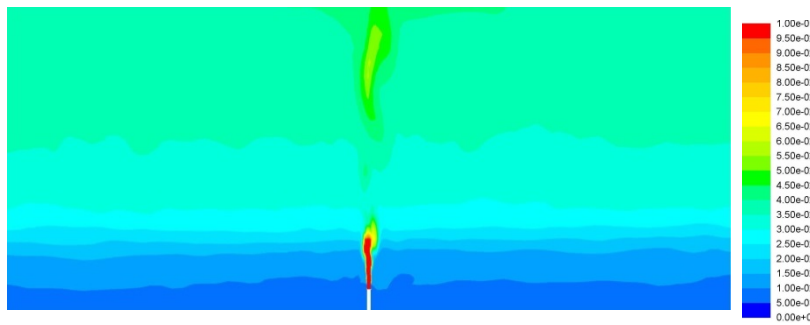


Figure 2-50. UU-Helium concentration contours on y-injection plane with RNG-LES at 3740 s. The hole is on the right side.

Finally, Figure 2-51 presents the predicted by each model flammable mass (g) inside the GARAGE facility. The RNG-LES model predicts higher peak flammable mass inside the facility. Both models predict that as soon as the release is stopped. The flammable mass decreased abruptly and reaches zero before 4000 s.

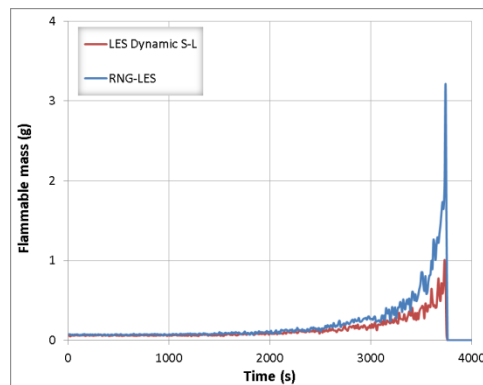
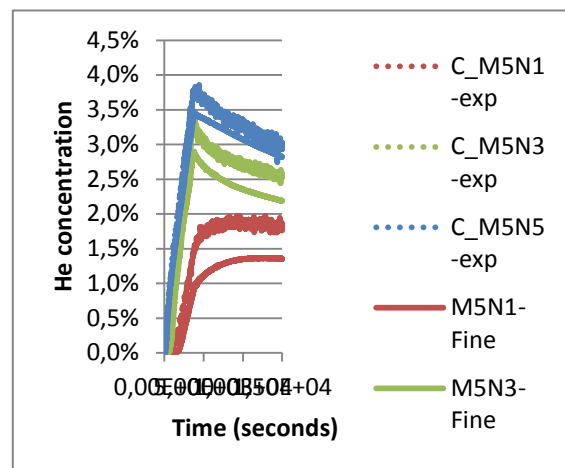


Figure 2-51. UU-Predicted flammable mass inside the GARAGE facility.

1.1.4.5 Results from EE

EE performed simulations with the LES model. A comparison with experimental (exp) data is shown below.



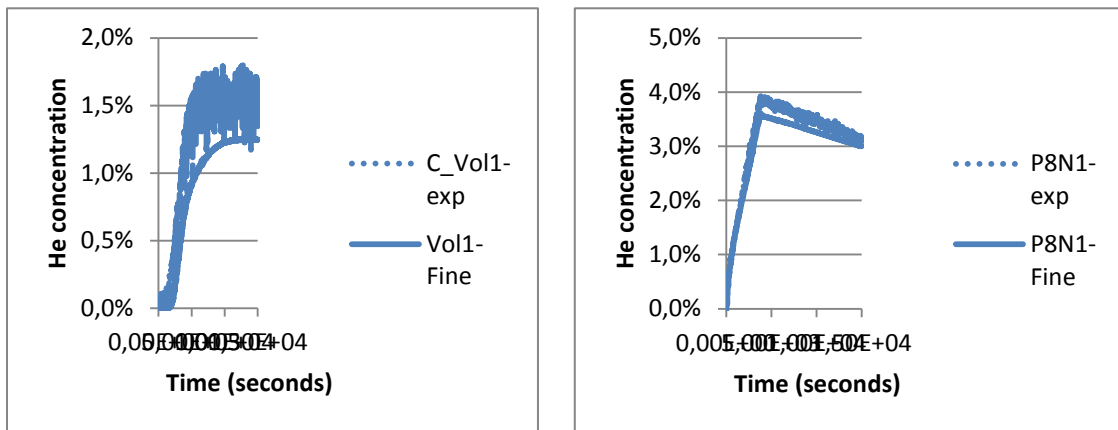
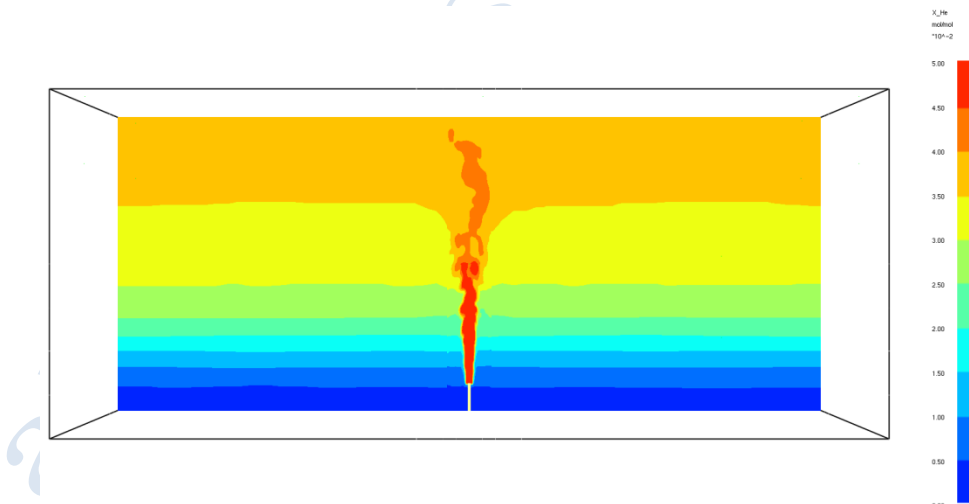


Figure 2-52. EE-Comparison of the results using LES model with the experiment.

There is generally good correlation with all sensors, although there is a general under-prediction of concentration which is most marked during the injection phase. As noted previously, this discrepancy is relatively small for sensors high up in the domain (i.e. P-sensors are more closely predicted, including some small overpredictions of concentration), but for lower sensors this difference is more marked. As noted before and by other simulators (e.g. UU) this may indicate that the LES modeling approach is insufficiently diffusive during the injection phase. Following this, during the diffusion phase the difference between simulation and experiment is reduced; this would indicate that the representation of diffusion is more accurate, and that over time the under-predictions of concentration become less marked.



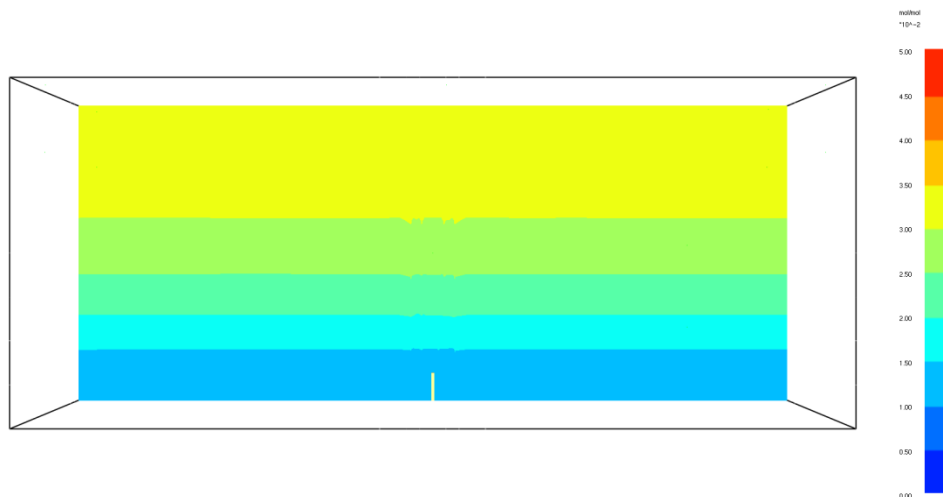


Figure 2-53. EE-Contours of He concentration at 3740 s (top) and 10,000 s (bottom).

Figure 2-53 shows the predicted He concentration contours on the y-injection point at 3740 s and 10000 s.

Finally, Figure 2-54 presents the predicted level of flammable mass (g) inside the GARAGE facility. As with most of the other predictions given above, the mass is predicted to rise to a peak and then abruptly drop to zero following cessation of He injection. The peak of ca. 1.6g is consistent with the LES results from UU presented above.

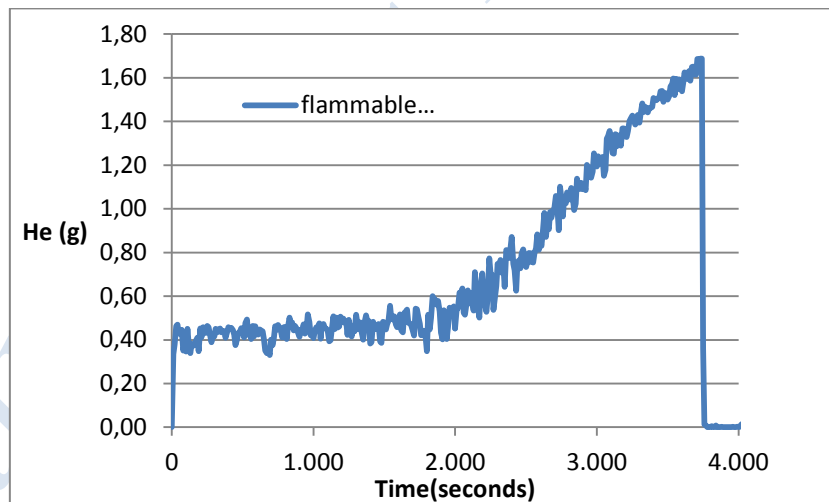


Figure 2-54. EE-Predicted flammable mass inside the GARAGE facility.

1.1.5 Comparison of the results by all partners

Figure 2-55 shows the results by JRC and NCSR D with the laminar model compared with the measurements. The JRC results are with the only hexahedral mesh. No grid independency study was performed for this type of mesh. However, a medium-size grid was used and the results are almost identical with the NCSR D grid independent results. Therefore, these results are also presented here.

Both NCSR D prediction and JRC prediction exhibit poor performance with underprediction of the concentration in the lower part of the facility and overprediction in the upper part. Therefore, the laminar model can not be considered as a good model for the examined case and cannot capture accurately the physical behavior.

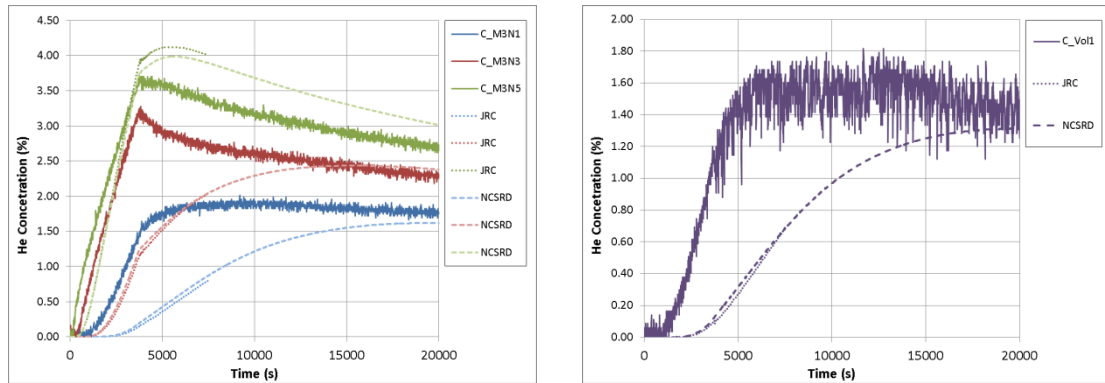


Figure 2-55. Comparison of the results by JRC and NCSR D partner with the laminar model.

Figure 2-56 shows the results by NCSR D and UU with the RNG-LES turbulence model compared with the measurements. Both predictions perform well during the release period. NCSR D prediction is in very good agreement with the experiment during the diffusion phase, too. In general, NCSR D-RNG-LES provides results almost identical to the measurements during both phases at most of the sensors. UU-RNG-LES agrees with the experiment very well as far as the peak concentration is concerned at the highest sensors. However, it tends to overestimate the diffusion during the diffusion phase and therefore it under-predict the concentrations near the ceiling and over-predict them near the bottom.

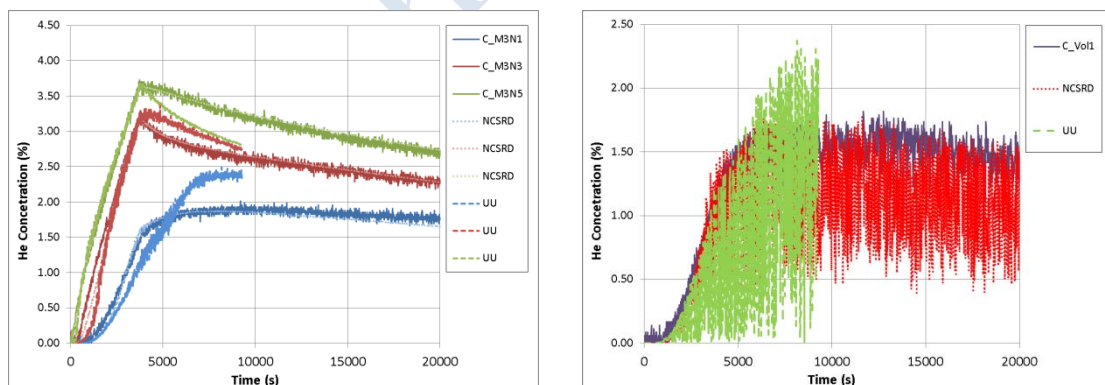


Figure 2-56. Comparison of the results by NCSR D and UU partner with the RNG-LES.

Finally, comparing the performance of the RANS models (SST and $k-\epsilon$) both models seem to provide results very close to the experiment (see Figure 2-38 and Figure 2-42). $k-\epsilon$ model predicts almost the same concentration levels as the experiment at the top and middle sensors, while SST model gives also results very close to the experiment at the middle sensors. However, $k-\epsilon$ model tends to under-predict the concentrations at the lower sensors during the diffusion period, whereas SST model tends to under-predict the concentrations at all sensors during the diffusion period.

1.1.6 Statistical analysis

In order to evaluate the models' performance statistical analysis was performed. Four statistical performance measures were used, as it is suggested in "Best Practice in Guidelines in numerical simulations" (SUSANA D3.1, 2014): Fractional bias (FB), normalized mean square error (NMSE), geometric mean bias (MG) and geometric mean variance (VG).

The model performance measures are derived by,

$$FB = 2 \frac{\bar{C}_o - \bar{C}_p}{\bar{C}_o + \bar{C}_p} \quad (1.3)$$

$$NMSE = \frac{\overline{(C_o - C_p)^2}}{\bar{C}_o \cdot \bar{C}_p} \quad (1.4)$$

$$MG = \exp \left[\ln \left(\frac{\bar{C}_o}{\bar{C}_p} \right) \right] \quad (1.5)$$

$$VG = \exp \left[\overline{\left(\ln \frac{C_o}{C_p} \right)^2} \right] \quad (1.6)$$

The overbar denotes the average over the entire dataset. Positive values of FB and values larger than unity of the MG indicate an overall underprediction of the model.

The statistical analysis was performed for all the models of all partners and is presented in Table 2-8-Table 2-10. Since no steady state is achieved the statistical analysis was performed for the peak concentration (release period), the concentration at 7000 and 20000 s (diffusion period) over all sensors. Some simulations have been stopped before reaching 20000 s or did not achieve grid independency; therefore, the statistical measures for those simulations are missing from the tables.

Table 2-8. Model performance measures for the peak concentration.

	FB	NMSE	MG	VG
perfect model	0	0	1	1
AREVA-Low Re k- ω	0.047	0.003	1.048	1.003
JRC-SST	0.096	0.011	1.098	1.010
NCSRDLaminar	-0.340	0.354	0.812	1.242
NCSRDK- ϵ	0.026	0.004	1.042	1.008
NCSRDRNG-LES	0.029	0.0020	1.031	1.002
UU-LES Dynamic S-L	0.010	0.008	1.003	1.008
UU-RNG-LES	-0.027	0.010	0.964	1.011
EE-LES	0.11	0.02	1.14	1.31

Table 2-9. Model performance measures for time=7000 s.

	FB	NMSE	MG	VG
perfect model	0	0	1	1
AREVA-Low Re k- ω	-0.042	0.002	0.959	1.002
JRC-SST	0.057	0.005	1.053	1.004
NCSRDLaminar	-0.174	0.153	0.983	1.228
NCSRDK- ϵ	0.0002	0.002	1.009	1.003
NCSRDRNG-LES	$-2.4 \cdot 10^{-5}$	0.0012	0.999	1.001
UU-LES Dynamic S-L	0.095	0.026	1.085	1.027
UU-RNG-LES	0.084	0.027	1.069	1.027
EE-LES	0.031	0.002	1.031	1.063

Table 2-10. Model performance measures for time=20000 s.

	FB	NMSE	MG	VG
perfect model	0	0	1	1
AREVA-Low Re k- ω	0.059	0.006	1.063	1.006
JRC-SST	0.057	0.005	1.063	1.006
NCSRDLaminar	-0.095	0.018	0.922	1.015
NCSRDK- ϵ	0.005	0.002	1.010	1.003
NCSRDRNG-LES	-0.00068	0.002	1.0067	1.0034
UU-LES Dynamic S-L	0.224	0.0667	1.237	1.060

Based on FB and MG all models tend to overall under-predict the peak concentrations except from NCSRDLaminar and UURNG-LES. The least agreement is found from the NCSRDLaminar model, which has the highest FB value. All other models seem to overall perform pretty well with FB and MG values close to ideal values. NMSE and VG values indicate also small scatter. UU-LES Dynamic S-L is close to perfect model as far as the peak concentration is concerned with NCSRDK- ϵ , UURNG and NCSRDRNG to follow.

At 7000 s (diffusion period) NCSRDLaminar model tends to overall overpredict the concentrations. NCSRDRNG model and AREVA-Low Re k- ω tend to overpredict the concentrations, while for the rest models by all partners both FB and MG indicate an overall underprediction of the concentrations. NCSRDRND-LES and k- ϵ model is very close to perfect model according to the statistical measures with EE-LES to follow. In general, all models performed very well except for the laminar model, whose statistical measures deviate from the ideal ones the most.

Similar remarks can be made for the statistical analysis at 20000 s (diffusion period). NCSRDLaminar overall overpredict the concentrations. AREVA-Low Re k- ω and JRC-SST have small differences and they both tend to under-predict the concentrations. UU-LES Dynamic S-L also underpredicts the concentration. NCSRDRNG-LES model seems to perform better with slight underprediction based on MG. NCSRDK- ϵ model performs also very well with slight tendency to under-predict the concentrations.

In addition, a plot of MG versus VG for the peak concentration is used for a systematic evaluation and is presented in Figure 2-57. This type of plot shows a parabola which represents the “minimum VG” curve for a given MG. All points should lie either on the parabola or inside. A perfect model would be the one that would be located on the parabola vertex (1,1). The points that lie on the left hand side of the parabola show a tendency to overpredict, while the opposite shows a tendency to under-predict. The vertical lines at MG=0.5 and MG=2 represent a factor of two over and under-prediction, respectively.

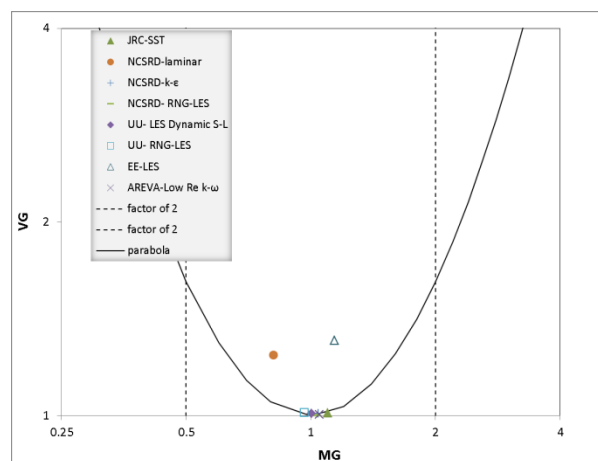


Figure 2-57. Geometric mean bias (MG) versus geometric mean variance (VG) for peak helium concentration.

Most of the models lie near the parabola vertex indicating very good agreement with the experiment. However, NCSRDL-laminar and EE-LES predictions do not lie on the parabola, but still they over and under-predict the concentrations, less than a factor of two.

1.1.7 Concluded remarks

In the framework of the SUSANA project a benchmarking exercise has been performed and five partners have been participated: AREVA, EE, JRC, NCSRDL and UU. For the benchmarking exercise the GARAGE experiment was used involving helium release inside a garage like facility. The facility has a small vent placed in the lower part of one wall. Helium is released vertically upwards and the injection point is placed in the middle of the floor and 220 mm above it.

Each partner used different CFD codes and several turbulent models to simulate the experiment. Several sensitivity studies were conducted by all partners, such as grid, domain and time step sensitivity studies, as “Best Practice in Guidelines in numerical simulations” (SUSANA D3.1, 2014) is suggested. AREVA used the low Reynolds $k-\omega$ model, JRC used the laminar model, the SST transitional and the DES turbulence model. NCSRDL used the laminar model, the $k-\epsilon$ and the RNG-LES turbulence model,

UU used the LES Dynamic S-L and the RNG-LES turbulence model, and EE used the LES model.

The final independent predictions are compared with the measurements using the time series at several sensors. The JRC-laminar and the JRC-DES predictions did not achieve grid independent solution (due to the high computational cost demanded for finer meshes), and thus they are not compared with the experiment. Based on the grid type sensitivity study it was shown that tetrahedral mesh produces high numerical diffusion. The tendency the mixture to become less diffusive (and in less agreement with the experiment) as the grid is refined (less numerical diffusion) is evident from the grid sensitivity study.

JRC predictions with SST model were in good agreement with the experiment. AREVA prediction with low Reynolds $k-\omega$ provides satisfactory results at most sensors and during both release and diffusion phase. However, it overpredicts the arrival time of the peak concentration.

NCSR prediction with $k-\epsilon$ model performs very well, though it tends to slightly under-predict the concentrations at the bottom sensors. RNG-LES model gives also very good results almost identical to the measurements at all sensors. Laminar model performs poorly with tendency to under-predict the concentrations at the bottom sensors and to overpredict them at the top sensors, indicating less diffusion and resulting in more stratified mixture inside the facility.

UU predictions with both LES models are similar to each other and consistent with the experiment. During the release both models are in very good agreement with the experiment. However, during the diffusion period (after the release has stopped) they seem to be more diffusive compared to the experiment, and thus, they predict higher concentrations at the bottom sensors and lower concentrations at the top sensors.

EE predictions are consistent with the experiment, although diffusivity during the injection period seems to be under-predicted. Following the injection period, the purely diffusion driven flow fields are better predicted.

Comparing the predictions with the same models performed by different partners, it is shown that JRC-laminar model using hexahedral mesh and NCSR-laminar model (also with hexahedral mesh) are almost identical at most of the sensors. Based on the performance of the laminar model it can be concluded that in the examined case the flow is turbulent (though the low Reynolds number at the pipe exit) and therefore the laminar model cannot capture the real physical behavior. However, when a hybrid mesh is used the artificial numerical diffusion that the tetrahedral cells produce acts like turbulent diffusion and improves the prediction considerably. This can lead to false conclusion that the laminar model performs well in the examined case. The significance to compare the grid independent results with the measurement before making any conclusions is highlighted.

Both RNG-LES simulations are in good agreement with the experiment during the release phase. However, NCSR-D-RNG-LES prediction performs better, especially during the diffusion phase, where UU-RNG-LES tends to under-predict the concentrations at the higher sensors and overpredict them at the lower sensors.

To evaluate the models' performance a statistical analysis has also been performed in accordance with "Best Practice in Guidelines in numerical simulations". Four statistical performance measures were used, FB, NMSE, MG and VG. According to these measures the peak concentration is slightly under-predicted by all models except for NCSR-D-laminar and UU-RNG-LES. All models except from laminar model performed overall very well as far as the concentrations at both 7000 and 20000 s. The best performance overall is exhibited by NCSR-D-RNG-LES model with $k-\epsilon$ model to follow very close.

1.1.8 References

Bragin, M., Makarov, D. & Molkov, V., 2013. Pressure limit of hydrogen spontaneous ignition in a T-shaped channel. *International Journal of Hydrogen Energy*, 38, pp.8039–8052. Available at: <http://www.sciencedirect.com/science/article/pii/S0360319913006393> [Accessed November 2, 2015].

Gupta, S. et al., 2009. Hydrogen related risks within a private garage: Concentration measurements in a realistic full scale experimental facility. *International Journal of Hydrogen Energy*, 34(14), pp.5902–5911. Available at: <http://linkinghub.elsevier.com/retrieve/pii/S0360319909003759> [Accessed May 15, 2015].

Kone, H.O., *Computational Fluid Dynamics softwares to predict large scale (industrial) explosions: capabilities and limitation, Ph.D thesis.*

Landa, P.S. & McClintock, P.V.E., 2004. Development of turbulence in subsonic submerged jets. *Physics Reports*, 397(1), pp.1–62.

Molkov, V. & Shentsov, V., 2014. Numerical and physical requirements to simulation of gas release and dispersion in an enclosure with one vent. *International Journal of Hydrogen Energy*, 39(25), pp.13328–13345.

Ungate, C., Harleman, D. & Jirka, G., 1975. Stability and mixing of submerged turbulent jets at low Reynolds numbers. *Energy Laboratory Report*. Available at: <http://dspace.mit.edu/handle/1721.1/27517> [Accessed November 6, 2015].

Versteeg, H. & Malalasekera, W., 2007. *An introduction to computational fluid dynamics: the finite volume method*, Available at: <http://www.mie.utoronto.ca/labs/mussl/cfd20.pdf> [Accessed November 13, 2014].

1.2 GAMELAN experiment

This experiment was simulated by AREVA.

1.2.1 Experimental description

The experimental set up (Cariteau & Tkatschenko, 2013) is a parallelepiped enclosure with a square base of 0.93m width and 1.26m height. The examined case has an opening of total area 32400 mm² (vent c: 930 x 35 mm).

The vent is located in the middle of the wall and 20mm below the ceiling. Figure 2-58 shows the schematic diagram of the facility. Helium is injected in the enclosure through a 5 mm nozzle. The injection point is located in the middle of the floor and 0.21 m from it and the release rate is 180 NL/min. the release is in quiescent environment and the ambient temperature is 295.51 K. Experimental geometry and conditions are summarized in Table 2-11.

Table 2-11. Summary of the experimental conditions.

Enclosure dimension l × w × h (mm)	Vent dimension w × h (mm)	Nozzle diameter D (mm)	Nozzle height (mm)	Release rate Q _{HE} (NL/min)	T (K)
930 × 930 × 1260	930 x 35	5	210	180	295.51

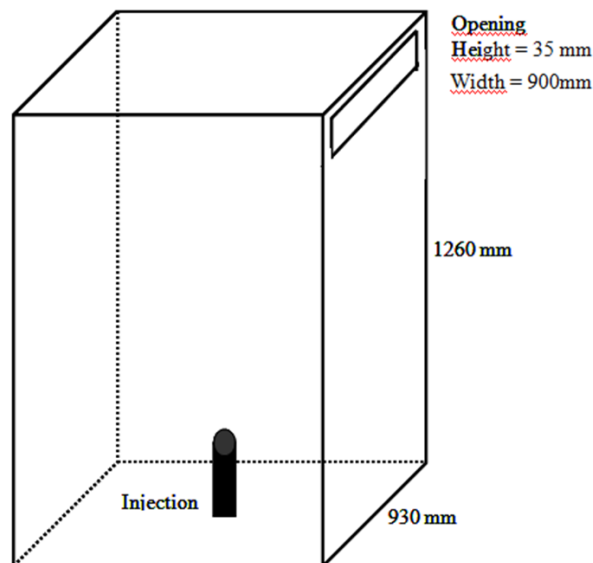


Figure 2-58. : Experimental environment of GAMELAN (Open box with a vent in the upper part).

Helium concentration sensors (catharometers) were placed on three vertical masts (M1, M2 and M4). All are located off the axis of the injection. In the following, the focus is laid on mast M1, given that the workable experimental results that we have are those of the mast M1. The details of the arrangement are given in Figure 2-59.

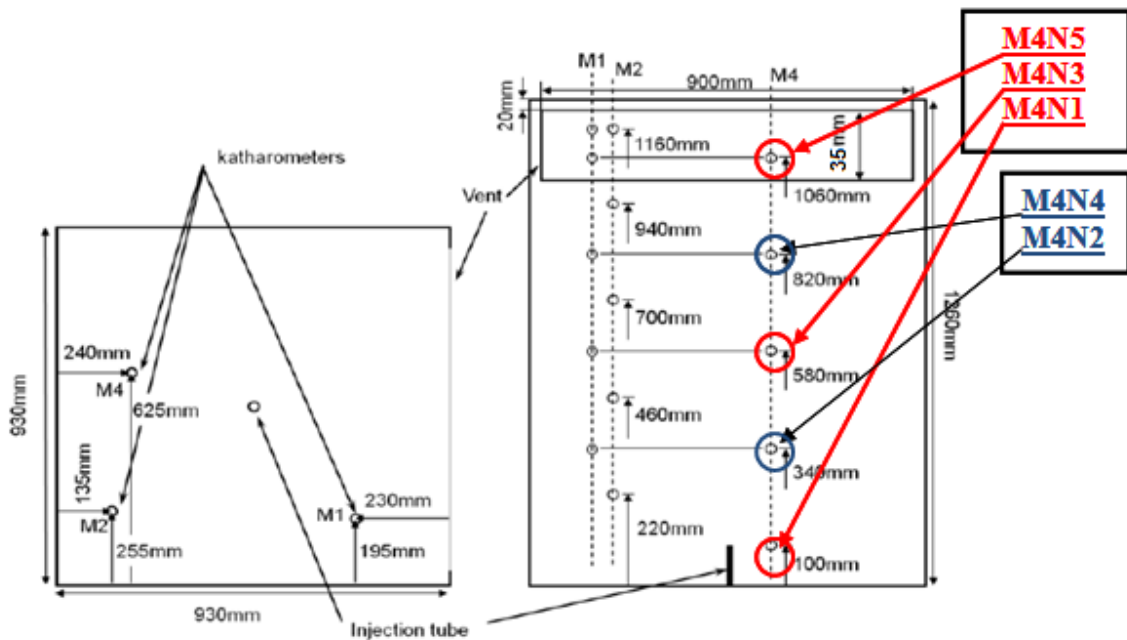


Figure 2-59. Experimental setup scheme, top view on the left and side view on the right.

1.2.2 Modelling approach

The main parameters of the CFD simulations are:

- CFD code: MERLIN (home code of INERIS establish on MATLAB)
- Isothermal simulation.
- Source modelled as a 2D
- Facility wall thickness 5 mm.
- Symmetry is assumed. Simulation made on a half domain
- The computational domain outside the box is extended in all the three directions to avoid boundary conditions at the opening.
- Model used: low Reynolds $k-\omega$

To simulate the experiments, a three dimensional calculation was performed using “Non-reacting flows” solver of the numerical toolbox MERLIN.

The equations were slightly modified to introduce the buoyancy terms both in the averages equations and in the turbulence equations:

❖ Mass equation

$$\frac{\partial \bar{\rho}}{\partial t} + \frac{\partial \bar{\rho} \tilde{u}}{\partial x} + \frac{\partial \bar{\rho} \tilde{v}}{\partial y} + \frac{\partial \bar{\rho} \tilde{w}}{\partial z} = 0 \quad [16]$$

❖ Momentum equation following the x direction

$$\frac{\partial \bar{\rho} \tilde{u}}{\partial t} + \frac{\partial \bar{\rho} \tilde{u}^2}{\partial x} + \frac{\partial \bar{\rho} \tilde{u} \tilde{v}}{\partial y} + \frac{\partial \bar{\rho} \tilde{u} \tilde{w}}{\partial z} = -\frac{\partial \bar{P}}{\partial x} + (\mu_l + \mu_t) \left[\frac{\partial^2 \tilde{u}}{\partial x^2} + \frac{\partial^2 \tilde{u}}{\partial y^2} + \frac{\partial^2 \tilde{u}}{\partial z^2} \right] \quad [17]$$

❖ Momentum equation following the y direction

$$\frac{\partial \bar{\rho} \tilde{v}}{\partial t} + \frac{\partial \bar{\rho} \tilde{u} \tilde{v}}{\partial x} + \frac{\partial \bar{\rho} \tilde{v}^2}{\partial y} + \frac{\partial \bar{\rho} \tilde{v} \tilde{w}}{\partial z} = -\frac{\partial \bar{P}}{\partial y} + (\mu_l + \mu_t) \left[\frac{\partial^2 \tilde{v}}{\partial x^2} + \frac{\partial^2 \tilde{v}}{\partial y^2} + \frac{\partial^2 \tilde{v}}{\partial z^2} \right] \quad [18]$$

❖ Momentum equation following the z direction

$$\begin{aligned} & \frac{\partial \bar{\rho} \tilde{w}}{\partial t} + \frac{\partial \bar{\rho} \tilde{u} \tilde{w}}{\partial x} + \frac{\partial \bar{\rho} \tilde{v} \tilde{w}}{\partial y} + \frac{\partial \bar{\rho} \tilde{w}^2}{\partial z} \\ & = -\frac{\partial \bar{P}}{\partial z} + (\mu_l + \mu_t) \left[\frac{\partial^2 \tilde{w}}{\partial x^2} + \frac{\partial^2 \tilde{w}}{\partial y^2} + \frac{\partial^2 \tilde{w}}{\partial z^2} \right] + g(\rho - \rho_a) \end{aligned} \quad [19]$$

As previously, we decide to not resolve the energy equation because the rejected helium has the same temperature as the ambient air.

Given that Helium is injected in the air, the system of equation has to contain the species equation to take into account the apportionment of Helium in the chamber.

❖ Species equation

$$\begin{aligned} & \frac{\partial \bar{\rho} \tilde{C}}{\partial t} + \frac{\partial \bar{\rho} \tilde{u} \tilde{C}}{\partial x} + \frac{\partial \bar{\rho} \tilde{v} \tilde{C}}{\partial y} + \frac{\partial \bar{\rho} \tilde{w} \tilde{C}}{\partial z} \\ & = \frac{\partial}{\partial x} \left[\left(\bar{\rho} D_1 + \frac{\mu_t}{Sc_t} \right) \frac{\partial \tilde{C}}{\partial x} \right] + \frac{\partial}{\partial y} \left[\left(\bar{\rho} D_1 + \frac{\mu_t}{Sc_t} \right) \frac{\partial \tilde{C}}{\partial y} \right] + \frac{\partial}{\partial z} \left[\left(\bar{\rho} D_1 + \frac{\mu_t}{Sc_t} \right) \frac{\partial \tilde{C}}{\partial z} \right] \end{aligned} \quad [20]$$

In reality, the k-ε model is valid, strictly speaking, far from wall boundaries. For the boundaries layers flows, the model does not provide damping for the turbulent parameters in the near boundary region and in fact, the application of the model as it is, for the boundary layer flows lead to the wrong profiles of velocity (more precisely, the velocity profile does not follow the well know “boundary law”) which may impact the helium concentration prediction, especially at sensor M4N1, given that it is located at 110 mm below of the output of the injection tube (in the boundary layer) where the effect of viscosity may be preponderant in view of the weak Reynolds number in that region (the injection is not directed in that region, it is rather the gravity effect which favors the drop of helium until the position of the sensor M4N1). The same ascertainment is done for the sensor M1N5 and M2N5 not because of the Reynolds number but rather their proximity to the upper wall.

An alternative consists in using the low Reynolds number k-epsilon model which resolves the flow everywhere. It contains two damping terms, and: the function that appears in the term of “dissipation of the dissipation” (see chapter 3 of the PHD thesis memory, (Kone, Ph.D in progress)) considers the effects of the low local Reynolds number near to the boundary, which contributes to the growth of ε in this zone; the function which intervenes in the calculation of is a damping function permitting to quickly decrease the turbulent viscosity in the zone of near boundary. It is a logical extension of the standard k-epsilon model and shares many of its advantages, but uses more memory.

In view of the reasons given above, the low Reynolds number k-epsilon model is retained for this simulation and the two transport equations that compose this model are written as follow:

$$\frac{\partial(\bar{\rho}k)}{\partial t} + \frac{\partial(\bar{\rho}\tilde{u}_j k)}{\partial x_j} = \bar{\rho}\tau R_{ij} \frac{\partial \tilde{u}_i}{\partial x_j} - \bar{\rho}\varepsilon^* + P_b + \frac{\partial}{\partial x_j} \left[\left(\mu + \frac{\mu_t}{\sigma_k} \right) \frac{\partial k}{\partial x_j} \right] - D \quad [21]$$

$$\frac{\partial(\bar{\rho}\varepsilon^*)}{\partial t} + \frac{\partial(\bar{\rho}\tilde{u}_j \varepsilon^*)}{\partial x_j} = C_{\varepsilon 1} \frac{\bar{\rho}\varepsilon^*}{k} \left(\tau R_{ij} \frac{\partial \tilde{u}_i}{\partial x_j} + C_{3\varepsilon} P_b \right) - C_{\varepsilon 2} f_2 \bar{\rho} \frac{\varepsilon^{*2}}{k} + \frac{\partial}{\partial x_j} \left[\left(\mu + \frac{\mu_t}{\sigma_\varepsilon} \right) \frac{\partial \varepsilon^*}{\partial x_j} \right] + E \quad [22]$$

In these equations,

ε^* is a transformed variable introduced by Jones and Launder and it is written:	$\varepsilon^* = \varepsilon - 2\nu \left(\frac{\partial k^{\frac{1}{2}}}{\partial y} \right)^2$	[23]
D is an additional dissipation term and it is written:	$D = \bar{\rho}\varepsilon - \bar{\rho}\varepsilon^*$	[24]
μ_t is the turbulent viscosity and it is written:	$\mu_t = C_\mu f_\mu \bar{\rho} \frac{k^2}{\varepsilon}$	[25]
E is an additional turbulence production term and it is written:	$E = 2 \frac{\mu\mu_t}{\bar{\rho}} \left(\frac{\partial^2 u_i}{\partial x_j \partial x_k} \right) \left(\frac{\partial^2 u_i}{\partial x_j \partial x_k} \right)$	[26]
f_2 is the damping factor and it is written:	$f_2 = 1 - 0.3 \exp(-R_t^2)$	[27]
f_μ is also a dumping factor and it is written:	$f_\mu = \exp \left(\frac{-2.5}{1 + \frac{R_t}{50}} \right)$	[28]
R_t is the turbulent Reynolds number and it is written:	$R_t = \frac{k^2}{\nu\varepsilon}$	[29]
P_b is the term linked to buoyancy and it is written:	$P_b = - \frac{\mu_t}{\rho S c_t} g \nabla \rho$ Sc _t is the turbulent Schmidt number and its value is 0.7 in this study.	[30]

It is important to underline that in the case where one used the modified dissipation ε^* instead of the true dissipation ε , the conservation equation for k must be modified by including an additional term of dissipation D. Moreover, it is necessary to add to the equation of ε^* an additional term of production denoted E whose role is to increase the rate of dissipation in the buffer regions of the boundary layer in order to ensure a correct value of the maximum of k in the profile.

1.2.3 Mesh Generation

Given that the domain of study presents a plane of symmetry, for the simulation, only a half of the domain will be considered.

Using regular mesh in this study, it is very difficult to find a good compromise between the cells size which compose the mesh and the calculation power of the computer PILCAM for the simple reason that if we decide to have 5 nodes for example in the injection diameter (which is not sufficient to ensure the precision of the calculation), we will have to resolve the system of equations over 544,887,000 cells of size $10^{-3}\text{m} \times 10^{-3}\text{m}$, which is beyond the capability of PILCAM. An alternative consists in using an irregular mesh. We mesh the different zones of the geometry considering the importance of the flow and the sensitivity to the cells size in order to improve the simulation precision.

Before meshing the geometry, it is important to analyze carefully the jet considered in this study.

In the case of a jet with large momentum (180 NI/min), on the ceiling at the impact point, the jet spreads to a ceiling inducing gravity current. When it touches the side walls, it turns, forming a homogeneous layer of concentration in the upper part (Figure 2-60). More the rate of discharge at the orifice is important, more the homogeneous layer deals with the height in the chamber to extreme case where this layer completely fills the enclosure.

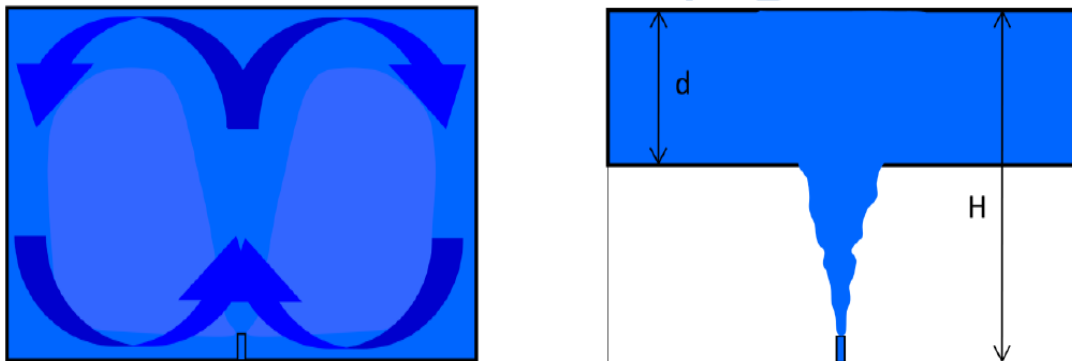


Figure 2-60. Homogeneous regime (left) and homogeneous layer regime (right).

According to the description done below, the zones to be meshed finely are the plume zone and the upper part of the chamber. The plume zone is meshed with an expansion of 12 degree, going from the origin of the jet to the ceiling which can represent the angle of jet expansion. The other parts of the chamber are meshed less finely. In Figure 2-61, the mesh used for this simulation is represented.

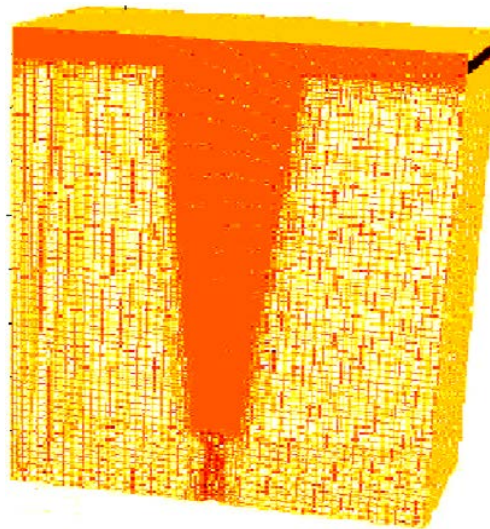


Figure 2-61. Mesh used to simulate GAMELAN.

The mesh presented in Figure 2-61 has been retained for this study after a study of sensitivity which proved that the convergence in mesh has been reached. Mesh grid size is an important factor in numerical simulations because resolving of the flow motions depends significantly on the grid size to accurately describe the flows. Thus, finding or developing the right model that can satisfy the engineering solutions without the need of fine grid size (cheap computational cost) is one of the biggest challenges engineers are facing nowadays. As the grid size gets finer, it inflicts a high computational cost because of the type of models used, such as the direct numerical simulation (DNS). In contrast, if the grid size gets coarser, this leads to use the models developed by approximations such as the Reynolds Average Navier- Stokes (RANS), which results poor description of the flow especially for the simulation of turbulent flows. Therefore, using the appropriate grid size is always crucial. Four grid size samples have been chosen to investigate the grid size effect on the results as shown in Table 2-12.

Table 2-12. Meshes used to simulate GAMELAN.

Meshes	Number of cells in the plume and the upper part of the chamber	Number of cells in the other part of the chamber	Number of nodes at the injection diameter	Total number of cells
Mesh1	544,214	625,420	5	1,169,634
Mesh2	2,825,314	3,325,712	12	6,151,026
Mesh3	5,555,000	6,533,644	20	12,088,644
Mesh4	6,514,312	7,630,255	24	14,144,567

The numerical results obtained for the lowest sensor of the mast 4 for the different meshes represented in the Table 2-12 are shown in Figure 2-62. According the different results obtained, it is clear that the convergence in mesh is obtained for mesh3. Therefore, the mesh3 is the reference mesh for the simulation of GAMELAN.

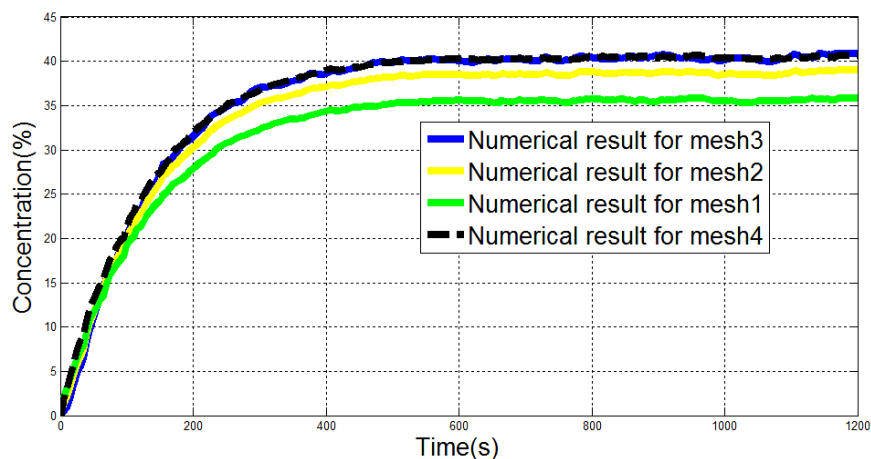


Figure 2-62. Numerical results of the lowest sensor of the mast 4 obtained with different meshes.

Concretely Gamelan has been simulated using in total 12,088,644 cells which can be decomposed as follow:

- 5,555,000 cells for the plume and the upper part of the chamber with 20 nodes at the injection diameter.
- 6,533,644 cells in the other parts of the domains.

1.2.4 Initial and Boundary condition

At the entrance of the helium jet:

- The ambient pressure (atmospheric pressure) is defined;
- The turbulence intensity is supposed to be 1%;
- The mass flow is imposed at the entrance (In each case, it is the global value of the mass flow which is imposed).
- The volume fraction of helium is supposed to be 1.
- An ambient temperature (273.15 K) is imposed at the entrance.

At the outlet (the vent):

- The atmospheric pressure is imposed;
- The inflow are normal to the output surface;
- The inflow turbulence is supposed to be 1%;
- The inflow mass of helium is zero;
- The ambient temperature is imposed.

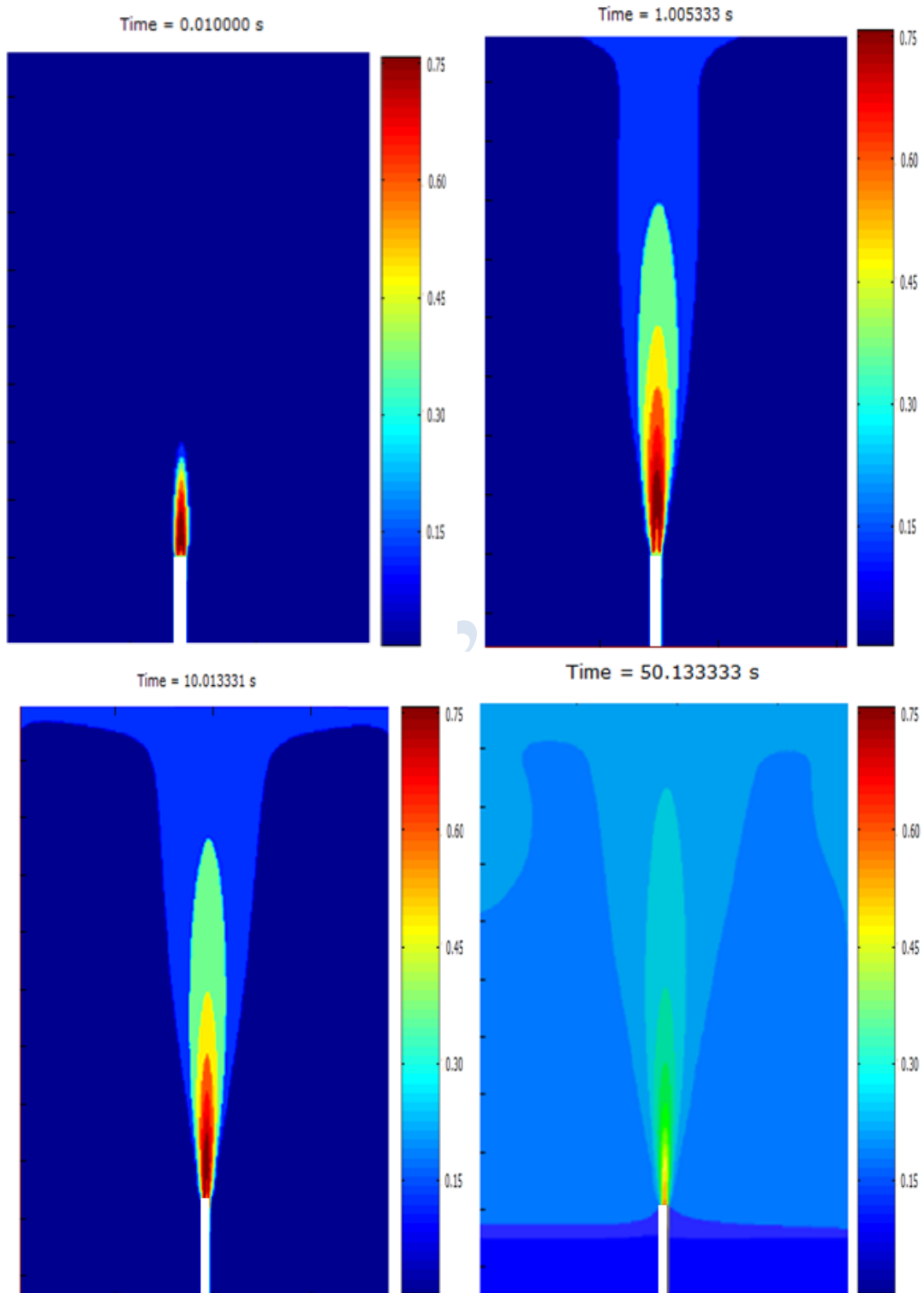
It is interesting to add at the beginning of the injection, the chamber contains air in Standard Temperature and Pressure (STP) conditions (273.15K/1bar).

1.2.5 Discretization of the system of equations

Without further indications, to solve the RANS equations, the time derivatives are first order solved explicitly. For the convective terms, FCT (Flux Corrected Transport) numerical scheme was used (Lax-Wendroff scheme for the high order flux estimator and Lax-Frederichs scheme for the low order flux estimator). A central derivation scheme is issued for the diffusive terms.

1.2.6 Results

The homogeneous regime is a limit case of the stratified regime when the injection conditions leads to the formation of a homogeneous layer of height equal to the height of the enclosure. This regime is obtained for the injection realized at 180NI/min from the tube of 5 mm of diameter.



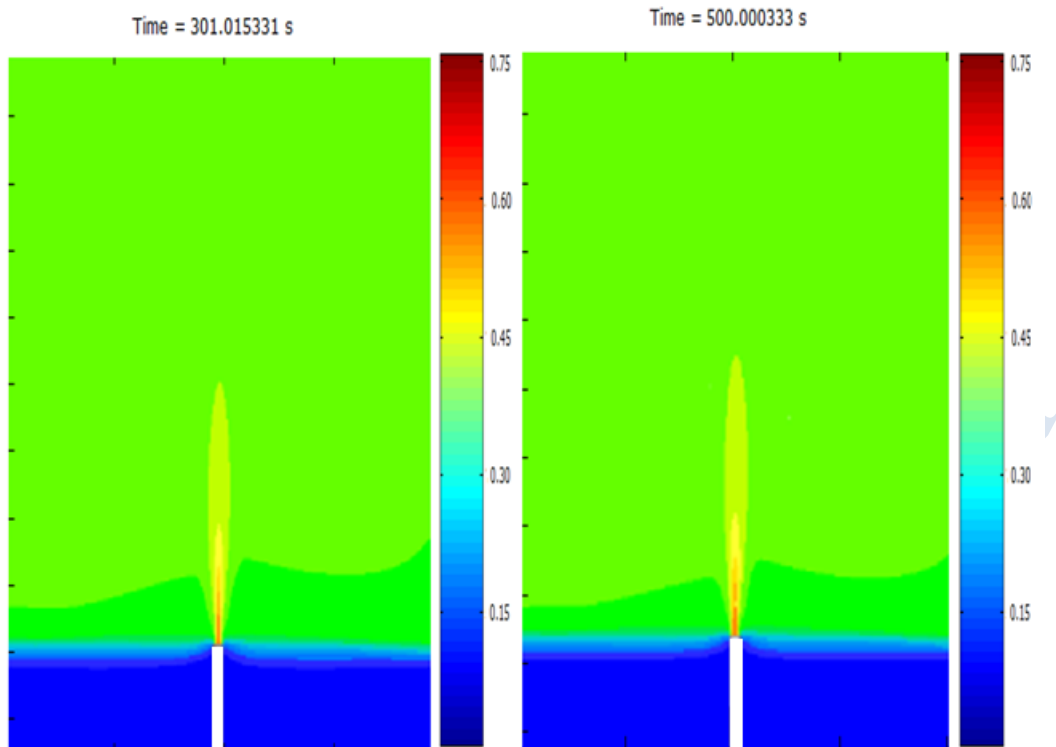


Figure 2-63. AREVA-Concentration of helium at different time.

Figure 2-63 shows the evolution of the volume fraction within the chamber according to the plane of symmetry x - z , and at several times of the study. At $t = 0.01$ s, the jet takes shape. Then, at $t = 1$ s, the gas mixture has impacted the top of the box and at $t = 10$ s, the gravity current is established and along the ceiling layer begins to order. At $t = 50$ s, the reversal phenomenon is out and already produced and filling front stands up to the discharge point but the mixture remains unevenly distributed in the layer formed. At $t = 300$ s and whatever the next moment, the formed layer is now homogeneous. A homogeneous regime is predicted numerically. This ascertainment is also confirmed by the profiles of the concentration registered by the different sensors of each mast which have approximately the same level (see Figure 2-64, Figure 2-65 and Figure 2-66). On these figures, the sensors are numbered from bottom to up. For example M4N1, indicates the sensor number 1 of the mast 4 which is the lowest (nearest to the ground) in term of position.

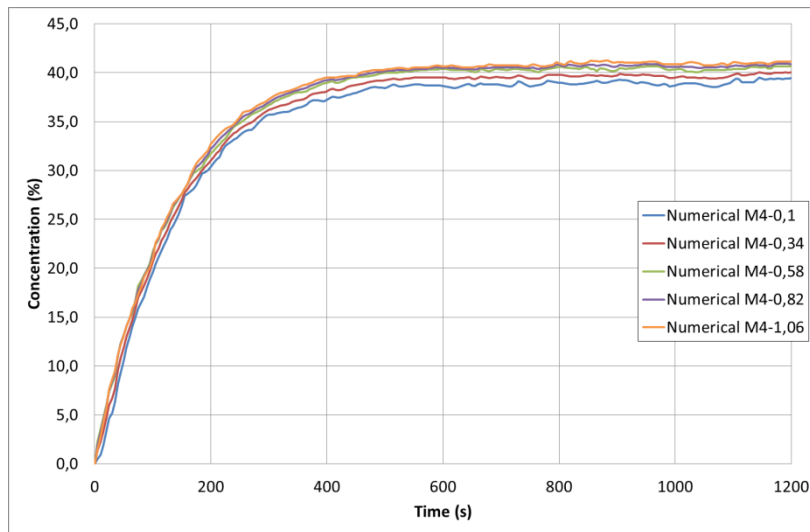


Figure 2-64. AREVA-Concentration of helium registered by the sensors of the mast4.

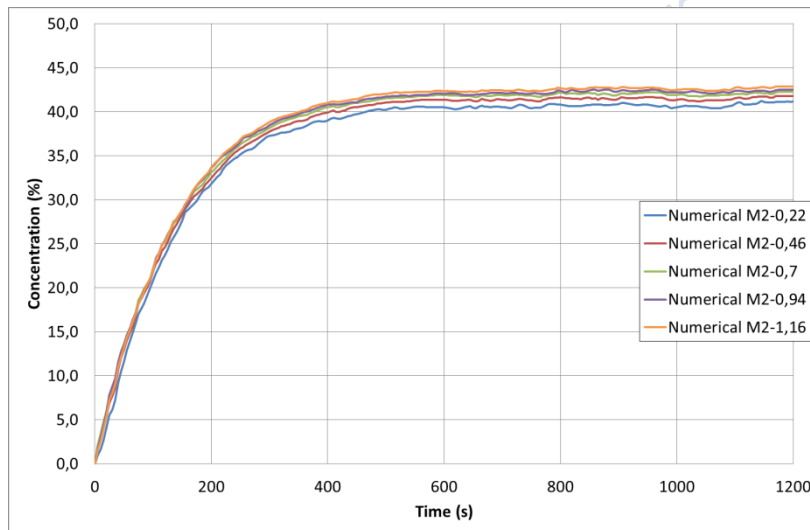


Figure 2-65. AREVA-Concentration of helium registered by the sensors of the mast2.

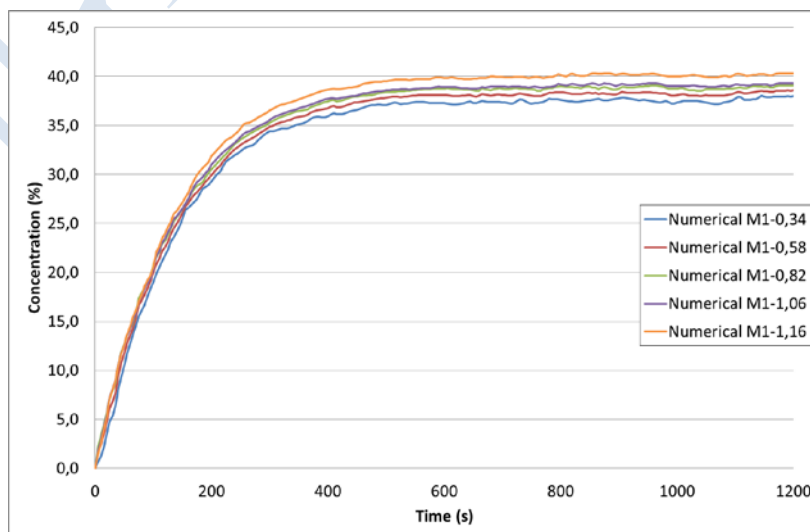


Figure 2-66. AREVA-Concentration of helium registered by the sensors of the mast1.

Comparing the concentration profiles (Figure 2-67-Figure 2-69) registered on the three masts during the numerical simulation to those found experimentally, it is clear that the numerical results obtained are good approximations of the experimental results. However, the numerical simulation tends to underestimate the results at most of the sensors.

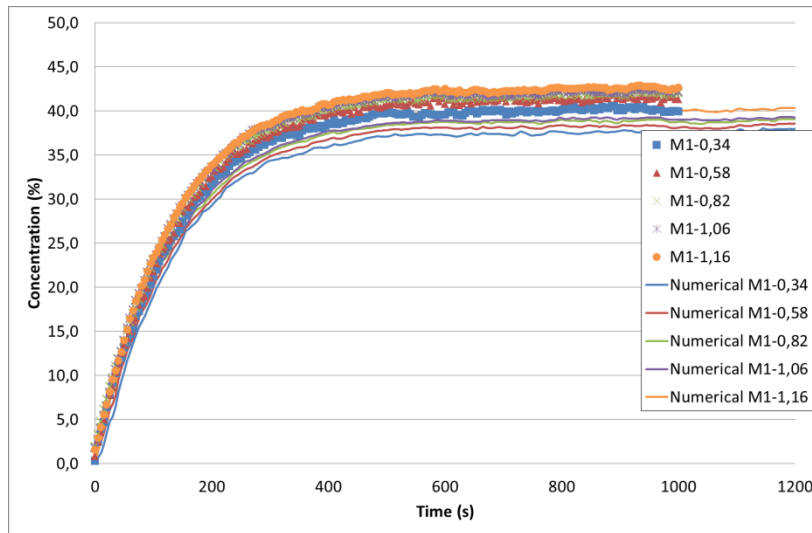


Figure 2-67. AREVA- Comparison between experimental and numerical concentration registered by the sensor of mast 1.

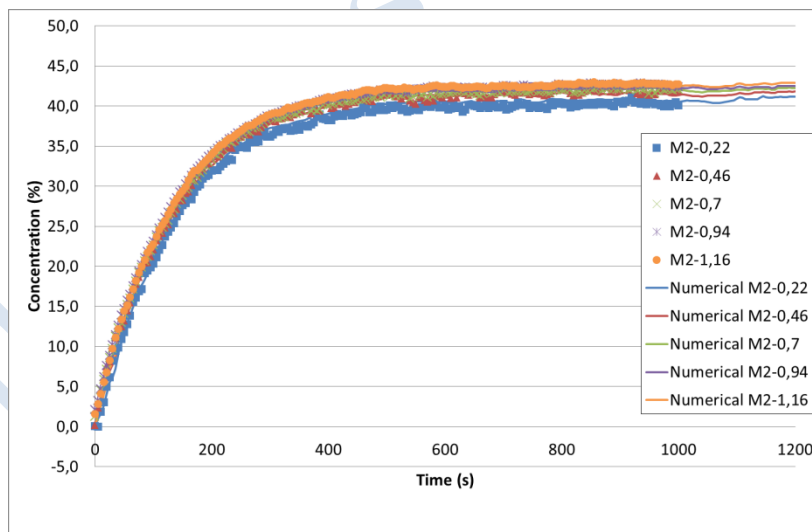


Figure 2-68. AREVA- Comparison between experimental and numerical concentration registered by the sensor of mast 2.

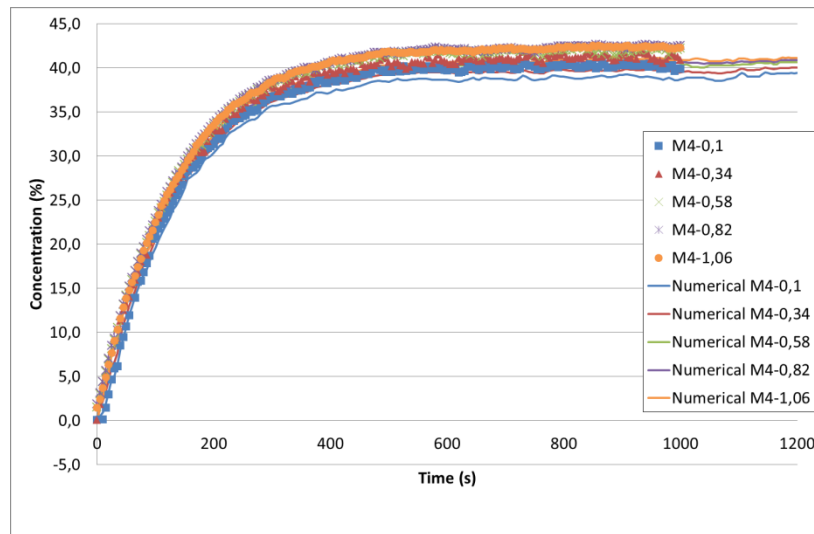


Figure 2-69. AREVA- Comparison between experimental and numerical concentration registered by the sensor of mast 4.

A statistical analysis has been also performed and Table 2-13 presents the statistical measures for the concentrations at steady state. With FB and MG absolute values very small the model can be considered as a “good” model. Moreover, the more the values of the statistical analysis are near their ideal values the better the model could be considered. The negative FB value and the MG value below unity reveal that the model tends to over-predict the helium concentration at steady state.

Table 2-13. Model performance measures.

	ideal	prediction
FB	0	0,033
NMSE	0	0,001
MG	1	1,034
VG	1	1,001

1.2.7 Conclusions

This work describes two physical situations that are frequently encountered in accidents appearing on fuel cell systems:

- The flows dominated by buoyancy, encountered on small leaks supposed statistically more frequent and acceptable (or close to the acceptability) from a security point of view;
- Rapid flows, for which the convection is dominant. These cases correspond to accidental situations encountered during breaks or pitting of pipes.

The numerical simulations give good results (compared to the experimental results) which is a consequence of the solidity of the methodology adopted.

It is interesting to underline that this level of approximation has been obtained after many works which consisted in finding the system of equations, the turbulence models, the discretization schemes and the mesh the most adapted to realize this case.

1.2.8 References

Cariteau, B., and I. Tkatschenko. 2013. "Experimental Study of the Effects of Vent Geometry on the Dispersion of a Buoyant Gas in a Small Enclosure." *International Journal of Hydrogen Energy* 38(19):8030–38. Retrieved May 5, 2014 (<http://linkinghub.elsevier.com/retrieve/pii/S0360319913007404>).

Kone, H.O., Computational Fluid Dynamics softwares to predict large scale (industrial) explosions: capabilities and limitation, Ph.D thesis.

Deflagration

This experiment was simulated by KIT.

1.3 Experiment overview

In the experiment, hydrogen-air stoichiometric mixture was contained in thin hemispherical polyethylene balloons of diameter $D= 20.0$ m. Ignition of the hydrogen-air mixture was given at the centre of the balloon of the ground level. Figure 3-1 shows experimental setup.

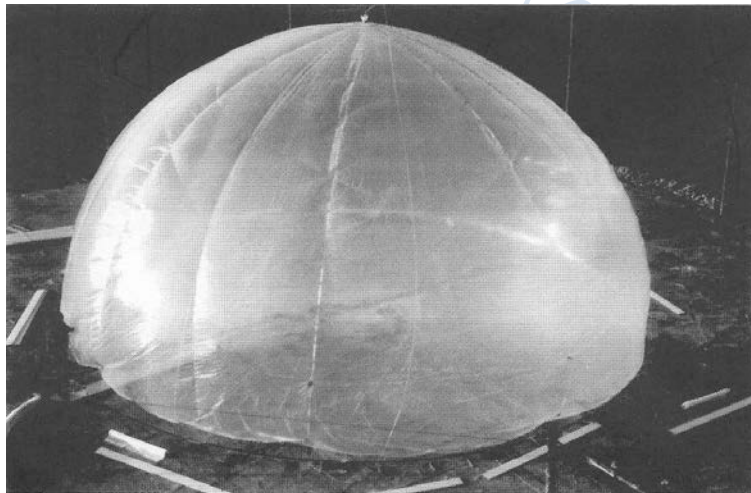


Figure 3-1. Experiment setup open deflagration

10 piezo-resistive kistler pressure sensors are used to detect the pressure data. The explosion pressure was measured at distances 2.0, 3.5, 5.0, 6.5, 8.0, 18, 25, 35, 60, and 80 m from the initiation point.

1.4 Mathematical methodology

1.4.1 Governing equations

To simulate the flow motion in the experiment open deflagration the standard $k-\varepsilon$ model is used. The standard set of equations in RANS for mass, momentum, energy and species reads,

$$(\bar{\rho})_t + (\bar{\rho} \bar{u}_j)_{x_j} = 0$$

$$(\overline{\rho u_j})_t + (\overline{\rho u_i u_j})_{x_j} = \overline{\rho} g_j - \overline{p}_{x_j} + M_{ij,x_j}$$

$$(\overline{\rho e})_t + ((\overline{\rho e} + \overline{p}) \overline{u_j})_{x_j} = \overline{\rho} g_j \overline{u_j} + \overline{u_i} M_{ij,x_j} + \left(\frac{\overline{\mu}}{C_h} \left(\overline{e} - \frac{1}{2} \overline{u_i u_j} + \frac{\overline{p}}{\overline{\rho}} \right)_{x_j} \right)_{x_j} + B + \rho \varepsilon$$

$$(\overline{\rho Y_\alpha})_t + (\overline{\rho Y_\alpha} \overline{u_j})_{x_j} = \left(\frac{\overline{\mu}}{C_h} \overline{Y_{\alpha,x_j}} \right)_{x_j} + \overline{\omega}_\alpha$$

and,

$$\overline{e} = \sum_{\alpha=1}^N \frac{\overline{Y_\alpha}}{\overline{\mu}_\alpha} (\overline{h}_\alpha + \Delta h_\alpha^0 - RT) + \frac{1}{2} \overline{u_j u_j}$$

$$\overline{Y_\alpha} = \frac{\overline{\rho}_\alpha}{\overline{\rho}}$$

The standard $k-\varepsilon$ model is formulated by the following equations

$$M_{ij} = -\frac{2}{3} \delta_{ij} (\overline{\rho k} + \overline{\mu u_{r,x_r}}) + \overline{\mu} (\overline{u_{i,x_j}} + \overline{u_{j,x_i}})$$

$$S = \overline{u_{i,x_j}} M_{ij} - B$$

$$B = \frac{\overline{\mu}}{C_\rho} \frac{1}{\overline{\rho}^2} \overline{\rho}_{x_r} \overline{p}_{x_r}$$

And additionally,

$$(\overline{\rho k})_t + (\overline{\rho k u_j})_{x_j} = S - \overline{\rho \varepsilon} + \left(\frac{\overline{\mu}}{C_k} \overline{k_{x_j}} \right)_{x_j}$$

$$(\overline{\rho \varepsilon})_t + (\overline{\rho \varepsilon u_j})_{x_j} = \frac{\overline{\varepsilon}}{k} [C_1 S - C_2 \overline{\rho \varepsilon}] + \left(\frac{\overline{\mu}}{C_{f_\alpha}} \overline{\varepsilon_{x_j}} \right)_{x_j}$$

with

$$\overline{\mu}_t = \overline{\mu} + C_\mu \frac{\overline{k}^2}{\overline{\varepsilon}}$$

Launder and Sharma provided an improved set of constant to the model, calibrated for tubes, in Table 3-1.

Table 3-1. Constants set for the Standard $k-\varepsilon$ method.

C_μ	C_1	C_2	C_k	C_ε
0.09	1.44	1.92	1.0	1.3

In simulation of such large scaling problem, more attention should be focused on the selection of chemical model. In this simulation the CREBCOM chemical model [1] is used. CREBCOM model belongs to the category of Forest Fire models pioneered by

Bak et al. in Ref [2]. The main characteristic of this model is that a cell starts burning when one or more of the surrounding cells is already consumed up to a limit. An advantage of CREBCOM model is that it does not introduce any special flag or indicator showing whether some cell is burning or not.

Let f be a progress variable of the reaction, equal to 0 for the fresh mixtures and to 1 for the completely developed reaction. Let us introduce the criteria value

$$F_{i,j,k} = f_{i+1,j,k}^2 + f_{i-1,j,k}^2 + f_{i,j+1,k}^2 + f_{i,j-1,k}^2 + f_{i,j,k+1}^2 + f_{i,j,k-1}^2 - 3f_{i,j,k}^2$$

Then CREBCOM burning criteria states that a cell is considered to be burning if F is more than $\left(\frac{1}{2}\right)^2$ That gives us the expression for the chemical reaction rate

$$\frac{df_{i,j,k}}{dt} = \begin{cases} \frac{C_g}{\Delta}(1-f_{i,j,k}) & F_{i,j,k} > \left(\frac{1}{2}\right)^2 \\ 0 & F_{i,j,k} < \left(\frac{1}{2}\right)^2 \end{cases}$$

where Δ is cell size. In the original CREBCOM formulation [3] there was no $(1-f)$ dependence in the reaction rate. This change was introduced to provide a softer convergence to the equilibrium composition. The thickness of the flame is approximately of two cells both in original and modified CREBCOM models.

One important feature of the chemical model is the burning velocity C_g can be specified manually by the users. Therefore for some combustion simulation which the burning velocity is known, numerical reproduction of the combustion with the CREBCOM model can be quite convenience.

1.4.2 Simulation approach

Geometry of experiment is quite simple, setting of the computational domain should be focused on saving computational efforts. Firstly, the geometry of the experiment is symmetric to the vertical axis so not the full experiment facility should be simulated. In the Cartesian grid system calculating a quarter of the experiment facility is enough and can save large amount of computational efforts. Figure 3-2 shows the size of the computational domain (marked by yellow border). Since there is one pressure sensor located in 80 meters from the center, the two horizontal directions should be given 100 meters. In the vertical direction, 30 meters is given (in the simulation the X direction and Z direction are in horizontal and Y direction is the vertical direction, so the domain has 100m length in X and Z directions and 30m in Y directions).

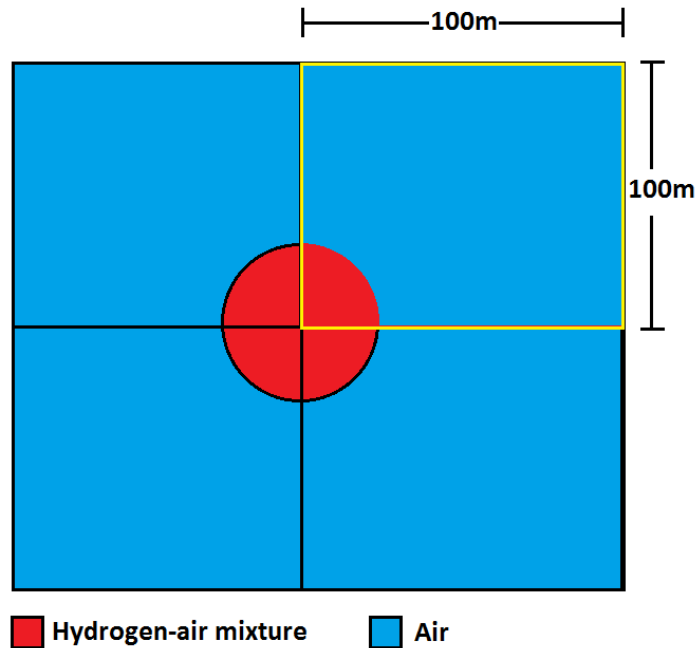


Figure 3-2. Computational domain for 1 quarter experiment

In the setting of computational domain, resolution of the domain is another important issue should be focused on. Under the consideration of saving computational efforts, the 1m resolution is used to construct the computational domain. Therefore the domain has the size of 100X100X30 cells.

In the setting of boundary conditions, three different boundaries should be set at the border of computational domain. Since one quarter of the experiment is simulate, the boundaries at $x=0$ and $z=0$ should be set as mirror style. The boundaries at $x=100$, $y=30$ and $z=100$ should be set as open (non-reflecting) style, because of the experiment is given in open atmosphere. The boundary at $z=0$ corresponds to the ground level in the experiment, such boundary should be set as the non-slipping style.

1.4.3 Numerical details

To reproduce the experiment numerically, CFD combustion code COM3D is used. The spatial discretization for the hydrodynamics is achieved by the second order explicit scheme TVD. This solver is based on article of Ami Harten [4]. TVD here means *Total Variation Diminishing*. Author also uses notion *Total Variation Non-Increasing*.

If takes the 1D problem $\frac{\partial u}{\partial t} + a \frac{\partial u}{\partial x} = 0$ as an example, then *Total Variation* is

$$TV^n = \sum_i |u_{i+1}^n - u_i^n|$$

TVD means that $TV^{n+1} \leq TV^n$. TVD is almost equivalent to *Monotonicity*.

If we return to general hyperbolic problem in which the variable vector is expressed as \bar{Q} , then we generalize definition of total variation,

$$TV = \sum_i \sum_{i+\frac{1}{2}} \left| L_{i+\frac{1}{2}} \cdot (\bar{Q}_{i+1} - \bar{Q}_i) \right|$$

Here $L_{i+\frac{1}{2}}$ is the matrix of left eigenvectors of some approximation of the Jacobian matrix at an intermediate point. Internal sum is the addition of the absolute values of the elements of the vector.

To build a second order TVD solver for hyperbolic equations, we start with some TVD variant of first order solver with upstream differences. This solver, of course, has a numerical diffusion that can be estimated.

Then, we try to remove this diffusion from our method. To do that, we try to modify the set of eigenvalues of our system. The modified system is equivalent to the original with negative numeric diffusion. However, these changes should be limited to ensure that resulting numerical method remains TVD.

Resulting method should be second order everywhere except on points of discontinuity or local extrema. For a linear hyperbolic system, this method is proven to be TVD. For non-linear case, the proof is not known. However this method is considered to be quite reliable. Detailed numerical explanation can be found in reference [4]. In order to get good stability in simulation, the CFL number

$$CFL = \frac{(|u|_{\max} + c)\Delta t}{\Delta x}$$

for the solution of hydrodynamics is set as 0.6 (in COM3D this means the CFL number for a single direction's calculation is 0.3). To keep the same accuracy in time, the alternating direction method is used in the calculation of hydrodynamics part.

Spatial discretization for equation right hand side is achieved by central difference which can provide second order accuracy. In order to keep the second order accuracy in time the second order Runge-Kutta method is used. Therefore the solution of right hand side can also keep both second order accuracy in time and space. Stability of solution is evaluated by the RED number.

$$RED = \max\left(\frac{D_{\max} \Delta t}{\Delta x^2}, \frac{\mu_{\max} \Delta t}{\Delta x^2}, \frac{\lambda_{\max} \Delta t}{\Delta x^2}\right)$$

In the simulation the critical RED number is set as 0.1, under such condition the solution of right hand side can keep quite good stability.

To keep second order accuracy in time the solution of chemical part is also made through second order Runge-Kutta method. However, in the solution of chemical part, most of the attention should be focused on the setting of flame speed in CREBCOM model. In the experiment, propagation of flame is also measured and the flame profiles is shown in Figure 3-3.

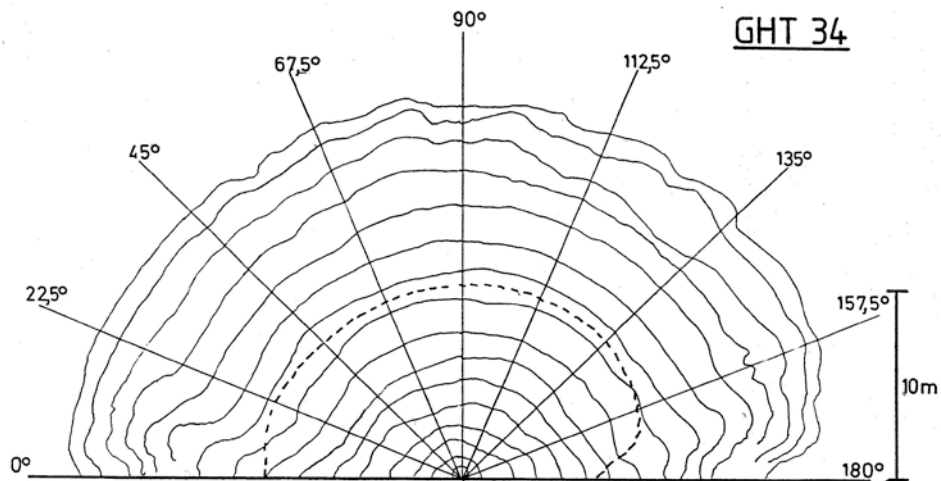


Figure 3-3. Experimentally obtained flame profiles

Figure 3-4 shows the position of the flame front detected by the sensors at different time. Shown as the figure, the speed of the flame is growing, so the flame speed input to the CREBCOM should be different at different process. In the simulation, the whole combustion process is split into 4 stages and different burning velocity is given to each stage to model the combustion in experiment.

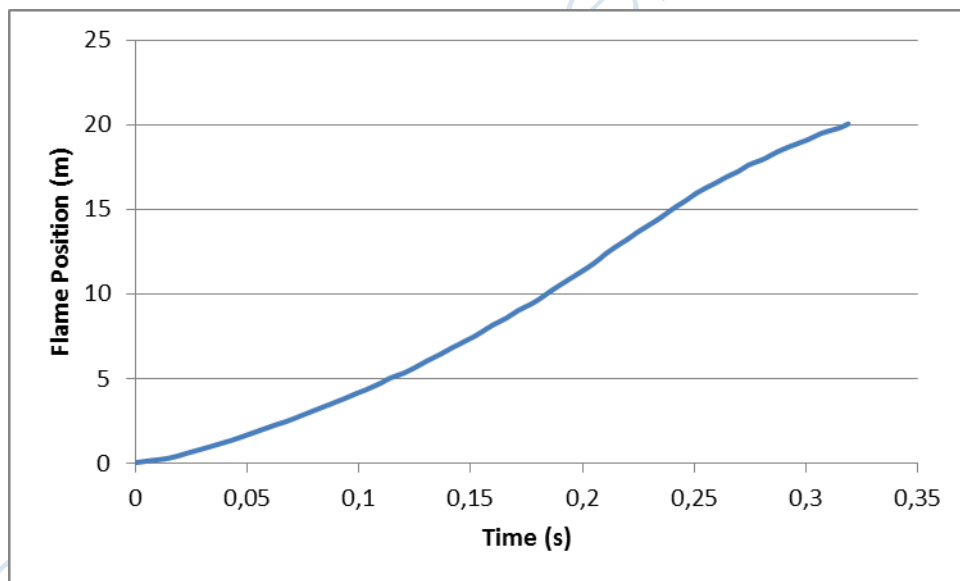


Figure 3-4. Position of the flame front

1.5 Conclusions

Mentioned in the description of the experiment, 10 pressure sensors are installed to get the pressure in experiment. But due to some unknown reason only the experiment results record by sensors at 2m, 5m, 8m, 18m, 35m and 80m are available. The simulation results will be compared with the experimental results at these 6 sensors.

Figure 3-5 is the comparison of the pressure between numerical simulation and experiment at position 2m sensor. The sensor at 2m is quite near to the combustion center, influenced by the strong shock, the pressure records get by the sensor is not complete. However, shown by the Figure 3-5, the tendency of the numerical simulation shows good agreement to the experiment.

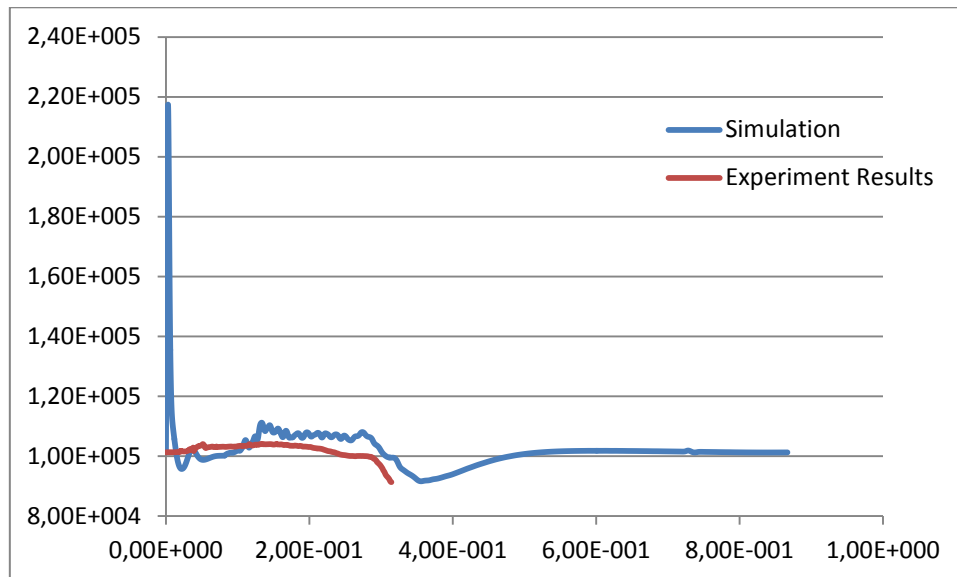


Figure 3-5. Comparison between simulation and experiment at sensor 2m

In the figure a quite high pressure peak appears at the initial stage of the simulation result, such pressure peak is generated by the ignition of hot spot. In numerical simulation the ignition of the fuel is usually accomplished by the force chemical reaction at a region called hot spot, when the fast chemical reaction rate is given in the ignition post quite high pressure wave can be produced. In the numerical simulation of Open Deflagration, in order to ignite the gas mixture fast, big reaction rate is given to the ignition spot, so the high pressure peak is generated. In the comparison, influences of artificial ignition should be ignored.

Since the experimental pressure data at 2m sensor is not complete, comparison between the simulation and experiment should be focused on the other sensors. Figure 3-6 shows the comparison between numerical simulation and experiment at the sensor located at 5m.

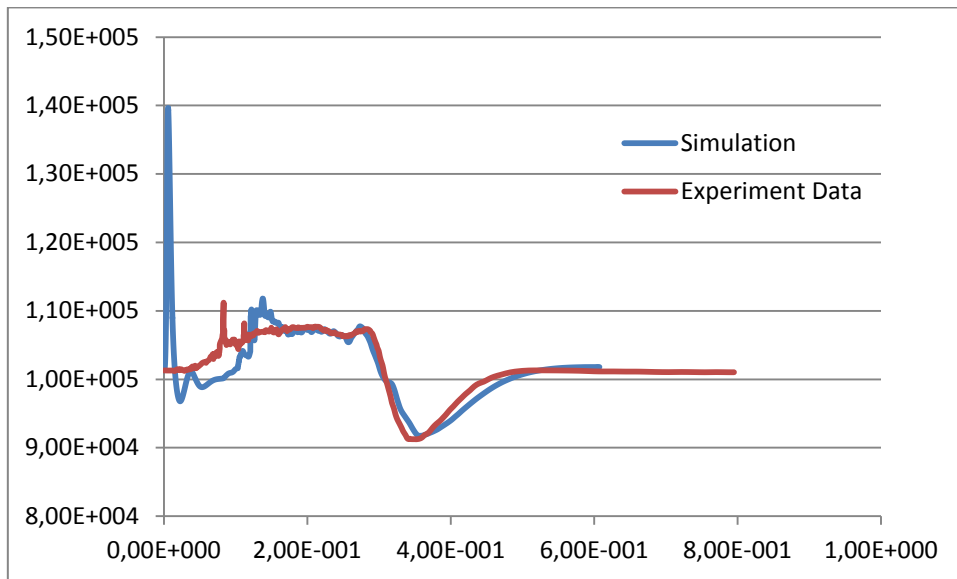


Figure 3-6. Comparison between simulation and experiment at sensor 5m

Firstly, influence of the pressure peak generated by the numerical ignition should be ignored in the comparison. In the comparison of the pressure curves, it is clear that the tendency of the numerical simulation has a quite good agreement with the experiment. In addition, the pressure values of the simulation at both the positive peak and negative peak all fit to the experiment results. So the numerical simulation reproduces the experiment at sensor located at 5m successfully.

Figure 3-7 show the comparison between numerical simulation and experiment at the sensor located at 8m from the ignition center.

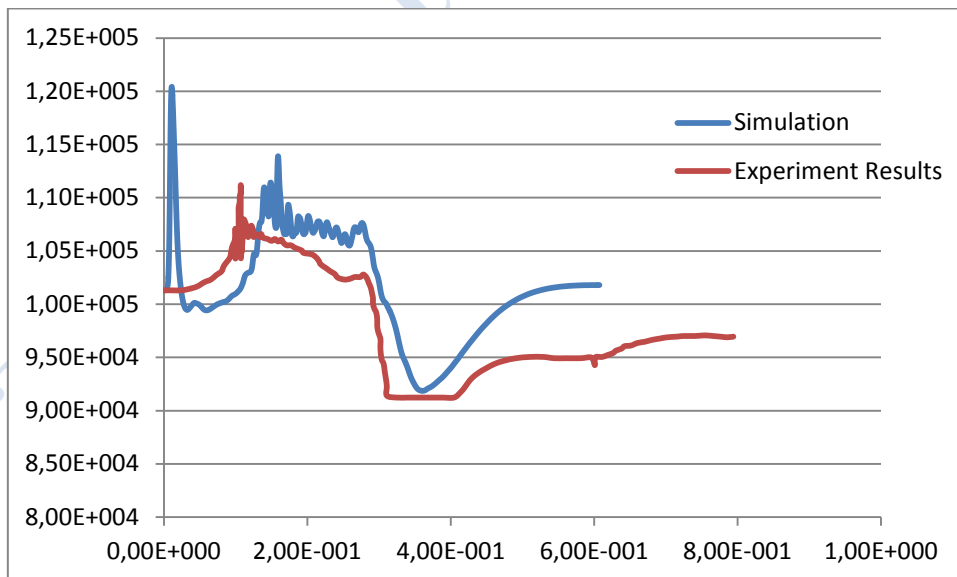


Figure 3-7. Comparison between simulation and experiment at sensor 8m

In the comparison, after the ignoring of the influence of artificial ignition, the simulation pressure values show 2000-1000 pa difference to the experiment in values. However, the tendency of the simulation pressure curve still has a good agreement to

the experiment. In the positive pressure peak part the simulation successfully reproduces the decreasing tendency, and the end of the positive pressure peak both simulation and experiment have a small increasing.

In the analysis of the negative pressure peak part there is several unusual phenomena need to be taken notice on. Firstly, the experiment result shows a flat region at the negative pressure peak but the simulation result shows a full trough shape at the moment. The flat phase in the negative pressure peak can be due to the cutting effect of the pressure sensor (if the over pressure is smaller than the lower limitation the sensor shows the lower limitation value). Then the experiment result does not go back to the standard condition value till the end of the experiment. In common situation the value get from the pressure should go back to around 1bar at the end of the experiment, but the experiment result goes to the value around 97 kpa. It is clear that the pressure sensor located at 8 m is influenced by the heat of the combustion and the pressure values get from the sensor is drag down. So it is quite possible that some pressure data from this sensor has been influenced by the thermos drag and they might be underestimated in value.

As a result, comparison of pressure at the sensor 8m should focus more on if the numerical simulation can have the same tendency as the experiment. In both positive pressure peak and negative pressure peak the simulation successfully reproduce the tendency of the experiment, so numerical simulation is successful at the sensor 8m.

Figure 3-8 is the comparison of the pressure at sensor located at 18m from the ignition center.

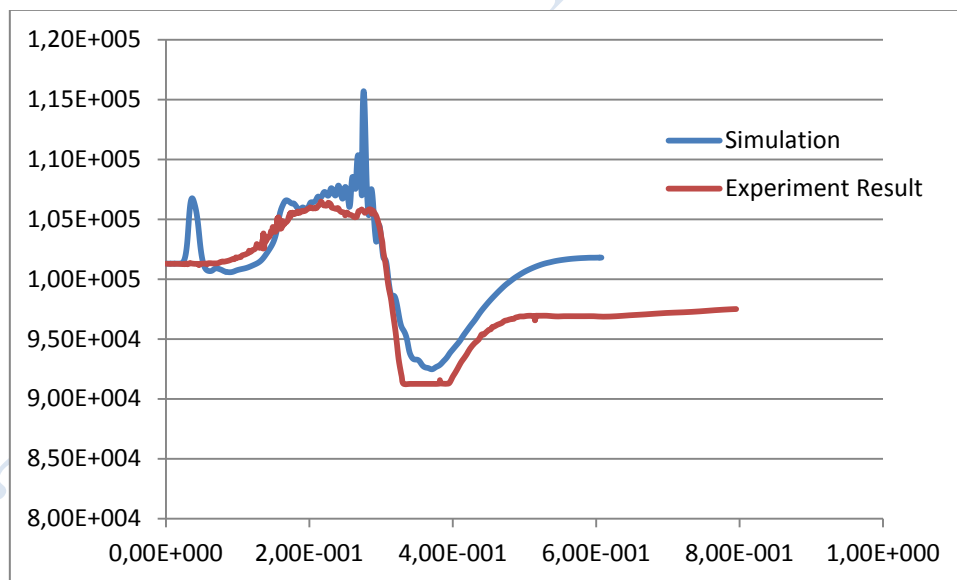


Figure 3-8. Comparison between simulation and experiment at sensor 18m

In the pressure data of simulation it is found that the influence of the artificial ignition becomes very small at this sensor. In the comparison, numerical simulation has a very good agreement with the experiment in the tendency, expect the dramatic pressure growth at the end of the positive pressure peak. The dramatic pressure increasing in numerical simulation should be due to the uncontinuous change of burning velocity in CREBCOM chemical model. In general, the numerical simulation has the same

tendency and value in both the positive and negative pressure peak, the numerical simulation is successful at sensor 18m.

Figure 3-9 is the comparison of pressure at the sensor which is located at the position 35 m from the ignition center.

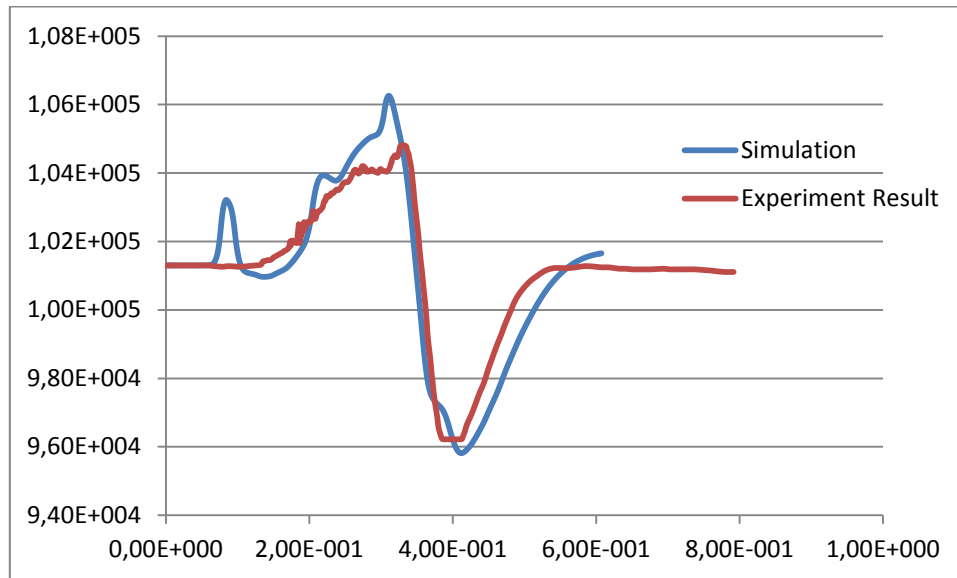


Figure 3-9. Comparison between simulation and experiment at sensor 35m

Shown by the experiment data of flame surface, the flame propagate stopped at the distance 20 m from the ignition centre. Pressure data detected by the sensor at 35m is the sound wave. The first pressure peak in the simulation result is still caused by the artificial ignition, analysis of the pressure data should ignore it. In general, pressure curve of the simulation has the same tendency as the experiment and the pressure value fits with the experiment in most cases. So the pressure comparison in the sensor 35m shows that the numerical simulation is successful.

Figure 3-10 is the comparison of the pressure at the sensor located at 80m from the ignition centre. Similarly to the 35m sensor case, the pressure detected by the sensor is the sound wave.

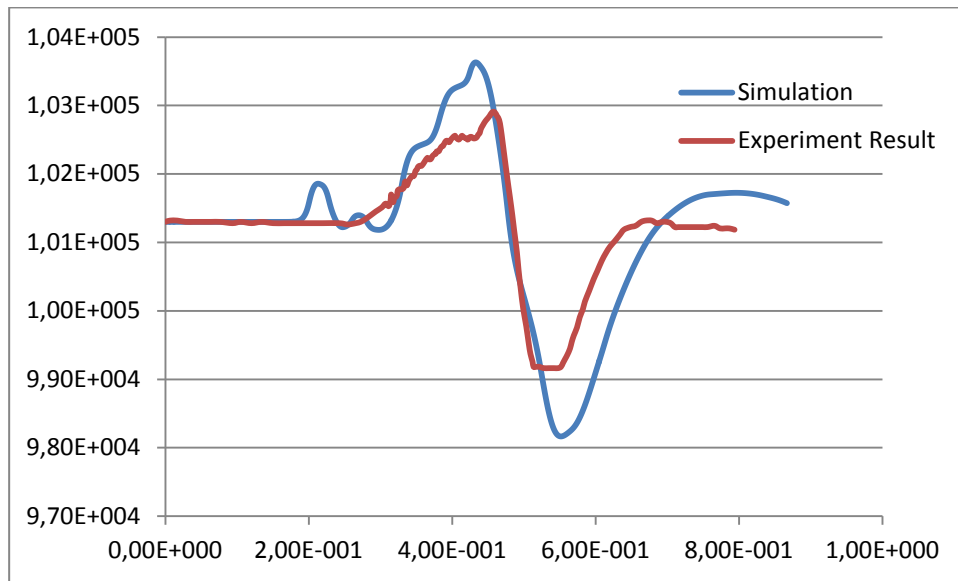


Figure 3-10. Comparison between simulation and experiment at sensor 80m

Shown by the comparison, the pressure curve of numerical simulation has the same tendency as the experiment. The errors between the numerical simulation and experiment are 500-1000 Pa, such errors are acceptable in numerical simulations. So the numerical simulation is successful in comparison of pressure at sensor located 80m from the centre.

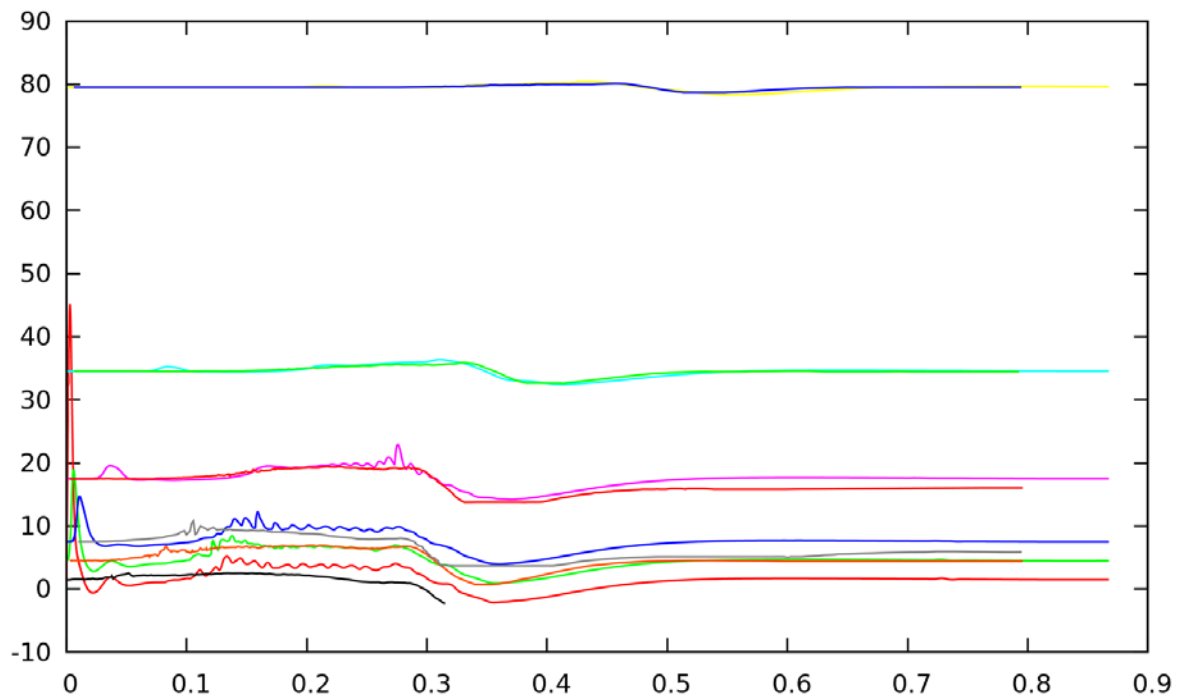


Figure 3-11. R-t diagram of the open deflagration

In total, comparison between numerical simulation and experiment at sensor 5m, 8m, 18m, 35m and 80m all show that the simulation has a good agreement with the experiment. Figure 3-11 shows the R-t diagram of the simulation Open Deflagration.

In the figure, both the numerical result and experiment result are displayed, the shorter time curves belong to the numerical simulation and the longer curves belong to the experiment (the experiment results at sensor 2m is shorter than the others). In general comparison at the R-t diagram, the curves of simulation fit the experiment quite well. So, the numerical simulation reproduces both the chemical reaction and the propagation of sound wave caused by combustion quite successfully.

However, it is still worth to note that using 4 different burning velocities at four different stages to simulate the continuous changing burning velocity in experiment may still not so perfect in reproduce the experiment. The pressure peak at sensor 18m shows the defect of uncontinuous changing burning velocity. If possible, more steps burning velocities or a numerical model which describes the changing of burning velocity should be used in the CREBCOM model to get better result.

1.6 References

- [1] A. Kotchourko, A. Lelyakin, J. Yanez, G. Halmer, A. Svishchev, Z. Xu, K. Re, 2015, COM3D: Turbulent Combustion Code Tutorial Guide Version 4.10, pp. 87-89.
- [2] Bak, P., Chen, K. and Tang, C., 1990, A forest-fire model and some thoughts on turbulence, *Phys. Lett. A* 147, 297-300.
- [3] Efimenko A.A., Dorofeev S.B., 2001, CREBCOM code system for description of gaseous combustion, *Journal of Loss Prevention in the process industries*, pp. 575-581.
- [4] Harten A., 1983, High resolution schemes for hyperbolic conservation-laws, *Journal of Computational Physics*, 49, pp. 357--393.

Deflagration to detonation transition

This experiment was simulated by KIT.

1.7 Experiment overview

Deflagration to detonation transition (DDT) is a quite attractive phenomenon in combustion, and it is very important to hydrogen safety analysis. In this article the numerical reproduction of DDT in H₂-Air mixture is present.

In the article, the experiment reproduced is the DDT in MINI RUT with the experimental ID mr046 (Matsukov et al. 1999). In the experiment, Processes of deflagration to detonation transition was studied in an obstructed channel (cross section 45x50 mm, blockage ratio 0.3 and 50 mm between obstacles), and in a chamber 210x125x50 mm. Stoichiometric H₂-Air mixtures were used in the experiment. The explosion processes and critical conditions for DDT were studied using high speed shadow photography, pressure transducers and photodiodes. The base experimental facility is shown in Figure 4-1.

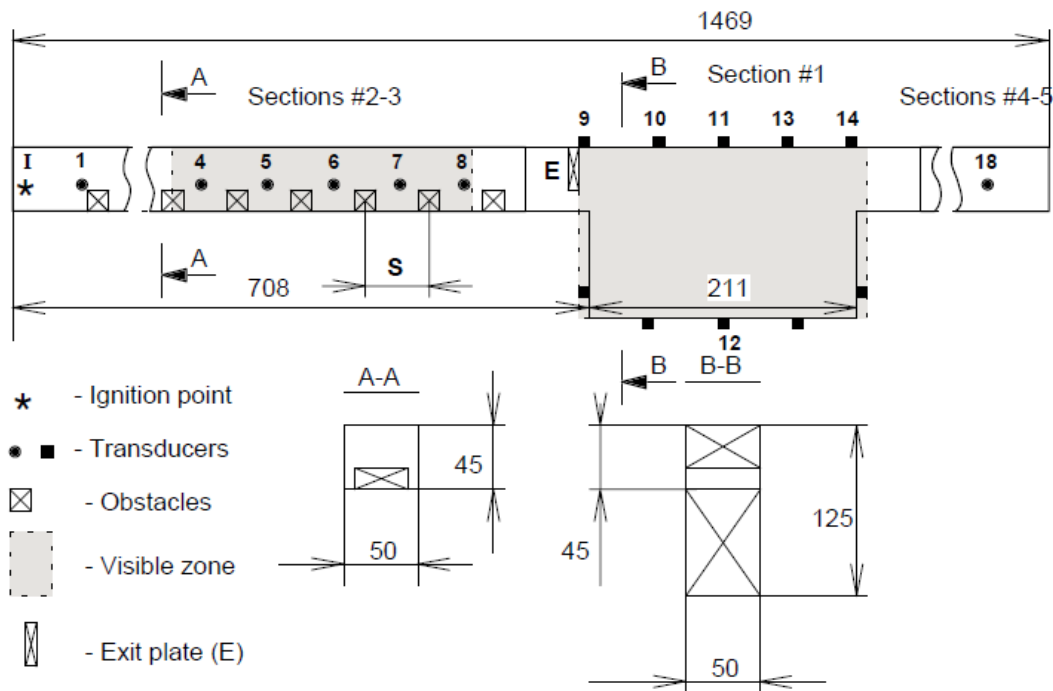


Figure 4-1. MINI RUT facility

Shown as the figure, the experimental facility was composed by three components, the obstructed channel with 12 obstacles, the big volume canyon and the ‘smooth’ square cross section channel. To get details of experiment, several pressure transducers and photodiodes were installed at central line of side wall, ceiling and floor. Shown in the figure 1.1, there are 18 positions are available for the transducers and some of them are used to install the transducers. The detailed locations of these transducers are provided in Table 4-1.

Table 4-1. Transducers

Pressure Transducer	Position mm	Photodiodes	Position mm
P1 (1)	74	L1 (1)	74
P2 (3)	274	L2 (2)	174
P3 (8)	592	L3 (3)	277
P4 (11)	813	L4 (4)	394
P5 (12)	840	L5 (6)	495
P6 (16)	1109	L6 (8)	592
P7 (18)	1377	L7 (9)	701
		L8 (14)	924
		L9 (15)	1058
		L10 (17)	1226

In experiment mr046, in order to achieve DDT in the obstructed channel (indeed in other experiments it has been proved that the basic obstructed channel is not enough for the transition) the obstructed channel was prolonged by a 20cm long channel which still keeps the same cross section and arrangement of obstacles. Therefore the

obstructed channel in experiment mr046 contained 16 obstacles and the positions of all transducers should increase 200mm.

Ignition point in the basic experimental setting was located at the position which is 25mm from the left end of the channel, in the cross section the ignition point located at the center of the rectangle. In the prolonged channel the ignition point was still set at the position located 25mm from the left end. In the experiment, the ignition of gas mixture was accomplished by a quite small sparking. Except the ignition, other information about the ignition condition of the experiment is shown in Table 4-2.

Table 4-2. Initial condition

Temperature K	Pressure bar	Velocity m/s	Gas Species mole ratio
300	1.0	0, 0, 0	H ₂ :O ₂ :N ₂ :H ₂ O=2:1:3.76:0

1.8 Mathematical Methodology

1.8.1 Governing equations

To simulate the complicated flow motion in DDT, large eddy simulation (LES) with the Smagorinsky-Lilly sub-grids model is used. Compared to the RANS model, the LES model is more tolerant to the time step in temporal discretization. In code COM3D, the LES model used contains the conservation of mass, momentum, total energy and gas species. In order to close the whole equations, the perfect gas state equation is used.

For DDT simulation, chemical model plays a quite important role. In the numerical reproduction of experiment mr046, the hybrid DDT chemical reaction model is used.

The DDT model utilized consisted on the comparison of two combustion rates. The combustion rate due to deflagration process is compared with the combustion rate of the detonation for those cases in which the combustible gases has been exposed to detonability conditions a time larger that the corresponding induction time (Sichel, 2002) (Korobeinikov, 1972), (Gaathaug, 2012).

This model can be expressed mathematically with two progress variables. The first one, f , takes the usual definition of progress variable, taking values 0 for fresh mixtures and 1 for products and represents the progress of the reaction. The second variable, c , represents the exposure time to reaction conditions. Under this definitions we have

$$\frac{df}{dt} = \dot{\omega}$$

$$\frac{dc}{dt} = \dot{\theta}$$

where

$$\dot{\omega} = \max(\omega_{detonation}, \omega_{deflagration})$$

and

$$\dot{\theta} = \frac{1}{\tau_{ind}}$$

The reaction rate due to deflagration has been calculated with a modified Gradient mechanism (Lipatnikov, 2002),

$$\omega_{deflagration} = \frac{S_t \rho}{\rho_u} \nabla f$$

where f is the progress variable, and sub-index u stays for unburned.

The turbulent burning velocity S_t , has been calculated utilizing the expression due to (Schmidt, 1998) that is

$$S_t = S_l + \frac{u'}{\sqrt{1 + \frac{1}{Da^2}}}$$

Where S_l is the laminar flame velocity, u' is the turbulent velocity and Da the Damkoeler number.

The consumption rate of the detonation have been estimated in its Arrhenius kinetic form, for the cases in which c is bigger than 1

$$\omega_{detonation} = \begin{cases} 0 & c < 1 \\ k \exp\left(-\frac{E}{RT}\right) & c \geq 1 \end{cases}$$

The values of k and E are import from detonation model in COM3D directly (Kotchourko, 2015). The values obtained for stoichiometric mixtures was $E/R=8736$ K and $k=1.5e7$ s⁻¹. Shown by the detonation reaction rate, the switch of reaction rates in DDT simulation depends on the c which is determined by induction time.

Following the described methodology it is necessary the knowledge of the induction time in each control volume and time step during the calculation. This can be achieved only without a significant overhead and consequent delay of the calculation through the creation of a correlation for the induction time. The consulted sources in the literature has not delivered a ready correlation valid for stoichiometric H₂-air mixtures in a range of temperatures between 1200K and 3000K and a range of pressures between 0.1 and 10 MPa. Therefore, we have built our own correlation. This has been done as follows. The induction time has been calculated utilizing the program Cantera (Goodwin, 2009). Afterwards an expression of the type

$$\tau_{ind} = K \frac{T}{P} \exp\left(-A + \frac{B}{T} + C \left(\frac{P}{1e5}\right)^D \exp\left(\frac{E}{T}\right)\right)$$

where, A, B, C, D, E are parameters has been fitted to adjust the 178200 points in which the values of the induction time are available. By analogy with the form available in (Sichel, 2002) K is considered to be

$$K = \frac{(\phi + 1) \left(\phi + \frac{1}{2}\right)}{\phi} R$$

where ϕ is the equivalence ratio (equal to one in an stoichiometric mixture) and R is the constant of the gases.

The results of the fitting, performed with the module “curve_fit” of sciplot (python) provides a linear determination coefficient of 0.84 and the values A=20.7, B=7978, C=0.0128, D=0.72, E=2407 for the parameter of the model. The quality of the adjustment of the models can be judged by observing the points obtained with Cantera in blue (one each 50 represented) and the grey surface (model)

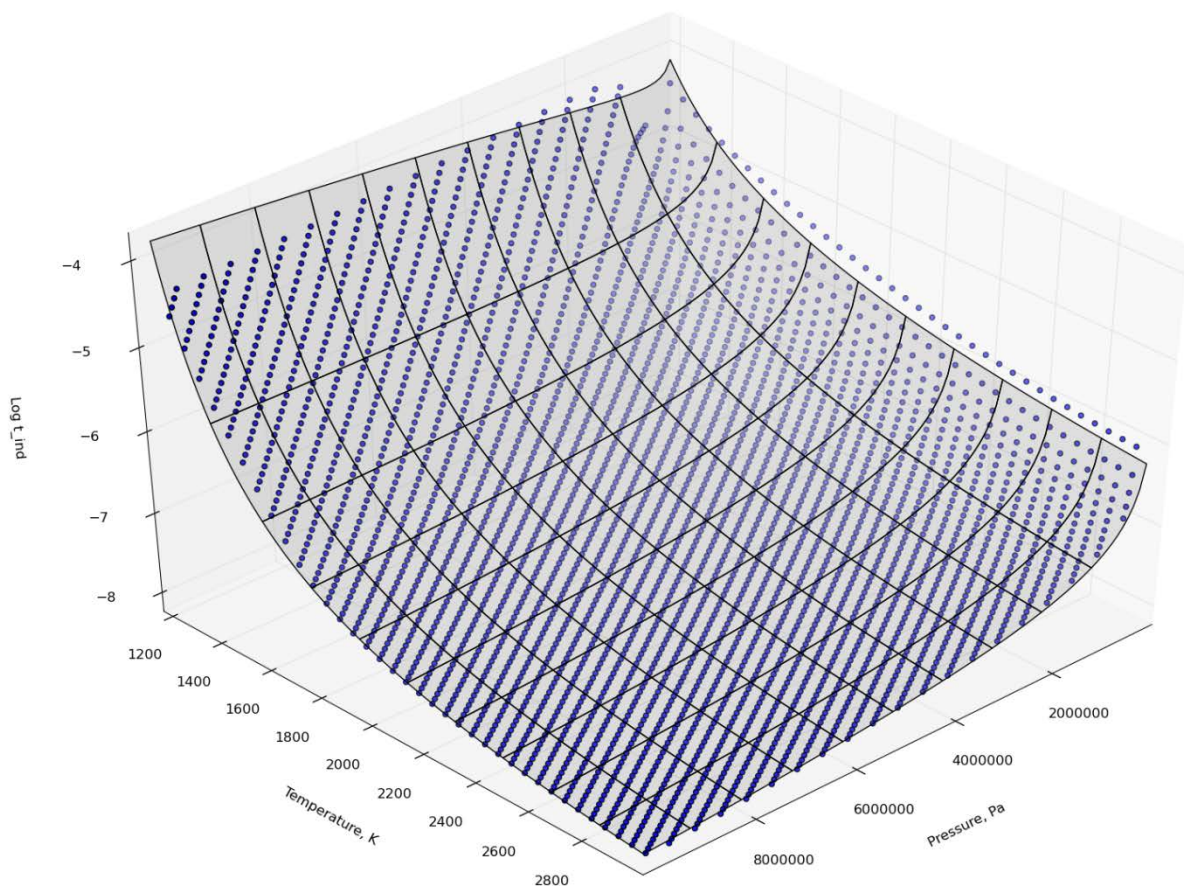


Figure 4-2. Induction times

The model developed has fundament in the literature and its form should be accepted without major concerns.

The approximation of the induction time, even if for lower temperatures is less accurate (see Figure 4-2), would have not major impact in the result. For the short timescales in which the DDT will take place for low temperatures the induction time could be considered as infinity without major regard to its real value.

1.8.2 Simulation approach

Similar to the RUT facility, the geometry of MINI RUT is also quite complicated. However, the numerical reproduction of DDT phenomena indeed does not require reconstructing the whole facility.

In experiment mr046, deflagration transitioned to detonation at the end of the obstructed channel. Therefore, in the simulation of DDT only the obstructed channel is necessary. In this situation all the computational resources can be focused on the channel and much higher resolution can be used in the computational domain.

In the construction of computational domain, it is necessary to notice that the obstacles in the channel do not fully block the lower part of the channel, there still exist small gaps between the obstacles and side walls. The gap has the width of 2.5mm, so the maximum resolution allowed in the code COM3D in this simulation is 1.25mm (in code COM3D there should be at least 2 gas cells between two solid obstacles). However, 2 cells between the solid surfaces is not sufficient for resolving the turbulent motion of the flow in the gap, under the consideration of total computational cost the resolution is fixed to 0.5mm. To construct the obstructed channel $2000 \times 90 \times 100 = 18$ million structured uniform cells are used in the computational domain. Since the resolution 0.5mm is used in the domain, the geometry of experimental channel can be reproduced quite accurately in the computational domain. Figure 4-3 shows the 3D overview of the numerical computational domain and Figure 4-4 shows that the details of the geometry are present accurately in the computational domain.

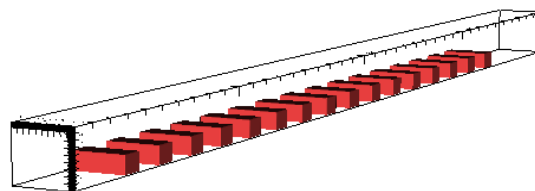


Figure 4-3. 3D overview of the computational domain

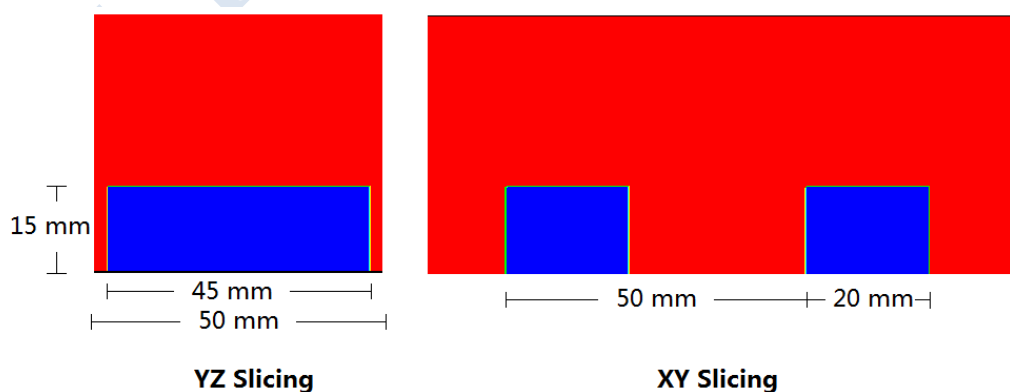


Figure 4-4. Details of geometry in computational domain

In setting of boundary conditions, since partial experimental facility is present in the computational domain the end of obstructed channel should be set as no-reflecting boundary (also called open boundary).

1.8.3 Numerical details

To reproduce the experiment numerically, CFD combustion code COM3D is used. The spatial discretization for the hydrodynamics is achieved by the second order explicit scheme TVD. This solver is based on article of Ami Harten (Harten, 1983). TVD here means *Total Variation Diminishing*. Author also uses notion *Total Variation Non-Increasing*.

If takes the 1D problem $\frac{\partial u}{\partial t} + a \frac{\partial u}{\partial x} = 0$ as an example, then *Total Variation* is

$$TV^n = \sum_i |u_{i+1}^n - u_i^n|$$

TVD means that $TV^{n+1} \leq TV^n$. TVD is almost equivalent to *Monotonicity*.

If we return to general hyperbolic problem in which the variable vector is expressed as \bar{Q} , then we generalize definition of total variation,

$$TV = \sum_i \sum \left| L_{i+\frac{1}{2}} \cdot (\bar{Q}_{i+1} - \bar{Q}_i) \right|$$

Here $L_{i+\frac{1}{2}}$ is the matrix of left eigenvectors of some approximation of the Jacobian matrix at an intermediate point. Internal sum is the addition of the absolute values of the elements of the vector.

To build a second order TVD solver for hyperbolic equations, we start with some TVD variant of first order solver with upstream differences. This solver, of course, has a numerical diffusion that can be estimated.

Then, we try to remove this diffusion from our method. To do that, we try to modify the set of eigenvalues of our system. The modified system is equivalent to the original with negative numeric diffusion. However, these changes should be limited to ensure that resulting numerical method remains TVD.

Resulting method should be second order everywhere except on points of discontinuity or local extrema. For a linear hyperbolic system, this method is proven to be TVD. For non-linear case, the proof is not known. However this method is considered to be quite reliable. Detailed numerical explanation can be found in reference [4]. In order to get good stability in simulation, the CFL number

$$CFL = \frac{(|u|_{\max} + c)\Delta t}{\Delta x}$$

for the solution of hydrodynamics is set as 0.9 (in COM3D this means the CFL number for a single direction's calculation is 0.45). To keep the same accuracy in

time, the alternating direction method is used in the calculation of hydrodynamics part.

Spatial discretization for equation right hand side is achieved by central difference which can provide second order accuracy. In order to keep the second order accuracy in time the second order Runge-Kutta method is used. Therefore the solution of right hand side can also keep both second order accuracy in time and space. Stability of solution is evaluated by the RED number.

$$RED = \max\left(\frac{D_{\max} \Delta t}{\Delta x^2}, \frac{\mu_{\max} \Delta t}{\Delta x^2}, \frac{\lambda_{\max} \Delta t}{\Delta x^2}\right)$$

In the simulation the critical RED number is set as 0.4, under such condition the solution of right hand side can keep quite good stability.

To keep second order accuracy in time the solution of chemical part is also made through second order Runge-Kutta method.

In addition, consuming of fuel in each gas control volume should also be considered in the stability criteria. In one step calculation the fuel spent in the chemical reaction should not exceed the amount of fuel remained in the control volume.

In total, time step used in the calculation should be decided by CFL number, RED number and the local fuel consuming.

1.9 Results and discussion

To get the experiment result, 7 pressure transducers and 10 light transducers are installed in the experimental facility. However, since partial facility (the obstructed channel) is present in the computational domain, only the pressure data from 3 pressure transducers and lighting signal from 5 photodiodes can be compared with numerical simulation.

In numerical simulation the deflagration transits to detonation around the last obstacle of the obstructed channel. In the following part, comparison will be focused on the comparison of pressure result, R-t diagram of pressure result and the R-v diagram to show that the numerical simulation reproduce the experiment successfully.

In the obstructed channel, pressure transducers are located at 0.27m, 0.47m and 0.79m. Comparison of pressure at the transducer P1 located at 0.27m is shown in Figure 4-5.

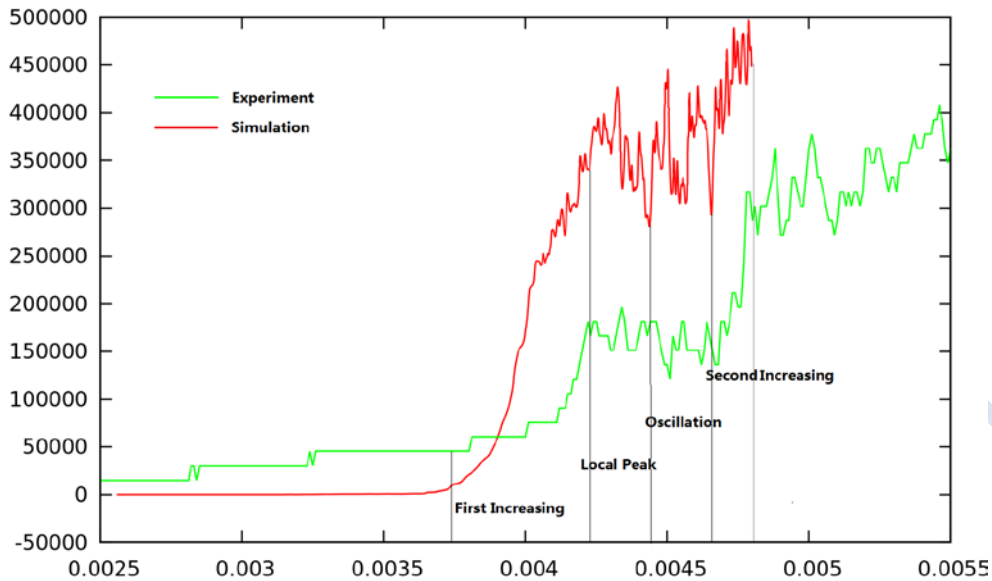


Figure 4-5. Comparison of pressure records at sensor P1

In the figure, numerical result shows higher pressure value when compared with the experiment result. However, as shown in the figure, the pressure curve of numerical simulation has the same trend as the experiment: in the stage of first increasing, both experiment and numerical simulation increase monotonically and last almost the same period of time; in the stage of local peak, there exists valley structure before the peak and after the peak, and in the numerical simulation the valleys are reproduced successfully; in the stage of oscillation, both the experiment curve and simulation curve have two big valleys and two big peaks in the main trend, especially in the first big the numerical simulation reproduces the small oscillation as well; finally, in the stage of second increasing, both the two curves increase oscillatory. Although numerical simulation shows much bigger pressure values at transducer P1, the numerical simulation can still be accepted for it can reproduce the motion of pressure.

Figure 4-6 shows the comparison of pressure at the pressure transducer P2 located at 0.47m. Shown in the figure, pressure values of numerical simulation are much bigger than the pressure records from experiment. However, in the analysis of curve trend, it is clear that the numerical simulation reproduces the pressure trend in experiment successfully: in the stage of increasing, both simulation and experiment have monotonic increasing phase and sharp decreasing phase; in the stage of peak, both numerical simulation and experiment have 4 peaks and 4 valleys, and the timing of those peaks and valleys are almost the same; in the stage of oscillation, the two curves have the same oscillation trend and the timing of those oscillations are the same. So, similar to the result of comparison at P1, although there exist big differences in pressure values, we still thought that the numerical simulation reproduces the physics in the experiment successfully.

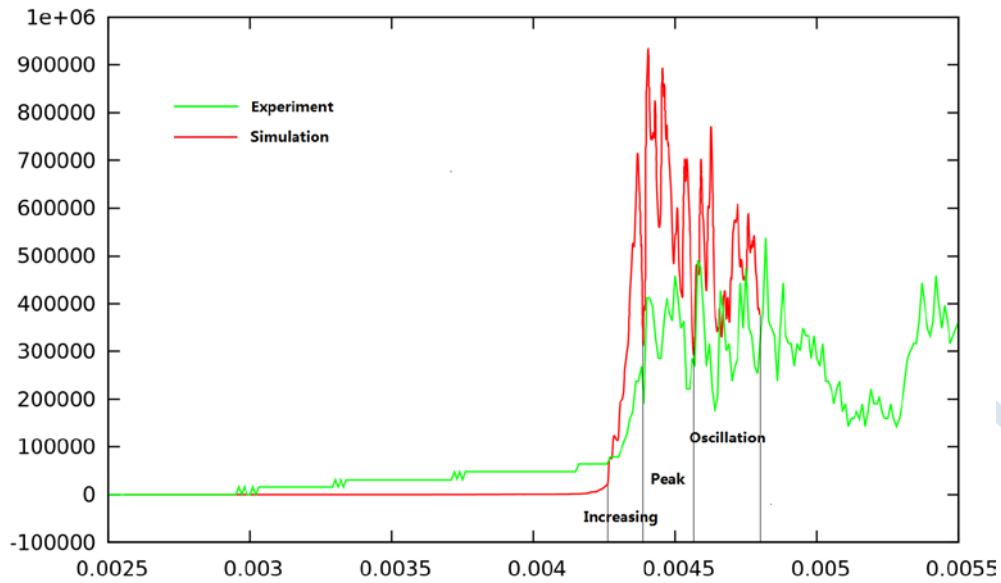


Figure 4-6. Comparison of pressure records at sensor P2

Figure 4-7 shows the comparison of pressure at the transducer P3 located at 0.79m which is quite near to the transition point.

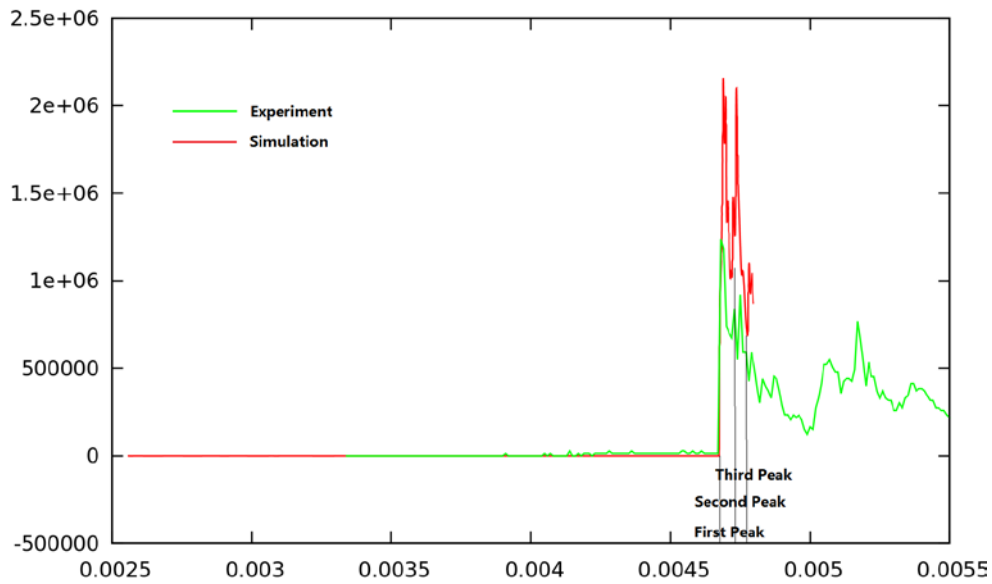


Figure 4-7. Comparison of pressure records at sensor P3

Shown as the Figure 4-7, the numerical simulation reproduces the trend of experiment, especially in the stages of the second and the third peak the oscillations are reproduced. In total, the numerical simulation reproduces the pressure motion at this sensor successfully.

Figure 4-8 shows the R-t diagram of the pressures, in the figure comparison of pressure between numerical simulation and experiment is made in general,

propagation of pressure wave and the propagation of reflecting waves can be expressed clearly in the diagram.

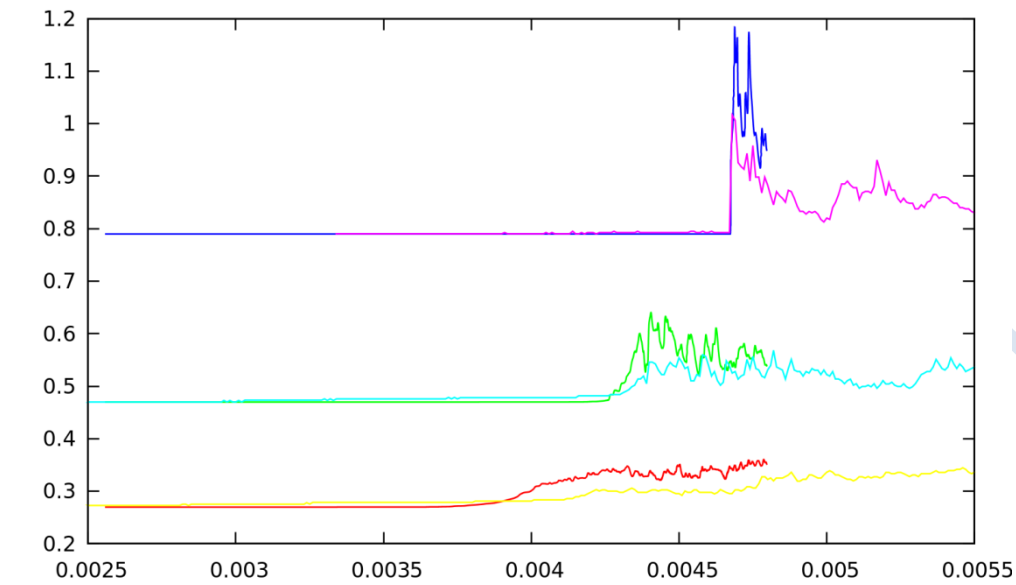


Figure 4-8. R-t diagram of pressure

In the comparison of pressure values between numerical simulation and experiment in R-t diagram, it is not difficult to find that the propagation speed of the pressure wave in numerical simulation is almost the same as the experiment. In code validation, comparison propagation speed of the pressure wave is very direct and accurate, good agreement of numerical simulation and experiment in propagation speed usually means the numerical simulation reproduce the real motion of pressure wave.

However, in the comparison of pressure records it is still necessary to clarify why the big differences in pressure values between numerical one and experiment are acceptable. Normally, propagation speed of pressure wave depends on the strength of pressure wave, so good agreement in propagation speed usually means the comparison of pressure values at each pressure transducers should have good agreement as well. In above, comparison of pressure in R-t diagram shows that the general propagation speed in numerical simulation fits the experiment well and the comparisons of pressure at each transducer show the numerical simulation can reproduce the propagation of pressure and its reflecting quite good, the only problem is the numerical pressure value is bigger than the experiment. In the setting of computational domain it has been mentioned that resolution used is 0.5mm which is much smaller than the size of pressure sensor, so the pressure data detected by the sensors should not be as resolved as numerical ones and could be much smaller than the high resolution simulation. In addition, in the code validation the uncertainty of experiment should also be considered in the analysis, in the analysis of the other pressure sensor data it has been found that the pressure value of the detonation wave has also been underestimated in the experiment and it is clear that the pressure value has been underestimated uniformly. In general, the big differences in pressure values should not be focused too much, the good agreement in propagation speed and curve

trend can already show that the numerical simulation can reproduce the motion of pressure wave in the experiment successfully.

Besides the comparison of pressure data, repeating the similar flame acceleration process of DDT is also a quite important aspect for evaluating the numerical simulation (DDT is a statistic phenomenon and can hardly be repeated in experiment, so we do not need to reproduce the same flame acceleration process).

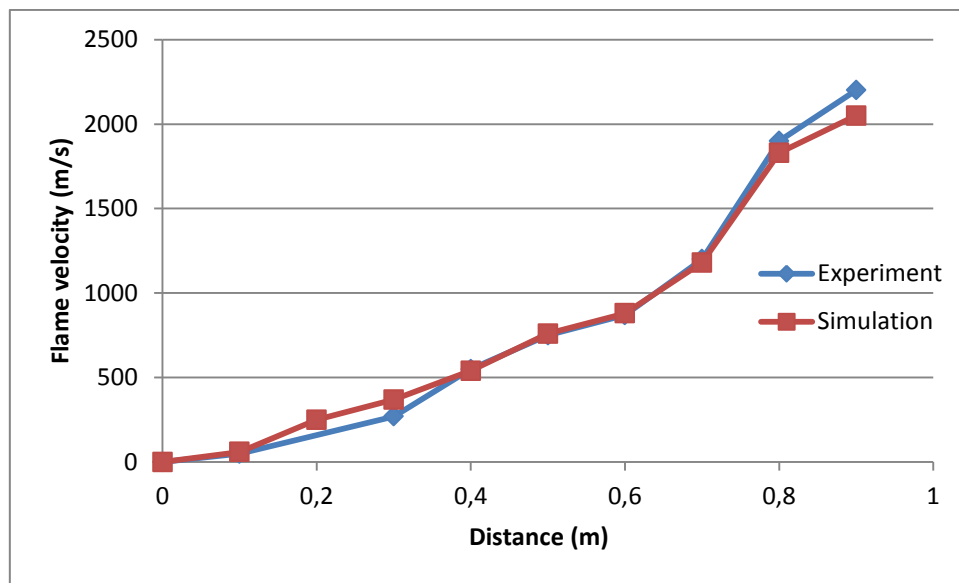


Figure 4-9. R-v diagram of experiment and simulation

Figure 4-9 shows the R-v diagram of numerical simulation and experiment. In the diagram the horizontal axis is the distance to the wall and the vertical axis is the velocity of the flame. The R-v diagram shows the whole flame acceleration process, comparison between the flame acceleration process of numerical simulation and the flame acceleration process of experiment can show clearly if the numerical simulation can reproduce the experiment. Shown by the figure, numerical simulation generally reproduces the flame acceleration in the real experiment. Therefore, numerical simulation managed to reproduce the main trend of flame propagation.

General speaking, numerical simulation can reproduce the motion of pressure wave and flame propagation in the experiment, so the numerical simulation can be regarded as a successful reproduction of the DDT in MINI RUT facility.

1.10 References

I.D. Matsukov, M.S. Kuznetsov, V.I. Alekseev and S.B. Dorofeev, Photographic study of transition from fast deflagration to detonations, 22nd International Symposium on Shock Wave, 1999, 195-200.

Efimenko, A. D. (2001). CREBCOM code system for description. *J. Loss Prev. Process Ind.*, 14, 575–581.

Gaathaug, A. V. (2012). Experimental and Numerical Investigation of DDT in Hydrogen-air behind a single obstacle. *37*, 17606-17615.

Goodwin, D. (2009). *Cantera: An object-oriented software toolkit for chemical kinetics, thermodynamics, and transport processes*. Pasadena, Ca, USA: Caltech.

Korobeinikov, V. L. (1972). Propagation of Blast Waves in a Combustible Gas. *Astronautica Acta*, *17*, 529-536.

Lipatnikov, A. N. (2002). Turbulent flame speed and thickness. *Progress in energy and combustion science*, *S*, 1-74.

Schmidt, H. H. (1998). *Combustion and flame*, *79*, 113.

Sichel, M. T. (2002). A two step kinetics model for numerical simulations of explosions and detonations in H₂-O₂ mixtures. *Proceeding of the Royal Society of London*, *458*, 49-82.

A. Kotchourko, A. Lelyakin, J. Yanez, G. Halmer, A. Svishchev, Z. Xu, K. Re, 2015, COM3D: Turbulent Combustion Code Tutorial Guide Version 4.10, 87-89.

Harten A., 1983, High resolution schemes for hyperbolic conservation-laws, *Journal of Computational Physics*, *49*, 357--393.